THE EFFECT OF HEAT TREATMENT ON MICROSTRUCTURAL EVOLUTION AND MECHANICAL PROPERTIES OF 3D PRINTED MEDICAL GRADE TI6AL4V

NIYOUSHA AZGOMI

A THESIS SUBMITTED TO
THE FACULTY OF GRADUATE STUDIES
IN PARTIAL FULFILLMENT OF THE REQUIREMENTS
FOR THE DEGREE OF
MASTER OF APPLIED SCIENCE

GRADUATE PROGRAMME IN MECHANICAL ENGINEERING
YORK UNIVERSITY
TORONTO, ONTARIO

DEC 2019

ABSTRACT

The merger of metal 3D printing with a simple post-processing treatment to fabricate parts using Ti6Al4V medical-grade titanium alloy would prove very desirable for most biomedical applications. In this study, the effect of post-processing heat treatment on the microstructure and properties of 3D printed and conventionally manufactured Ti6Al4V medical-grade titanium alloy was investigated to determine the performance of the as printed and heat-treated parts. In general, heat treatment led to the growth of distinct continuous and discontinuous α lath structures along prior β grain boundaries as well as basketweave lath and V-shaped structures within the prior-β grains. V-shaped and spherical structures were specific to 3D printed and conventional samples, respectively. Also, regarding the mechanical properties, 3D printed samples had better wear resistance as well as higher hardness compared to the conventional samples due to the presence of V-shaped structures.

Acknowledgments

I would like to thank my supervisor, Professor Solomon Boakye-Yiadom, for allowing me to work on this different and interesting project. I am grateful for his advice and encouragement at every stage of my work.

A big thank you to my committee members, Alex Czekanski and Matthew Perras, for taking time out of their busy schedules to review my thesis and giving efficient feedback.

I am also thankful for the mechanical engineering faculty and technician group especially, David Marcinkiewicz who shared their knowledge and support with no hesitation.

I would like to acknowledge my supportive husband, Paul, for his absolute honest support and patience during these two years.

I would also like to thank my parents and my sister, Naghmeh for encouraging me every day to follow my true dreams and reminding me of all the amazing things I am capable of.

Table of Contents

List of Table

List of Figures

COPYWRITE PERMISION

Figure 2.1 – J. Donachie and J. M, "Titanium – A Technical Guide," *ASM Int. 2nd Ed.*, 2000- Reprinted with permission from Pergamon, December 12,2019.

Figure 2.2 − J. Sedlak, D. Rican, M. Piska, and L. Rozkosny, Procedia Engineering- Reprinted with permission from Elsevier Ltd, December 12,2019.

Figure 2.3 – J. D. Avila, S. Bose, and A. Bandyopadhyay, Titanium in Medical and Dental Applications- Reprinted with permission from Elsevier December 12,2019.

Figure 2.4 – H. Galarraga, D. A. Lados, R. R. Dehoff, M. M. Kirka, and P. Nandwana, Additive Manufacturing-Reprinted with permission from Elsevier December 12,2019.

Fig 2.6 − L. Parry, I. A. Ashcroft, and R. D. Wildman, Additive. Manufacturing- Reprinted with permission from SPRINGER-VERLAG LONDON, December 12,2019.

Figure 2.7 – J. A. Cherry, H. M. Davies, S. Mehmood, N. P. Lavery, S. G. R. Brown, and J. Sienz, Int. J. Adv. Manuf. Technol. -Reprinted with permission from Elsevier December 12,2019.

Figure 2.8 − A. Ducato, L. Fratini, M. La Cascia, and G. Mazzola, Computer Analysis of Images and Patterns: 15th International Conference, CAIP 2013- Reprinted with permission from Springer December 12,2019.

List of Abbreviations and Symbols

Abbreviations	**Description**
3D	3 Dimensional
AC	Air Cooled
AM	Additive Manufacturing
BCC	Body Center Cubic
CV	Conventional
DMLS	Direct Metal Laser Sintering
EBM	Electron Beam Melting
ELI	Extra Low Interstitial
HCP	Hexagonal Closed Packed
LMD	Laser Metal Deposition
OM	Optical Microscope
SEM	Scanning Electron Microscope
SLM	Selective Laser Melting

SLS	Selective Laser Sintering
STL	File Format
TEM	Transmission Electron Microscopy
Ti6Al4V	Titanium, 6% Aluminum, 4% Vanadium
WQ	Water Quenched
XRD	X-ray Diffraction
α	Alpha Crystal
α’	Alpha Prime Crystal
β	Beta Crystal

Chapter 1 Introduction

1.1 Background and Motivation

Recently, advances in Metal 3D Printing have led to revolutionary manufacturing techniques for fabricating parts with complex geometry from 3D CAD drawing of the part. They offer design flexibility to produce intricate shapes for customized medical parts by simply making computer-aided drawings of the parts. DMLS (is an example of a powder bed fusion metal) 3D printing process. This manufacturing process is a technology to manufacture complex geometries. Also, the final products are stronger and denser than conventionally manufactured parts. DMLS[1]. process starts with heating the desired metal powder in the powder bed, near to alloy's sintering temperature. Next, a thin layer of powder is dispensed on the build platform and based on the CAD drawing, a high energy laser selectively sinters the powder into a solid shape. In the end, after the part is cooled down, the remaining metal powder is removed. This additive manufacturing process is recently becoming more attractive for medical-grade Ti6Al4V manufacturing [1].

The Ti6Al4V (ELI Extra Low Interstitial) is a two-phase (α & β) alloy at room temperature. The α phase (hcp crystal structure) is contributing most to the mechanical strength of the structure while the β phase (bcc crystal structure) is imparting some ductility to this alloy. In Ti6Al4V, aluminum is the α stabilizer and vanadium is the β stabilizer elements and the lowest equilibrium temperature at which this alloy's structure is all β is called β transus (975℃).The alloy's structure changes to all beta (BCC crystal)structure at or above beta transus. In heat treatment, three specific parameters including temperature, time and rate of cooling may result in different microstructure and mechanical properties. Choosing optimized heat treatment conditions including the temperature and cooling rate will result in better mechanical properties [2].

Titanium alloys have a wide application in the biomedical industry, because of their attractive properties such as high strength to weight ratio, good corrosion resistance, and biocompatibility. All these great features make this alloy's usage increase daily [3], [4]. With these large amounts of alloy's usage, it is desirable to have manufacturing processes that minimize the production time. Conventional manufacturing techniques such as casting result in a large material waste as well as high manufacturing cost. However, Additive Manufacturing (AM) using powder bed fusion techniques for metallic products offsets the disadvantages of the conventional manufacturing

techniques and also it is providing customization to biomedical products [5], [6]. Residual stresses, surface roughness, and porosity are some of the disadvantages of additive manufacturing which can be improved by post-processing like heat treatment which can as well improve the mechanical properties of titanium alloys. For biocompatibility, stability, and cost, heat treatment is the most conducive method which can be used to reduce residual stresses, to bring proper ductility and stability to the structure, to increase strength and optimize special properties [2].

Besides heat treatment's effects on mechanical properties (wear rate) of Ti6Al4V, velocities, loads, and the oxide layer are other elements affecting wear and friction in materials [7]. Recent studies have proven that the improvement of the wear properties of titanium alloys is related to the reinforcement content which means the higher consolidation lead to a lower wear loss rate [8]. In addition, some studies illustrated that the higher hardness results in lower friction coefficient which are both dependent on the alloy's microstructure[9]. On the other hand, materials with high hardness properties may not always lead to the lowest wear rate. For example, the primary martensite phase has been reported to have the worst wear resistance, even though it has the highest hardness properties [10].

1.2 Problem Statement and Research Objectives

Although there have been several studies on Ti6Al4V ELI, the mechanical properties data presented from these studies are not very consistent. In addition, since the DMLS printing method is a new-developed manufacturing technique, there are not many studies clarifying the microstructure and mechanical properties of the medical grade Ti6Al4V alloys and possible techniques to improve these properties. The aim of this work is to study the possibility of using a heat treatment technique to improve the microstructure and mechanical properties of medical-grade Ti6Al4V. A comparison will be made using an alloy processed by conventional techniques against a 3D printed one. This is critical in tailoring and improving the structure and properties of these materials for medical applications. For this purpose, all specimens were heat treated and their hardness and wear resistance were investigated by microhardness and wear test equipment. Microscopy analysis was done by using an optical microscope and Scanning Electron Microscope (SEM).

1.3 Research Methodology

There were three major processes to achieve the objectives of this study. Firstly, one sample from each group (conventional and 3D printed) was chosen as the controlled samples. Then, to find the optimized properties, all other samples (16 samples) were solutionized at 1080℃ to achieve a complete beta phase structure. The purpose of choosing this temperature was to heat all the samples to the above beta transus temperature (975℃) in order to make the specimens comparable to each other. The solutionizing was followed by air-cooling half of the samples and fast cooling(water-quenching) the rest of the specimens. One sample from each group was chosen to be aged at 200, 500, and 800The heat treatment process was followed by a comprehensive microstructural characterization to determine the morphology of the heat-treated specimens and the as-received ones. Moreover, a comparison between the baseline samples' morphology and the heat-treated ones was also done to investigate the microstructural evolution of Ti6Al4V ELI at different heat treatment conditions. This study used different microstructural characterizing techniques including, optical microscope, Scanning Electron Microscope (SEM), X-ray Diffraction analysis (XRD), and Electron Probe Microanalysis to reveal the microstructure of medical-grade Ti6Al4V at different heat treatment conditions. Finally, the effect of heat treatment on the mechanical properties of medical-grade Ti6Al4V was studied by Micro Vickers Hardness test as well as rotary wear test equipment with lubricant. These mechanical tests were done to measure and compare the hardness and wear rate of each condition, respectively. In general, the careful study of the microstructures and results from the mechanical tests would increase our understanding of the effect of manufacturing techniques and post-processing on the microstructure and properties of medical-grade Ti6Al4V.

1.4 Summary of Finding

In general, distinct α lath and basket weave lath structures with high degree of orientation were observed within the as-printed samples. As the alloys were heat treated, different microstructures were observed in different conditions. V-shaped structures were mostly noticed in 3D printed samples, which started appearing in solutioned samples. The volume fraction of the V-shaped structures was rising by increasing the aging temperature. The maximum V-shaped structures were found at aged 500℃ and as the sample was aged at 800℃, the volume fraction of this microstructure was reduced. Lath structure was the second structure noticed in Ti6Al4V alloys.

Heat treatment led to the growth of distinct continuous and discontinuous α lath structures along prior β grain boundaries. As the aging temperature was rising, the thickness of lath structures appeared at grain boundaries was enlarging. About the same result was noticed in basket weave structures, which were mostly formed in the middle of grain. The formation and thickness of the basket weave structures were improved by increasing the aging temperature which at 800℃ some basket weave structures were formed close to the grain boundaries. Different microstructures appeared on the alloy's surface had a significant impact on the hardness of both 3D printed and conventional samples. The presence of V-shaped structure regardless to the aging temperature or manufacturing techniques resulted in the highest hardness, while basket weave structures led to the lowest hardness among all the other observed microstructures. Also, density and thickness of the lath structures resulted in a different hardness value. Therefore, in both water-quenched/aged and air-cooled/aged samples, the 3D printed samples at 500℃ had the highest hardness as a result of the presence of coarse V-shaped structures. Moreover, the 3D printed samples generally had higher wear resistance than the conventional samples regardless of the heat treatment condition.

1.5 **Thesis Organization**

This thesis is structured into six chapters. The following includes a summary of each chapter:

- Chapter 1 summarizes the background of medical-grade Ti6Al4V and its applications, the motivation for this research, and the effect of additive manufacturing in the future of orthopedic and biomedical industries.
- Chapter 2 is a literature review of the microstructure and phases of Ti6Al4V ELI. Metal additive manufacturing and processes that are used for Ti6Al4V manufacturing and post-processing that is necessary after 3D printing are fully discussed in this chapter. Moreover, it includes a literature review of the possible wear mechanisms found after wear test on Ti6Al4V. The chapter ends with the proposed research's main objectives.
- In chapter 3, two-material manufacturing processes (conventional and 3D printing) and preparations are explained. Also, the heat treatment process and other experimental procedures are described in detail.
- Chapter 4 is devoted to the results of heat treatment effects on microstructure and mechanical properties of conventional and 3D printed medical-grade Ti6Al4V.

- Chapter 5 discusses the results and compares them with other research results.
- Finally, Chapter 6 concludes the results captured from this research.

Chapter 2 Literature Review

2.1 Ti6Al4V Alloy information

Titanium consists of two main crystal structures, hexagonal close-packed (HCP) α phase and body-centered cubic (BCC) β phase (Fig 2.1). Temperature and alloying elements have an effect on the microstructure and define the type of alloy [11]. Elements such as Aluminum and Tin stabilize the α phase by increasing the transition temperature. Pure titanium has a transition temperature of about 882°C at which the transformation of HCP to BCC happens. Elements such as Vanadium, Molybdenum, and Chromium are the β phase stabilizers and by decreasing the transition temperature, this will bring more β phase to the alloys [11]

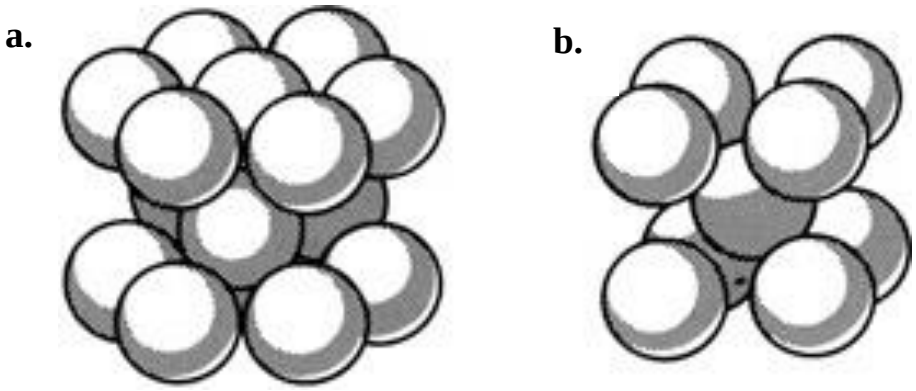

Figure 2.1 Crystal structures of Titanium. a. Hexagonal close-packed (HCP) b. Body-Centered Cubic (BCC) [11]

Generally, due to the allotropic transformation, which can be caused by either alloying or changing the temperature, titanium alloys are divided into three main alloy groups.

2.1.1 α alloys

α alloys are formed as a result of titanium alloying with Al, O, N, and C which are the α stabilizer elements. Among all these elements, aluminum and oxygen have the highest solubility properties which enable them to dissolve better. On the other hand, alloying with aluminum reduces the density and brings ductility to the alloy [12]. Ti5Al2.5Sn is an example of titanium α alloy and these alloys are known for their strength, toughness, and creep resistance [13]

2.1.2 α+β alloys

These alloys consist of one or two α stabilizer elements and one or two β stabilizer elements which make them a mixture of α and β phase at room temperature [13]. Alloys such as Ti6Al4V and Ti6Al2Sn6V are two well-known α+β alloys. The mechanical properties of these alloys are controlled by heat treatment. Therefore, a wide range of microstructure and mechanical properties can be produced in these alloys. Generally, α+β alloys have high strength at room temperature and good fabricability.

2.1.3 β alloys

Generally, all β alloys contain a large amount of one or two β stabilizer elements like Vanadium, Niobium, Tantalum, and Molybdenum. Despite α alloys' stability, β alloys are metastable and heating or cold work at room temperature may result in the transformation to the α phase. All β alloys have excellent formability, good ductility, and toughness. Since beta is a metastable phase, by heating this alloy, alpha phase precipitation happens. Thus, this alloy is not the best choice for application influenced by temperature, although fracture toughness improves by temperature increase [13].

Ti6Al4V with 6% Aluminum as the α stabilizer and 4% Vanadium as the β stabilizer categorize as the α+β alloy at room temperature [14]. There are two different grades of this alloy available and being used in different industries. Grade 5 of Ti6Al4V is mainly used in aerospace and automotive industries while the grade 23 or the ELI Ti6Al4V has a wide application in medical industries. The main difference between grade 5 and grade 23 is the lower percentage of Oxygen, Nitrogen, and Iron in grade 23 which results in ductility and fracture toughness improvement. Therefore, grade 23 of Ti6Al4V is the best choice when a combination of high strength, light weight, good corrosion resistance, useful formability, and high toughness is required. Above all, the ELI grade has a superior damage tolerance compared to the other grades [2]. The main focus of this thesis is on medical-grade Ti6Al4V ELI with extra-low interstitials of oxygen and nitrogen.

2.2 Ti6Al4V Application

Because of titanium alloys' exceptional characteristics and mechanical properties, titanium-based materials are widely used in industries such as aerospace and biomedical engineering [15]. This

alloy was first used in 1950 for aircraft applications. Because of its lightweight, Ti6Al4V has been a suitable option for jet engines, gas turbines, and aircraft frames. As time passed by, more industries became interested in Ti6Al4V attractive characteristics [16]–[19].In the last few decades, Ti6Al4V alloys have been used in dental and bone-implant which is due to their excellent biocompatibility to human body tissue, great corrosion resistance and the good strength-weight ratio [20]. Recently, total hip replacement is one of the most common orthopedic surgeries [21]. The implanted hip has a life expectancy of 10 to 15 years, although almost half of the patients who are in need of implants are younger than 70 years old. Thus, there is a high risk of a new surgery and operation.

2.3 Additive Manufacturing

Conventional manufacturing is a process of manufacturing structures by removing material. Different types of conventional manufacturing are such as turning, milling, grinding, drilling, CNC machining, injection molding, forging, and casting. Disadvantages such as the high amount of material waste are binging more attention to additive manufacturing [21].

Additive manufacturing defines as a process of building structures in the form of three-dimension by joining material layer by layer [22]. Additive manufacturing is also known as additive fabrication, additive processes, direct digital manufacturing, solid freeform fabrication, and 3D printing manufacturing. Investigation in additive manufacturing methods started in the late 1980s [23]. The early 3D printing materials were resin, polyamide, wax, ABS, polycarbonate, metal, metal/ceramic/polymer powders, etc. which were built layer by layer from the CAD models [24]. In the past two decades, 3D printing manufacturing has been applied in industries such as automotive, biomedical, and aerospace [22], [25]–[27]. In general, additive manufacturing technology brings improvement in industries by decreasing the lead time, bringing more possibilities to manufacturing complex structures, and cost-saving in single parts manufacturing [24].

Additive manufacturing processes are divided into four categories according to the state of the starting material used. Table 2.1 summarizes the four states of starting material: liquid, filament/paste, powder, and solid sheet.

Table 2.1 Four categories of AM process according to the state of starting material used [28]

State of starting material	Process	Material preparation	Layer creation technique	Phase change	Typical materials	Applications
Liquide	SLA	liquid resin in vat	Laser scanning/ light projection	photopolymerization	UV curable resin, ceramic suspension	prototypes, casting patterns, soft tooling
	MJM	liquid polymer in jet	Ink jet printing	Cooling and photopolymerization	UV curable acrylic plastic, wax	prototypes, casting patterns
	RFP	liquid droplet in nozzle	On demand droplet deposition	Solidification by freezing	water	prototypes, casting patterns
Filament/paste	FDM	Filament melted in nozzle	continuous extrusion and deposition	Solidification by cooling	Thermoplastics, waxes	prototypes, casting patterns
	Robocasting	paste in nozzle	continuous extrusion	-	Ceramic paste	Functional parts
	EFE	paste in nozzle	continuous extrusion	Solidification by freezing	Ceramic paste	Functional parts
Powder	SLS	Powder in bed	laser scanning	Partial melting	Thermoplastics, waxes, metal powder, ceramic powder	prototypes, casting patterns, metal and ceramic performs (to be sintered and infiltrated)
	SLM	Powder in bed	laser scanning	Full melting	Metal	Tooling, functional parts
	EBM	Powder in bed	Electron beam scanning	Full melting	Metal	Tooling, functional parts
	LMD	powder injection through nozzle	On demand powder injection and melted by laser	Full melting	Metal	Tooling, metal part repair, functional parts
	3DP	Powder in bed	Drop on demand binder printing	-	polymer, metal, ceramic, other powders	prototypes, casting shells, tooling
Solid sheet	LOM	Laser cutting	feeding and binding of sheets with adhesives	-	paper, plastic, metal	prototypes, casting models

2.3.1 Powder-based additive manufacturing

Basically, in powder base additive manufacturing, materials are used in the form of powder and a localized heat source is used to build a structure layer by layer. Powder bed fusion technique consists of different processes that are used based on the material and applications. SLS or Selective Laser Scanning is one of the powder bed fusion techniques in which the powder is sprayed in a layer then based on the desired structure, the powder gets scanned selectively by a

laser. SLS processes can cover a wide range of material types such as a polymer, wax, metal, ceramics, polymer/metal powders [29], [30]. In this technique, the powder is partially melted, while in SLM (Selective Laser Melting) full melting happens. SLM technique is mainly used for metallic parts and is derived from a selective laser scanning technique. The final products are very dense and normally no post-processing is required which makes them have better mechanical properties than the conventional manufactured metals [31]–[34]. DMLS (Direct Metal Laser Sintering) is another additive manufacturing method that is used for metal manufacturing. A schematic of this manufacturing process is shown in Fig 2.2. DMLS is similar to SLM with the difference that in SLM there is complete melting while in DMLS only partial melting happens [35].On the other hand, DMLS and SLS have a lot in common while SLS is mostly used for non-metal applications [36]. Electron Beam Melting (EBM) is another powder additive manufacturing process in which an electron beam is used as a source of energy. EBM is used for metal manufacturing and the final products are better than SLM products due to the strength and higher energy that is received from an electron beam versus that of a laser. The negative side of this manufacturing technique is its surface finish [37]–[42]. LMD or Lase Metal Deposition which is also known as Laser Engineered Net Shaping (LENS) is similar to the SLM technique with the difference that in LMD the powder is fed via a nozzle while in SLM the structure is made in a powder bed. The product of this technique is very dense, and no post-processing is needed [43]–[48]. Besides all the good features of this manufacturing technique, due to difficulties in controlling a large amount of energy used for melting metal powders, issues such as balling, high residual stress and part deformation may occur [31] which are discussed fully in section 2.3.4 of this thesis.

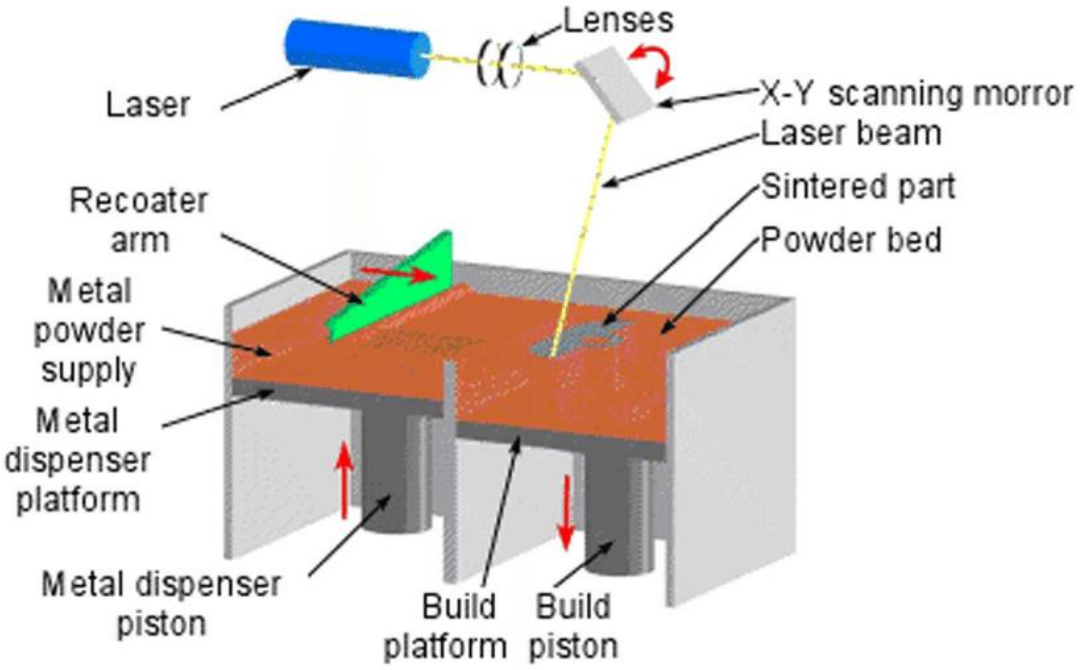

Figure 2.2 Schematic of Direct Metal Laser Sintering (DMLS) process [49]

2.3.2 Metal Additive Manufacturing

The first additive manufacturing technology was able to produce plastic prototypes and parts. Development in AM technology enables industries to 3D print metals via EBM and SLM. More improvement resulted in producing complex net-shaped metallic products. In general, metal additive manufacturing is either done directly or indirectly.

2.3.2.1 Indirect Metal 3D Printing

Binder is used in the indirect AM process to attach and hold the structure. Binder can be either polymer or a low melting point metal. Products that are made in indirect metal AM require post-processing in order to remove the binder and form a fully dense structure. SLS, FDM, SLA, 3DP, and LOM are the metal additive manufacturing processes that indirect process is used in them [50], [51].

2.3.2.2 Direct Metal 3D printing

Metal manufacturing can also be done in the direct method. In SLM and EBM process no binder usage is necessary since a high-power laser or electron beam is used as the energy source to fully melt the powder. This manufacturing method results in great mechanical properties which at some point, these mechanical properties may be better than the conventional products. Titanium alloys such as Ti6Al4V and Ti6Al4V ELI are mainly manufactured by direct metal 3D printing [35], [52], [53].

2.3.3 Additive manufacturing application in orthopedic application

Improvement in 3D printing and biomedical industry brought interest in manufacturing orthopedic implants, artificial organs and medical devices [54]. The benefits that additive manufacturing is bringing to orthopedic implants are the ability to manufacture complex structures and geometries, produce stiff and effective bone implants with tissues similar to bone integration, and above all, customizing implants to match patient's needs. Arcam, Adler Ortho Group, Concept Laser and MTT Technologies are examples of companies manufacturing orthopedic and dental implants using additive manufacturing techniques like SLM and EBM [55], [56].3D printed Ti6Al4V alloys due to their superior mechanical properties, biocompatibility, and similarities to bone stiffness have attracted scientists' attention with EBM and SLM as the two techniques used to fabricate implant parts [44], [57].

Figure 2.3 Additive manufactured hip implant cup [58]

2.3.4 Additive Manufacturing Defects

Besides all the great features that additive manufacturing has, this manufacturing method can be limited by the number of defects. Porosity, rough surface finish, and residual stresses are some examples of flaws that additive manufactured produces may have. Each defect influences the

mechanical properties of as-built products. In this section, more details are discussed regarding additive manufactured Ti6Al4V.

2.3.4.1 Porosity

Although controlled porosity can be beneficial for Ti6Al4V implants to reduce stress shielding effect and impacts, uncontrolled porosity in a full dense structure happens as a result of non-optimal deposition parameters and has a negative impact on mechanical properties [20], [59]–[62]. Researches have shown that porosities' shapes and orientations have effects on product ductility. Also, adiabatic shear bands and microcracks are more possible at the pores' locations [63]–[65]. Porosity appearance is very common in additive manufacturing products, but their size can be controlled by post-processing techniques such as heat treatment and HIP which researches show to have an improvement in AM products [66]. Generally, pores in 3D printing are divided into two groups: gas pores and lack of fusion pores. Gas pores appear randomly in AM materials as spherical or elliptic shape (Fig 2.4.a). It is believed that gas pores form as a result of gas entrapment and to eliminate their formation during 3D printing, usage of a laser with higher energy and reducing the scan speed may help [67]–[72]. On the other hand, lack of fusion pores which are shown in Fig 2.4.b have an irregular shape with sharp edges and appear to be larger than the spherical pores. They form as a result of deflection in the melting condition. For example, low power laser usage or melting an extra amount of powder will result in a lack of fusion pores due to insufficient melting and forming weak bonding between layers. That explains the formation of the irregular pores at the boundaries which seem like a flat crack [63], [73].

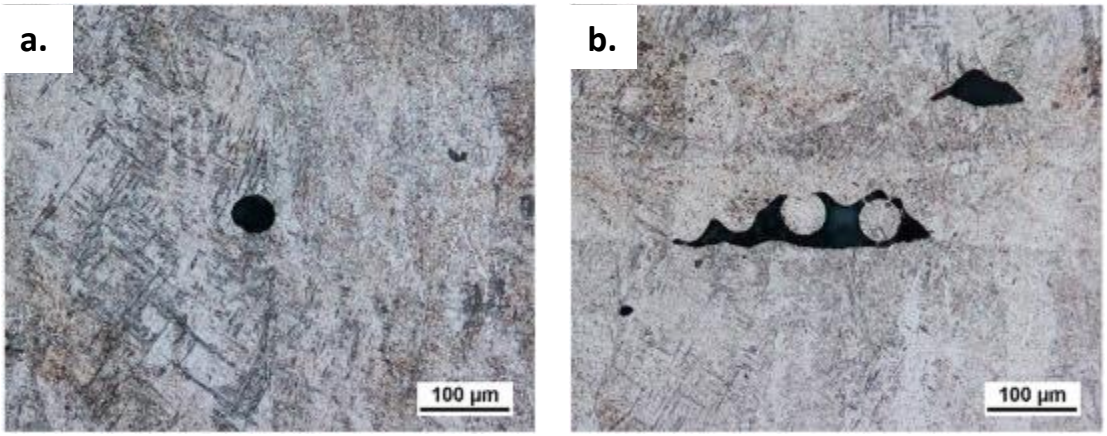

Figure 2.4 a. Spherical or gas pores b. Irregular shaped or lack of fusion pores [67]

2.3.4.2 Surface roughness

High surface roughness is one of the disadvantages of additive manufacturing which makes almost all the products from this manufacturing type, dependent on postprocessing [74]. Surface roughness of different AM processes varies. Also, by changing the parameters like scanning speed, powder size, and each layer height in each additive manufacturing process, surface roughness can be improved. Li el al claimed that there are three reasons for surface roughness formation. Staircase phenomena is one of the reasons for a rough surface (Fig 2.5) which can be controlled by the number of layers and the bonded layers' angle. The other reasons are the not fully melted powders at the external surface and appearance of open uncontrolled pores [75]. The most effective post-processing in order to reduce surface roughness is polishing. Research has shown that polished samples show higher strain to failure, which is due to removing critical defects and cracks from the surface [73].

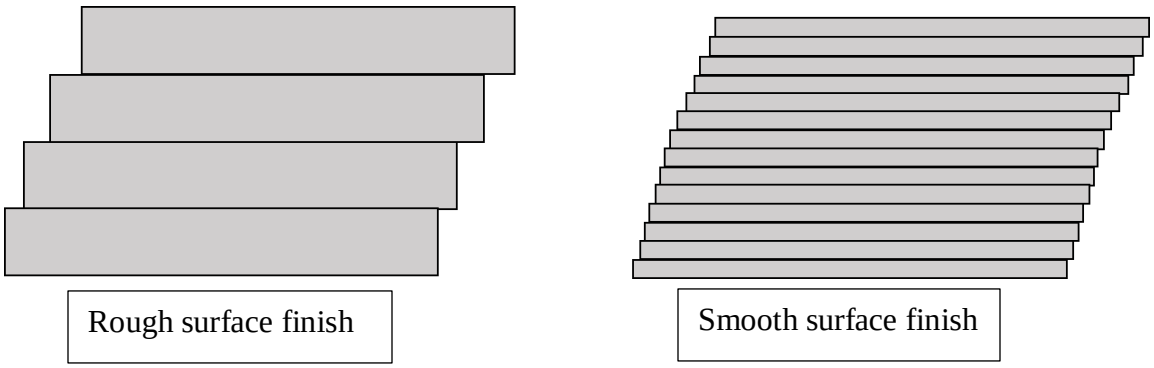

Figure 2.5 Appearance of staircase phenomena in AM products

2.3.4.3 Residual stresses

Rapid heating and cooling cycles in additive manufacturing processes cause residual stresses in specimens [76]. Residual stress rises by increasing the number of layers and usually, the free surface has the highest residual stress value [77]. Moreover, the scanning angle has an effect on residual stresses. Higher residual stresses can be found along the scan direction while lower stress was observed at spots that the scanning direction was perpendicular. In addition, by increasing the scan length, residual stress rises [78]. Residual stress is one of the reasons for material failure since it can cause crack formation and geometrical disorientation in certain parts [78]. To improve AM materials' quality regarding residual stresses, Vastola et al. [77] claimed that by preheating the

fusion bed, the thermal gradient will be reduced. Therefore, by increasing the bed fusion temperature by 50°C, residual stress can be reduced by about 20%. Since in the EBM process for Ti6Al4V the building temperature is about 600 to 750°C, the thermal gradient is low and compared to SLM manufacturing, EBM has lower residual stress [79]. Heat treatment is also used as a post-processing technique to reduce residual stress in as-built materials. Stress-relieving in titanium alloy is dependent to time, temperature and chemical composition of alloys. According to ASM standard for Ti6Al4V, stress relieving process needs to be done for 1 to 4 hours at temperature between 480 to 650°C [13].

Figure 2.6 Crack Formation as a result of residual stress build-up during the manufacturing process [80]

2.3.4.4 Non-equilibrium phases

According to the phase diagram, slow cooling from over β transus temperature (β phase region), generally results in an α phase formation and an equilibrium microstructure of α and β phase mixture. A high cooling rate is used in the additive manufacturing process. Therefore, non-equilibrium metastable phases such as α' are formed [81]. The temperature gradient between layers is the main reason for non-equilibrium phase formation. Post-processing like heat treatment can reduce these metastable phases.

2.3.4.5 Balling or over melting

Balling happens as a result of insufficient laser processing parameters such as its speed and energy. Due to unfavorable laser parameters melted powder instead of spreading equally on a certain layer, they break into droplets. The droplet formation is known as balling which is one of the defects in additive manufacturing. Balling phenomena can result in a poor surface finish. The formation of

balling is strongly influenced by the melted powder and the solid surface temperature [82]. Post-processing like polishing the surface finish can improve the balling effect.

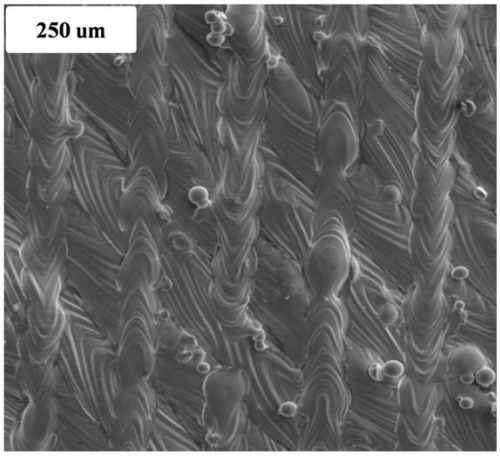

Figure 2.7 Micrograph of Balling Formation in additive manufacturing process [83]

2.4 **Heat Treatment**

Studies have shown that the microstructural and mechanical properties of the materials such as Ti6Al4V can be influenced by post-processing heat treatment [84]. The post-processing heat treatments can reduce residual stresses and bring more equilibrium microstructure to the structure [85]. According to the ASM standard, the heat-treating process is accomplished for several reasons: 1. Relieving stresses that were developed during fabrication 2. To bring sufficient ductility, stability, and machinability to structure 3. To increase strength and 4. To improve the mechanical properties of alloys such as fracture toughness, fatigue strength, and high temperature creep strength based on the application [13].

Various heat treatment types in titanium alloys result in different microstructure and mechanical properties. Also, depending on the alloy's phase condition, different microstructures are expected. Beta transus point is a temperature that differs in alloys with different chemical composition and it is an important temperature in the heat treatment process. Ti6Al4V ELI's beta transus temperature is about 975°C [86], which makes this alloy have a fully β structure above 975°C and below this temperature, Ti6Al4V behaves as an α+β alloy. The cooling rate is another factor in heat treatment that may cause different microstructures in alloys. For instance, by air cooling an alpha-beta alloy like Ti6Al4V after solutioning it at

above beta transus temperature, widmanstätten α, and β colony microstructures will be observed, while water quenching results in martensitic α structures (α' and α") [87].

As it was mentioned above, based on different applications, the heat treatment process may vary. For example, the aging process is used in α+β alloys to improve strength, while annealing increases ductility and toughness of titanium alloys [13].

2.4.1 Annealing

Annealing treatment is commonly called the solution treatment or stress relief heat treatment that has four different kinds: 1. Mill annealing 2. Duplex annealing 3. Recrystallization annealing, and 4. Beta annealing. The main purpose of annealing is to bring toughness and ductility at room temperature to alloys [13].

2.4.2 Aging

Aging is another heat-treating process that improves the strength of titanium alloys. It is a process of reheating specimens at about 425 to 650℃ to reach the highest strength. Aging results in the transformation of hexagonal α' and orthorhombic α'' crystal structures to alpha and sustainability of the decomposition of the supersaturated beta phase [13].

2.4.3 Heat treating effects on Ti6Al4V ELI

Research has been done on the effect of heat treatment on Ti6Al4V ELI by H. Galarraga and R.J. Warren and they reported that the heat treatment parameters such as cooling rate need to be chosen based on the alloys' application [67]. They reported that fast cooling speeds result in a fully α' martensitic while the air-cooled samples contain fewer martensitic structures [67]. Additive manufactured Ti6Al4V alloys go through multiple phase transformations due to temperature fluctuation during manufacturing [88]. First, the α+β powder is heated above beta transus and turn to liquid and then the cooling process happens, and the alloy goes back to β and then to α, α', and β, and the same process goes on for the next layers [88]. Fig 2.8 shows Ti6Al4V alloy's phase diagram. By heating Ti6Al4V to 1050℃ which is slightly over beta transus temperature, the whole alloy's phase turns to β. Fast cooling or water quenching of the

alloy at this condition result in a mixture of α' martensite and β phase. On the other hand, air cooling the alloy result in lamellar α+β structure and α grain boundaries appears.

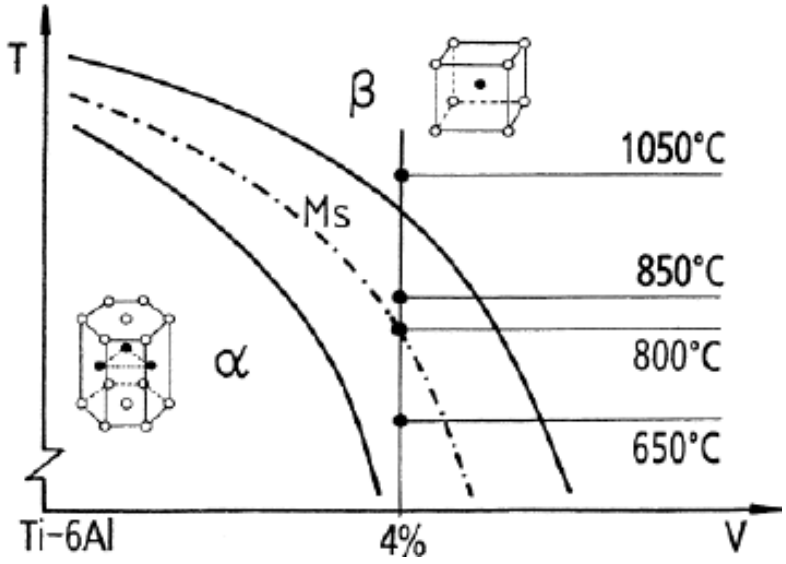

Figure 2.8 Ti6Al4V Phase Diagram [89]

2.5 **Wear Mechanism**

Tribology is the science of studying wear and friction. Wear happens as a result of friction between surfaces in contact. In order to measure and monitor the wear of materials, it is essential to understand different types of wear mechanisms. In general, there are four main types of wear mechanism; Adhesive wear, Abrasive wear, Fatigue wear, and Corrosive wear [90].

2.5.1 Adhesive Wear

This type of wear happens as a result of two surfaces sliding against each other and the friction caused by this cold-welds the roughness of one surface to another one. Thus, some material transformation occurs as a result of adhesive wear and the amount of material transferred is dependable to the area of the contract. Fig 2.9 shows a schematic of the adhesive wear mechanism [90].

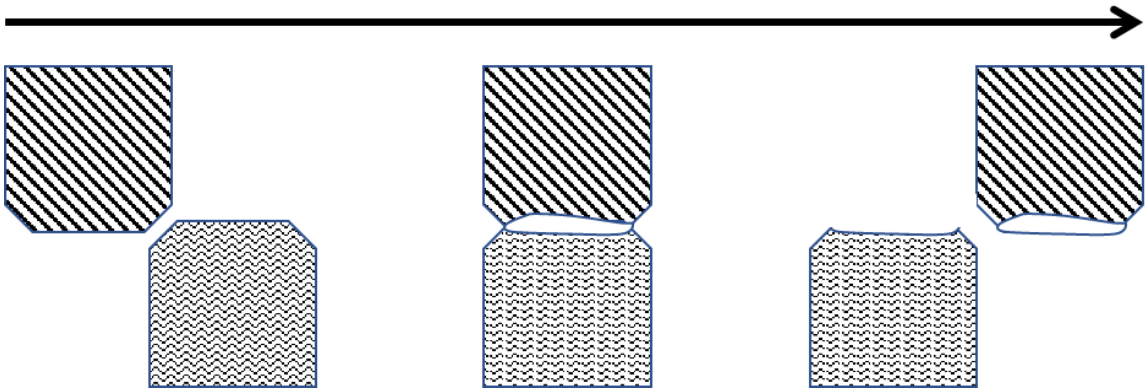

Figure 2.9 Schematic of adhesive wear mechanism showing from left to right the process of meeting, friction and adhesion, and finally the separation, respectively.

2.5.2 Abrasive Wear

Abrasive wear is the most common type of wear and it happens as materials with different hardness slide against each other (Fig 2.10). This type of wear is controlled by the materials hardness, geometry of the materials in contact, load and sliding distance. Abrasive wear can happen between more than two surfaces which are called two-body and three-body abrasion when there are two and three surfaces in contact, respectively. Material can also be cut by a high velocity flowing liquid which is known as erosion which is another type of abrasive wear [91].

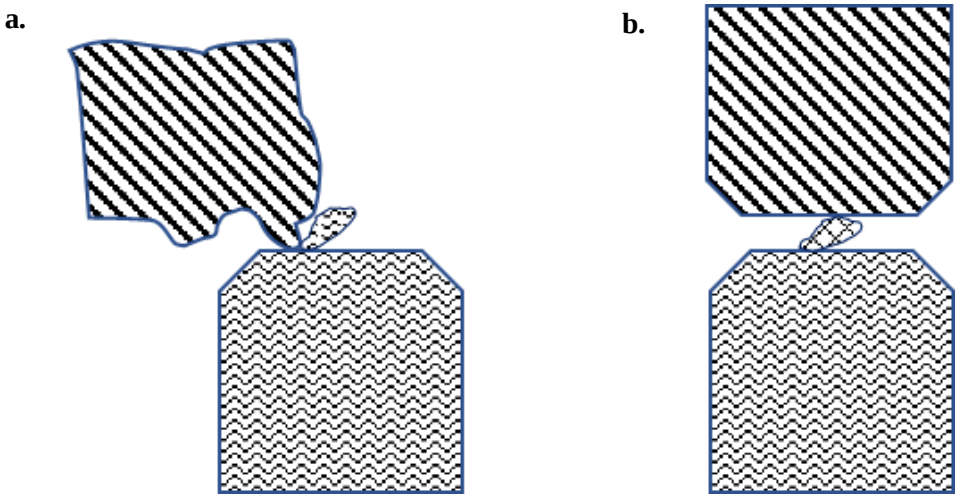

Figure 2.10 Schematic of abrasive wear. a. two-body abrasion b. three-body abrasion

2.5.3 Fatigue Wear

As a result of two surfaces sliding against each other, a zone of compression and tension is created ahead and behind the motion, respectively. This compression and tension initiate a crack formation and as the cycle repeats, the crack enlarges and reaches the surface. Material loss and debris produced because of the fatigue wear may result in the three-body abrasive wear. Fig 2.11 shows a schematic of the fatigue wear as well as tension and compression zones[92].

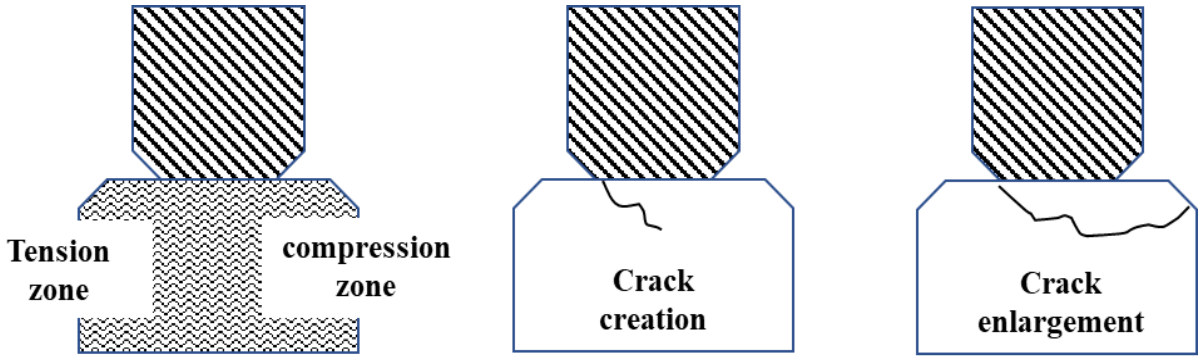

Figure 2.11 Fatigue wear schematic. a. tension and compression zone, b. crack initiation c. the crack grows as the cycle goes on until failure happens.

2.5.4 Corrosive Wear

Corrosion wear (Fig 2.12) happens when a surface is exposed to a chemical and the reaction layer is getting removed after each slide between two surfaces. Basically, after each slide, a fresh surface is getting exposed to the chemical which is going to be removed at the next cycle [90].

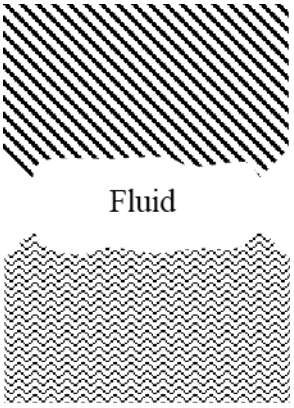

Figure 2.12 Schematic of corrosion wear and the reaction of materials' surface with corrosive fluid.

Chapter 3 Material and Experimental procedure

3.1 Material Processing and Preparation

A pre-alloyed powder (AP&C's Ti-6Al-4V, Quebec, Canada) manufactured using the proprietary APATM Plasma Atomization process, producing highly spherical powders containing virtually no entrapped porosities with minimal satellite content, resulting in truly exceptional flowability and packing density were used. Direct Metal Laser sintering (DMLS) method was used to manufacture cylindrical parts of 25×10 mm. All the 3 printed samples were manufactured at "Precision ADM" located at Winnipeg, Canada. Precision ADM is a known manufacturer for medical implant 3D printing. To sum up the DMLS 3D printing method, the STL file of the cylindrical part is fed to the printer. At each stage of the printing, a roller spread a thin layer of Ti6Al4V powder on the base of the work followed by heating up the print chamber of the 3D printer. Then a high energy laser is used to raise the temperature of the powder for those areas that are part of the design to just above the melting point. This action at each layer fuses the powder together. This is repeated until the final layer is attached together [93]. The post-processing at ≥500℃ for 2 hours followed by oven cooling in a non-inert atmosphere using an ISO 13485-certified multi-step manufacturing plan for medical devices was done right after 3D printing those cylindrical parts. For investigation purposes, a baseline was introduced to compare the 3D printing parts with, and this baseline was consisting of cylindrical parts of 25×10 mm of conventionally processed Ti6Al4V ELI. These conventionally manufactured alloys were casted and extruded into cylindrical shapes at "Titanium JOE" located at Kingston, Canada. The chemical composition of the Ti6Al4V alloy is shown in Table 3.1.

Table 3.1 Chemical composition of Ti6Al4V ELI (wt%) from ASTM F136 standard [94]

Alloy type	Composition							
Ti6Al4V ELI	Ti	V	Al	O	Fe	H	C	N
	Balance	3.5-4.5	5.5-6.5	<0.13	<0.25	<0.012	<0.08	<0.05

3.2 Heat treatment

To understand the effect of heat treatment on the evolution of the microstructure and mechanical properties of medical-grade Ti6Al4V, DMLS manufactured samples were heat treated. First, all samples were divided into two groups to study the effect of cooling rate on their structures and properties. For better tracking the sequence of events that happen to the specimens after heat treatment, both groups were heat-treated in a furnace to above beta transus for solutionizing. The temperature chosen for solutionizing was 1080℃ and all samples were kept at this temperature for 4 hours prior to aging. Group 1 samples were air-cooled while samples in group 2 were water quenched right after solutioning from the 1080℃-4 hours. All samples in the two groups were then aged at 200 ℃, 500 ℃, and 800 ℃ for 4 hours followed by air cooling. Figure 3.1 shows a schematic of the process used for heat-treating the 3D printed samples. The whole heat treatment procedure was repeated for conventional medical-grade Ti6Al4V samples which were chosen at the comparison baseline. Also, a list of the18 samples with their names used in this thesis is shown in Table 3.2.

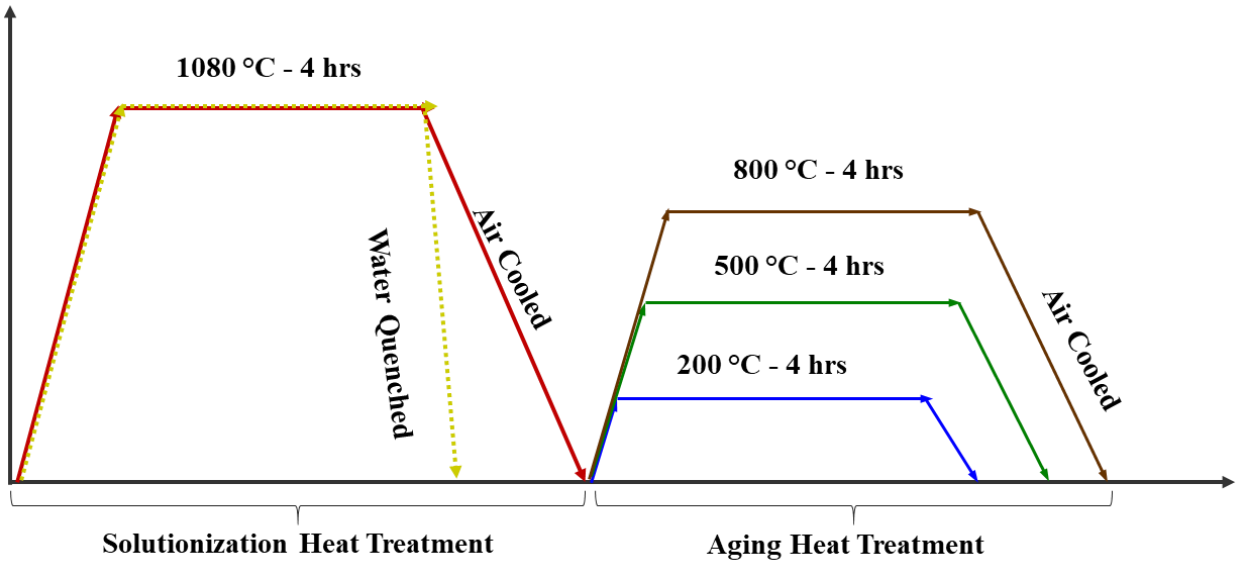

Figure 3.1 Schematic of heat treatment conditions of Ti6Al4V alloy.

Table 3.2 Sample's symbol and their descriptions.

#	Symbol	Sample Description
1	AR-CV	As Received Conventional
2	AR-3D	As Received 3D printed
3	AC1080-CV	Solutionized at 1080℃ followed by air-cooling-Conventional
4	AC1080-3D	Solutionized at 1080℃ followed by air-cooling-3D Printed
5	AC200-CV	Solutionized at 1080℃ followed by air-cooling + aged at 200℃-Conventional
6	AC200-3D	Solutionized at 1080℃ followed by air-cooling + aged at 200℃-3D Printed
7	AC500-CV	Solutionized at 1080℃ followed by air-cooling + aged at 500℃-Conventional
8	AC500-3D	Solutionized at 1080℃ followed by air-cooling + aged at 500℃-3D Printed
9	AC800-CV	Solutionized at 1080℃ followed by air-cooling + aged at 800℃-Conventional
10	AC800-3D	Solutionized at 1080℃ followed by air-cooling + aged at 800℃-3D Printed
11	WQ1080-CV	Solutionized at 1080℃ followed by water-Quenching-Conventional
12	WQ1080-3D	Solutionized at 1080℃ followed by water-Quenching-3D Printed
13	WQ200-CV	Solutionized at 1080℃ followed by water-quenching + aged at 200℃-Conventional
14	WQ200-3D	Solutionized at 1080℃ followed by water-quenching + aged at 200℃-3D Printed
15	WQ500-CV	Solutionized at 1080℃ followed by water-quenching + aged at 500℃-Conventional
16	WQ500-3D	Solutionized at 1080℃ followed by water-quenching + aged at 500℃-3D Printed
17	WQ800-CV	Solutionized at 1080℃ followed by water-quenching + aged at 800℃-Conventional
18	WQ800-3D	Solutionized at 1080℃ followed by water-quenching + aged at 800℃-3D Printed

3.3 **Metallographic Analysis and Microstructural Characterization**

To study the samples' microstructure and properties after heat treatment procedure, basic metallographic techniques such as mounting, grinding, polishing, etching, microscopic analysis, hardness, and wear testing were used. Right after heat treatment, all samples were hot mounted.

To remove oxide later and achieve a smooth surface, all specimens were ground with 180, 400, 600, 800, and 1200 grit Silicon Carbide papers. Grounding was followed by polishing with alumina suspension to attain a mirror-like surface finish. Kroll's (2% HF+ 4% HNO_3) was used as an etchant to enable samples' microstructures to be detected and examined at each heat-treated

condition. Samples were soaked in the etchant for about 30 seconds and it was followed by immediate water and ethanol cleaning, respectively. Optical Microscope (OM) and Scanning Electron Microscope (SEM) were used to study different structures of Ti6Al4V samples. One of the equipment used to investigate this alloy's mechanical properties was Micro Vickers Hardness tester. The hardness of the samples was measured by applying a 300 gf (gram-force) or 2.94 N force for 15 seconds on the samples. A total of 15 indentations away from the samples' edge were recorded and their average values calculated as the hardness value of the sample.

3.4 Surface Roughness Measurements and Wear Tests

To measure the surface roughness of the mirror-like surface of samples, Bruker Contour GT optical profilometer device was used. This device is equipped with two different lights which in this study the white light was used to detect the surface roughness of each sample. This measurement was done prior to each wear test to ensure that all the specimens' surface roughness is within the acceptable range. Standard used for the surface roughness investigation was ISO 25178 in which a high and low pass filter were used, respectively, to smooth the asperities of the polished surface. The average of seven roughness measurement in the form of area surface measurement (S_a) for each sample is shown in Table 3.3 for both 3D printed and conventional manufactured Ti6Al4V.

Table 3.3 Surface roughness of Ti6Al4V alloys at different heat treatment conditions (nm).

Condition	As received	WQ1080	WQ200	WQ500	WQ800	AC1080	AC200	AC500	AC800
Conventional	1.437	1.208	1.487	1.628	1.376	0.989	1.246	1.202	0.964
3D printed	1.573	1.896	1.504	1.569	1.222	1.320	1.591	1.473	1.791

Wear test was the other method used to investigate the mechanical properties of medical-grade Ti6Al4V alloy. The UMT Tribolab (Brucker Tribometer, Canada) wear equipment was used for a ball-on-disc rotary wear test with lubricants. Fig 3.2.a shows a configuration of this equipment. The standard used for this test was ASTM G99-05 (2010) in which a 9.525 mm diameter spherical high strength grade 5 Ti6Al4V was used as the counter body in the test. The ball was cleaned as well as weighted before and after each test. Right after ball measurement, it was secured in the

designed holder. The polished disc-shaped sample which is shown in Fig 3.2.b with a dimension of 25×4 mm was cleaned, dried by high pressured air, and weighted prior to getting secured by a screw in the center to the bottom of the chamber. The chamber was filled with 9g/L Sodium Chloride as Lubricant to fully cover the sample's surface. The test was done in two stages. In the first stage, a preload of 10 N was applied to the titanium alloy ball for 60 s. The main reason for this step was to ensure smooth engagement of the contact surface before the beginning of the major stage of the test and to examine the force sensor sensitivity. The second and the main stage started by continuing the constant normal load of 10 N for 90 mins while the spherical ball rotated with a velocity of 106.5 rpm. The temperature for the test was kept at 37℃ to simulate human body temperature in which the chamber temperature was set to 37℃ at the beginning of the first stage.

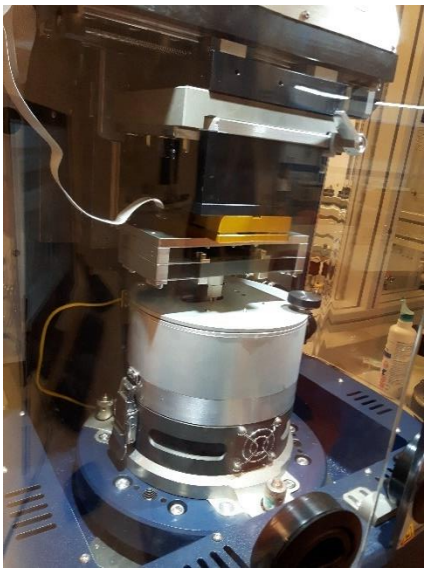

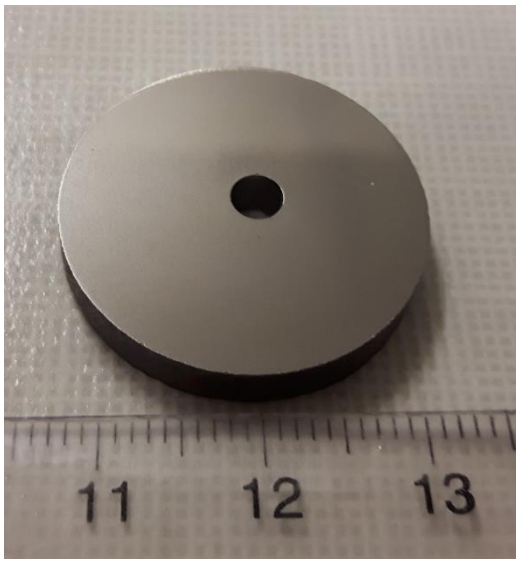

Figure 3.2 a. Ball on disc rotary wear test machine with the temperature-controlled chamber. b. The disc-shaped specimen used for the rotary wear test.

For all conditions, the ball and the specimen's mass were measured before and after each test. Also, in order to find out the reasons behind the different wear rates of each condition, wear mechanisms of wear tracks were studied by optical microscope.

3.5 **Electron Probe Micro Analyzer (EPMA)**

EPMA was used to analyze the chemical composition of the v-shaped microstructure. The fundament of both EPMA and SEM is the same. However, EPMA is mainly designed for quantitative analysis, while, SEM is primarily designed for high-resolution imaging.

Microanalysis and XRD results helped in realizing the crystal structure of the V-shaped microstructure as well as the grain boundaries.

3.6 X-Ray Diffraction Analysis on The Medical Grade Ti6Al4V

2D diffraction data were collected at the MAX Diffraction Facility at McMaster University using a Brucker D8 DISCOVER diffractometer. The diffraction phases in all the samples were analyzed using X-Ray diffraction (XRD) with Cu/K alpha radiation with a wavelength of 1.054056 Å using an X-ray source operated at 40kV and a 40mA current at room temperature with the exposure time of 300s/frame within 2θ range of 15 to 100°. The XRD patterns phase identifications were carried out using MDI Jade 6.5 software.

Chapter 4 Results

4.1 The microstructure of the As-printed Ti6Al4V Alloy

Generally, the mechanical properties of titanium alloys are affected by morphology and distribution of α and β phases. It has been shown that the density and size of the α phase has a direct influence on the mechanical properties of Ti6Al4V ELI [95]. Figure 4.1 shows the surface of an etched Ti6Al4V sample which generally reveals the grains after etching.

Figure 4.1 The surface of Ti6Al4V sample after chemical etching

Figure 4.2 shows an Optical microscope (OM) and scanning electron microscope (SEM) micrographs of the as-printed 3D printed Ti6Al4V ELI at different magnifications. Generally, two forms of lath morphologies were observed within the grains. One morphology comprised of basketweave structures (Figure 4.2 (a)) whiles the other morphology was made up of lath-like structures with single orientations as shown in Figure 4.2 (b-d). The basketweave structures were made up of laths with 2 orientations which were generally at 90° to each other. The lath-like structures were usually colonies of lath with single lath orientations. The lath-like structures were more distinct and developed than the basketweave structures as shown in Figure 4.2. In addition, few surface micropores were observed in the as-printed specimen as shown in Fig 4.2 (d-f). Figure 4.3 shows the microhardness indentation on the as-printed Ti6Al4V ELI. The average microhardness value recorded for this sample was 402 HV. However, microhardness values were different for the two specific morphologies (lath-like and basketweave structures). The lath structures exhibited a higher average microhardness value of 411 HV whiles the short basket weave structures exhibited an average microhardness value of 395 HV as shown in Fig 4.3(a-d).

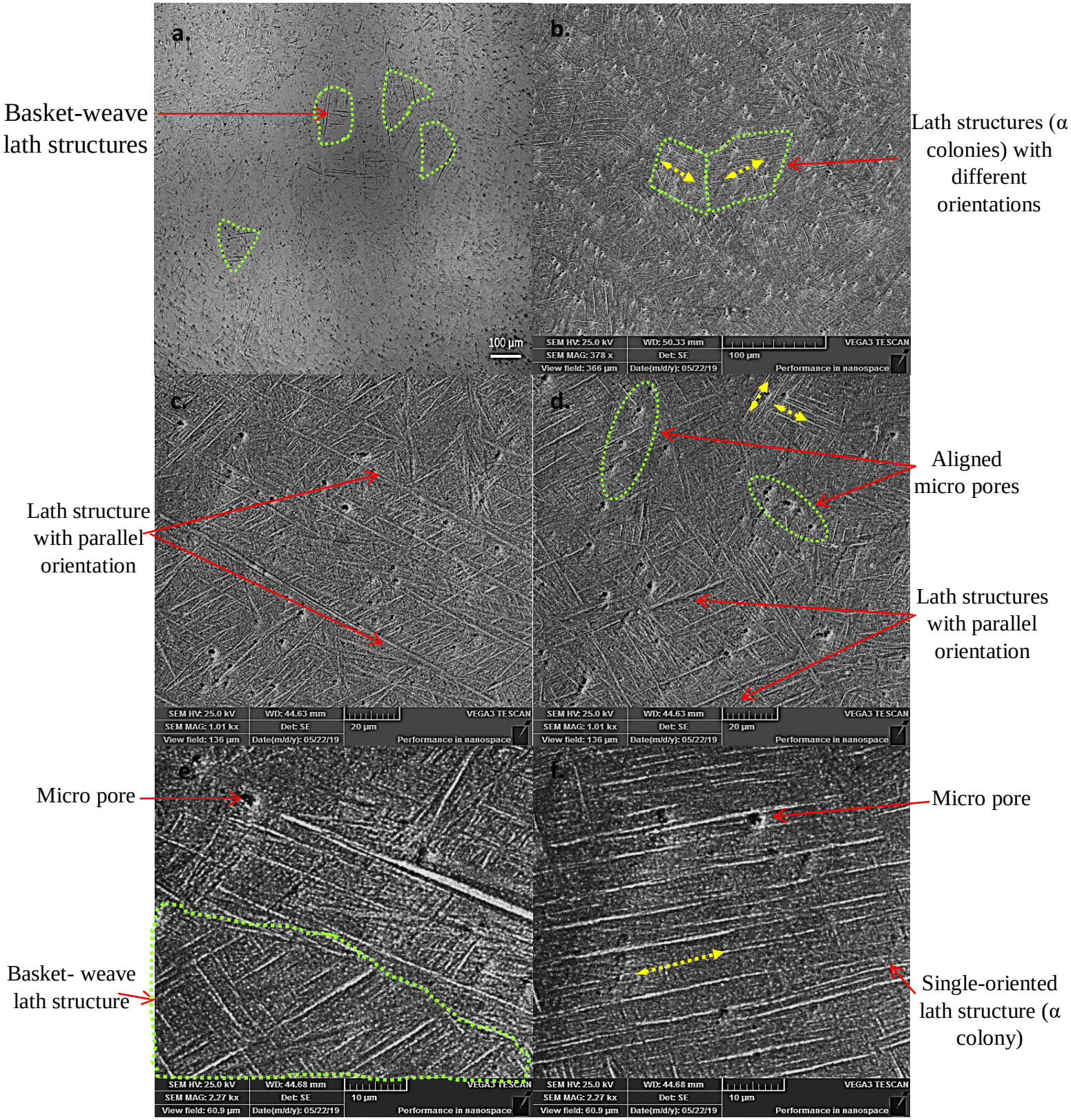

Figure 4.2 Optical and Secondary Electron (SE) micrographs of as-printed Ti6Al4V sample showing a) Basketweave lath structures b-c) α lath structures with different orientations d-f) aligned micro porosities with no observed V-shaped structure.

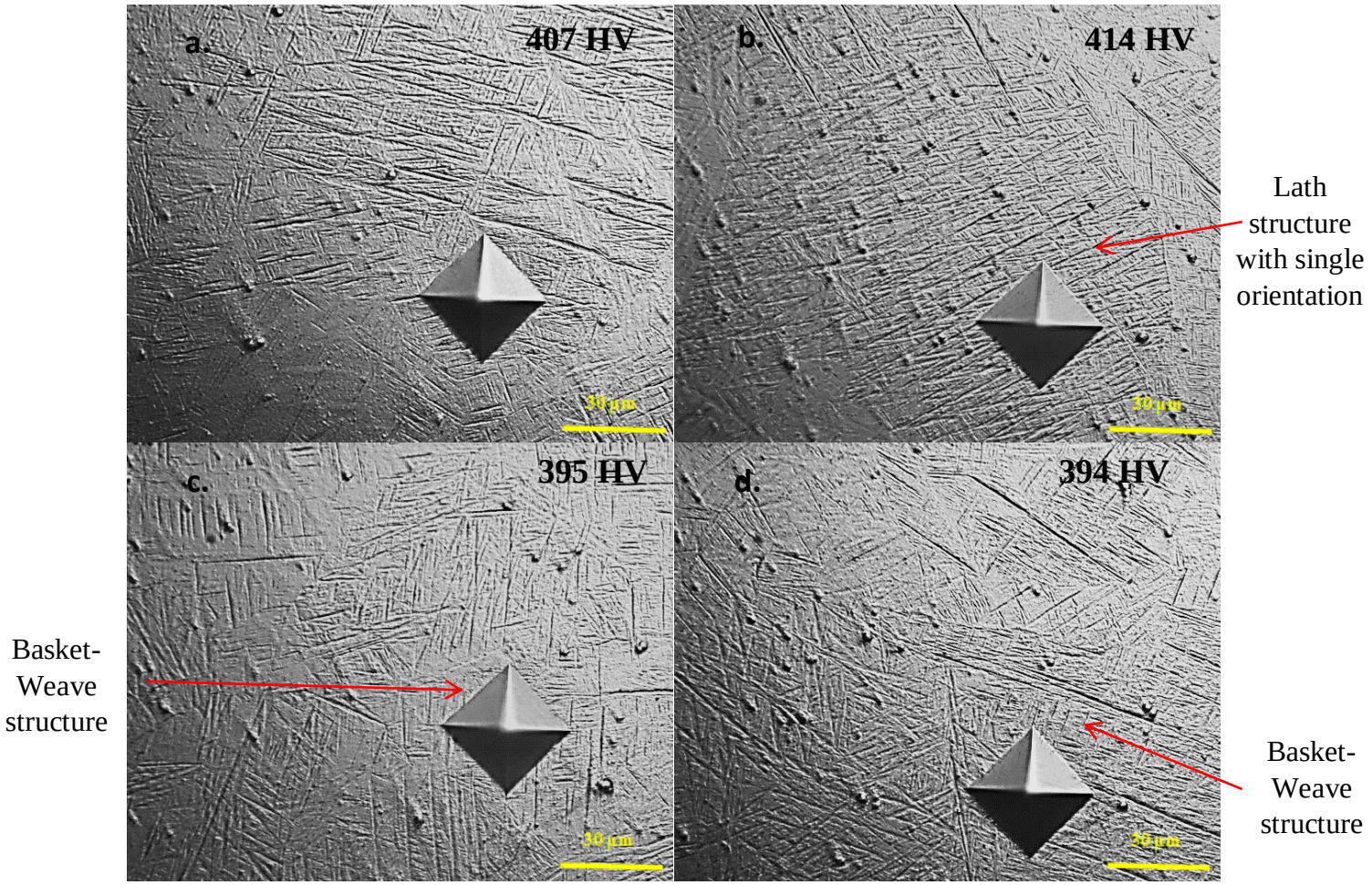

Figure 4.3Hardness indentations on the as-printed Ti6Al4V ELI sample on a-b) lath structures c-d) basketweave lath structure

4.2 Microstructural Evolution of the As-printed and Conventional Ti6Al4V Alloy Solutionized at 1080°C Followed by Water Quenching and Aged at 200°, 500° and 800°.

To study the effect of heat treatment on the microstructural evolution of the as-printed samples, all the samples in this group were heat-treated at 1080℃ for 4 hours and water quenched prior to aging. Generally, cooling and diffusion rate influence the nucleation and growth of the α phase. Usually, water quenching, which has a faster cooling rate than air cooling, transforms β grains to martensitic alpha which can be either a hexagonal structure α' or/and orthorhombic crystal structure α". The amount and type of each martensitic structure is dependent on the chemical composition of the β phase before quenching. Figure 4.4 shows SEM micrographs of 3D printed Ti6Al4V ELI sample which was water quenched after solutionization at 1080℃ for 4 hours, WQ1080-3D. The microstructure comprises mainly of lath structures with different orientations (Fig 4.4(a)) within prior-β grains in addition to few basket weave structures (Fig 4.4 (b)). Lath structures were emanating from prior-β grain boundaries forming α colonies (Widmanstätten colonies) as shown in Fig4.4 (c-d). These α colonies were well developed with distinct boundaries and usually appeared oriented along prior-β grain boundaries. In addition, V-shaped structures were observed within the prior-β grains as shown in Fig 4.4 (c), (f). These V-shaped structures did not appear to have lath structures within them and appeared smooth.

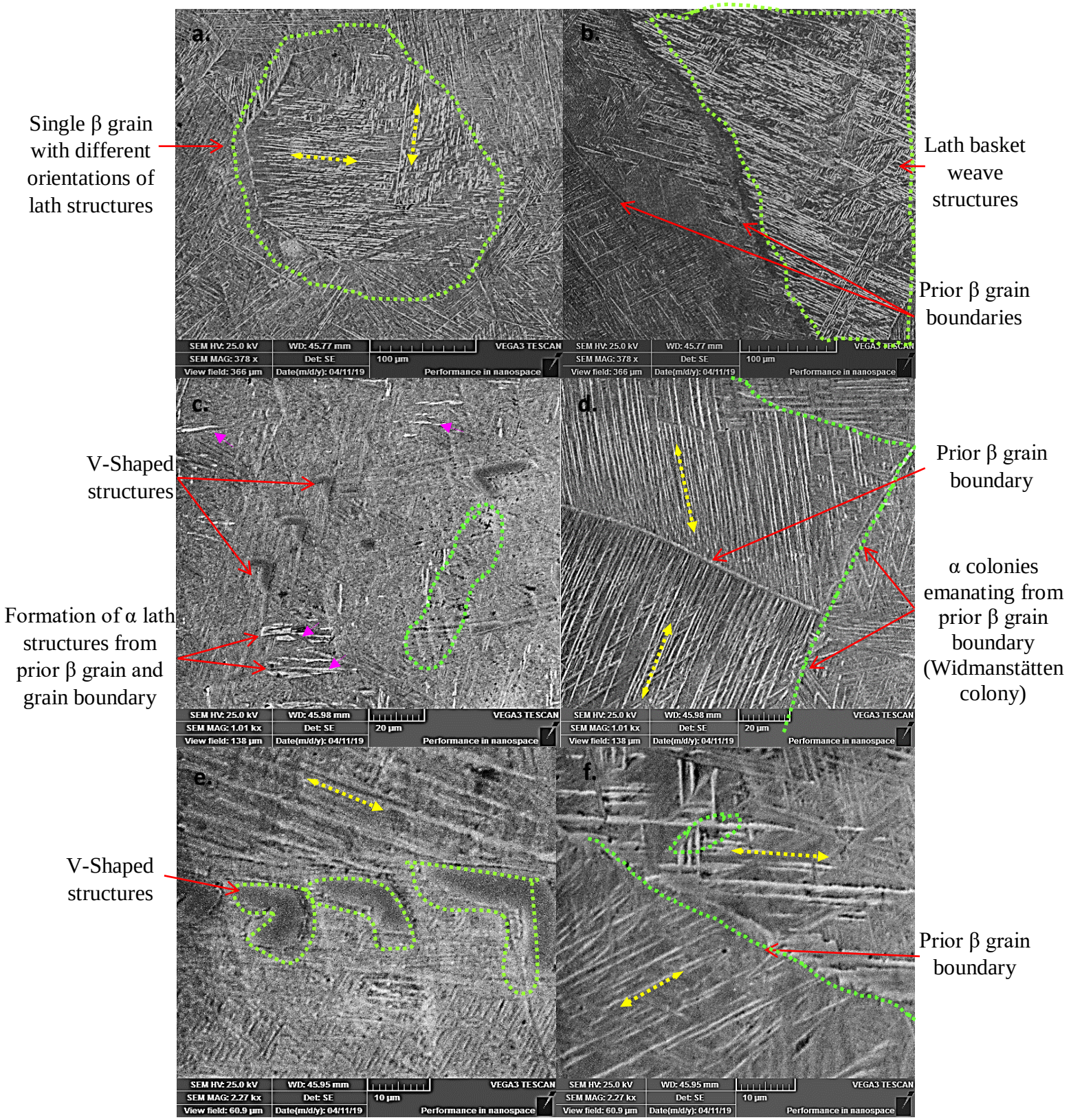

Figure 4.4 SEM micrographs of the WQ1080-3D Ti6Al4V sample showing the α lath, basket weave and evolution of new V-shaped structures

As a baseline for comparison, conventional Ti6Al4V ELI samples were heat-treated at 1080℃ for 4 hours and either air-cooled or water quenched prior to aging. Figure 4.5 shows the optical and Secondary Electron (SEM) micrographs of the conventional Ti6Al4V ELI sample which was water quenched after solutionization at 1080℃ for 4 hours, WQ1080-CV. The microstructure comprised of dense lath structures (Fig 4.5(a)) and single oriented α colonies (Fig 4.5(b)) within prior β grains with few basket weave structures. The volume fraction of V-shaped structures were relatively higher than was observed in the heat-treated 3D printed sample. The V-shaped structures were very much distinct and appeared flat and smooth (Fig 4.5 (c-f)) compared to the ones observed in the heat-treated 3D printed sample. In addition, the observed α colonies were dense and well developed compared to the ones observed in the heat-treated 3D printed sample.

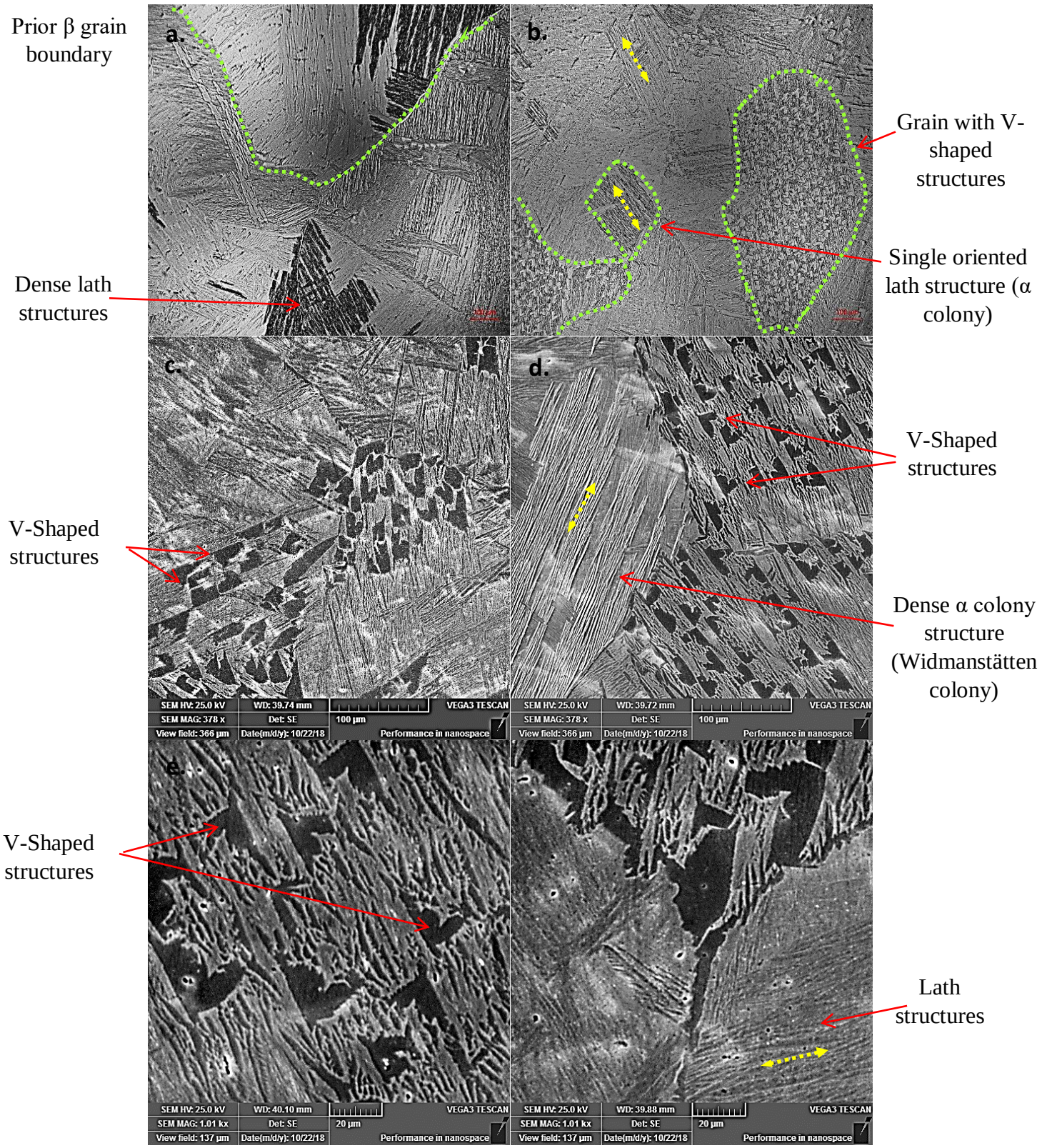

Figure 4.5 Optical and Secondary Electron (SEM) micrographs of the WQ1080-CV Ti6Al4V sample showing dense lath structures along prior β grain boundaries and V-shaped structures in the background

Figure 4.6 shows the microhardness indentations on the different lath and V-shaped structures observed in the heat-treated 3D printed, WQ1080-3D, and conventional, WQ1080-CV, Ti6Al4V ELI alloys. The average measured bulk sample's hardness of the WQ1080-3D was 391 HV while the WQ1080-CV was 447 HV, representing a 14% increase in hardness. As shown in Figure 4.6, the lath structures in the WQ1080-CV were generally denser with a higher hardness than the lath structures observed in the WQ1080-3D. In addition, the observed V-shaped structures in the WQ1080-CV were usually harder than the lath structures observed in the WQ1080-3D. The WQ1080-CV sample, with its densely packed lath structures, exhibited the highest hardness among all the water quenched samples.

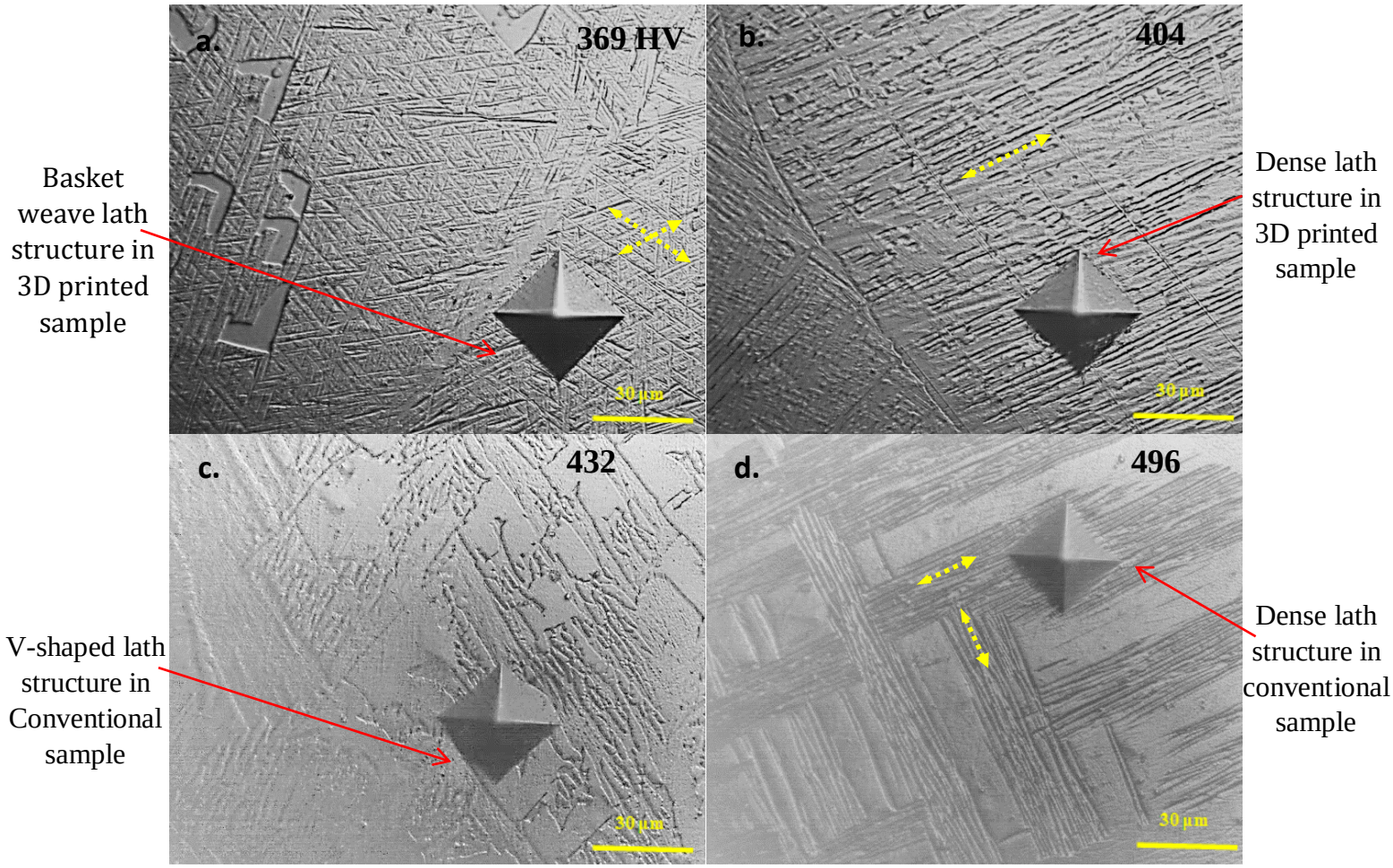

Figure 4.6 Microhardness indentations on the different structures observed in the WQ1080-3D and WQ1080-CV Ti6Al4V samples

After solutionization at 1080°C and water quenching, both the 3D-printed and conventional Ti6Al4V samples were aged at 200°C for 4 hours, from here on referred to as WQ200-3D and WQ200-CV samples respectively. Figure 4.7 shows the observed microstructural features in the WQ200-3D sample. The microstructure was made up of α lath structures within prior β grain and α lath colonies aligned along prior β grain boundaries (Fig 4.7 (a), (b)). Relatively dense lath structures were observed in addition to basketweave lath structures as shown in Figure 4.7. Generally, the basketweave lath structures were within the prior β grains while the lath structures with single orientations were along the prior β grain boundaries. Also, there were relatively more prominent V-shaped structures in this sample when compared with the WQ1080-3D. Figure 4.8 shows the optical and Secondary Electron (SEM) micrographs of the conventional Ti6Al4V sample, WQ200-CV, which had relatively well-developed lengthy lath structures, α colonies emanating from prior β grain boundaries and basketweave structures when compared to the WQ200-3D sample. However, there were no V-shaped structures observed in this sample even though they were present in the "parent" material after solutionization at 1080°C followed by water quenching. Thus, V-shaped structures disappeared from the WQ200-CV sample even though they were present in the WQ1080-CV sample as shown in Figure 4.8.

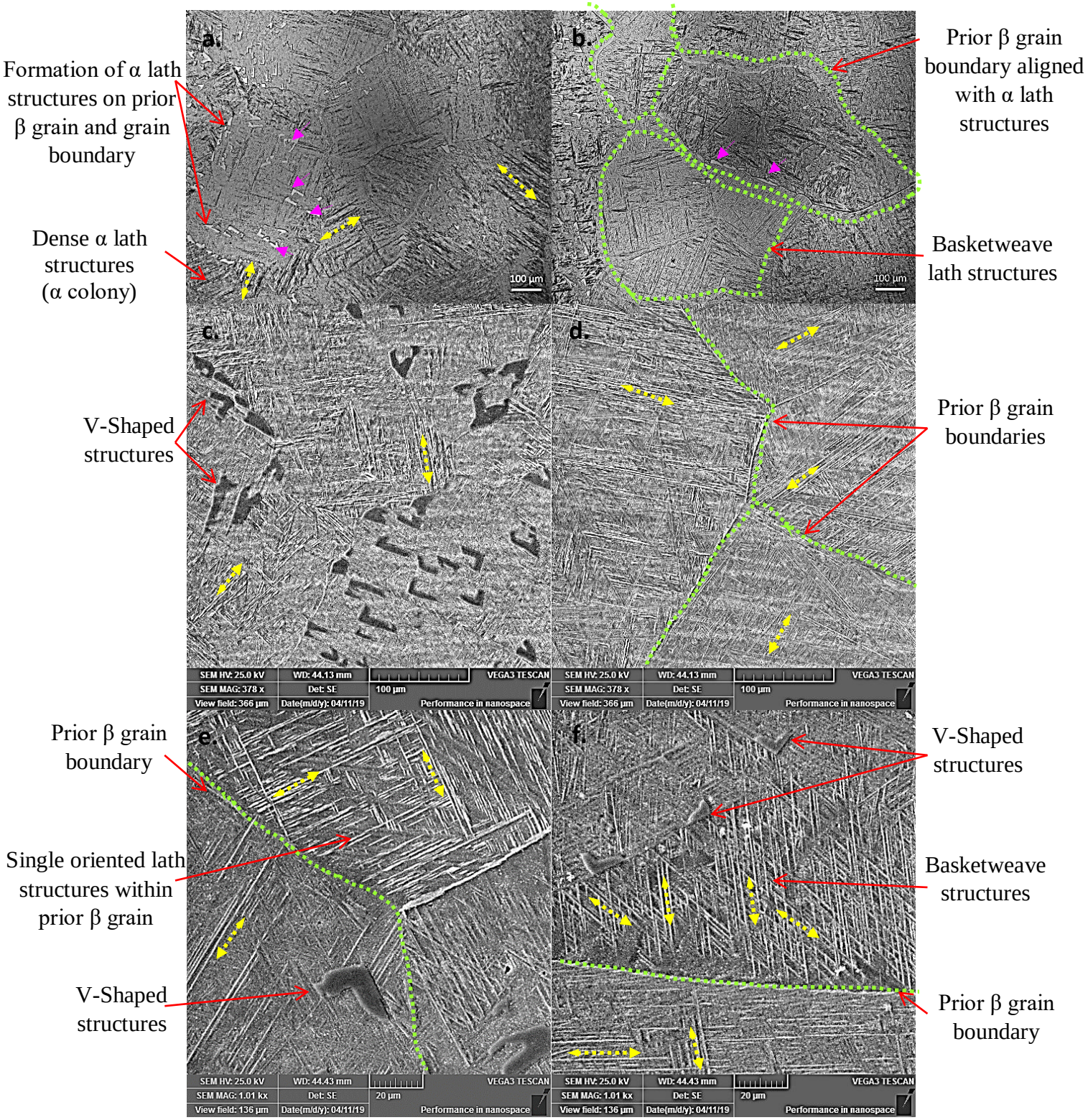

Figure 4.7 Optical and Secondary Electron (SEM) micrographs of the WQ200-3D Ti6Al4V sample showing single oriented lath structures within and along prior β grain boundaries, basket weave lath structures and V-shaped structures

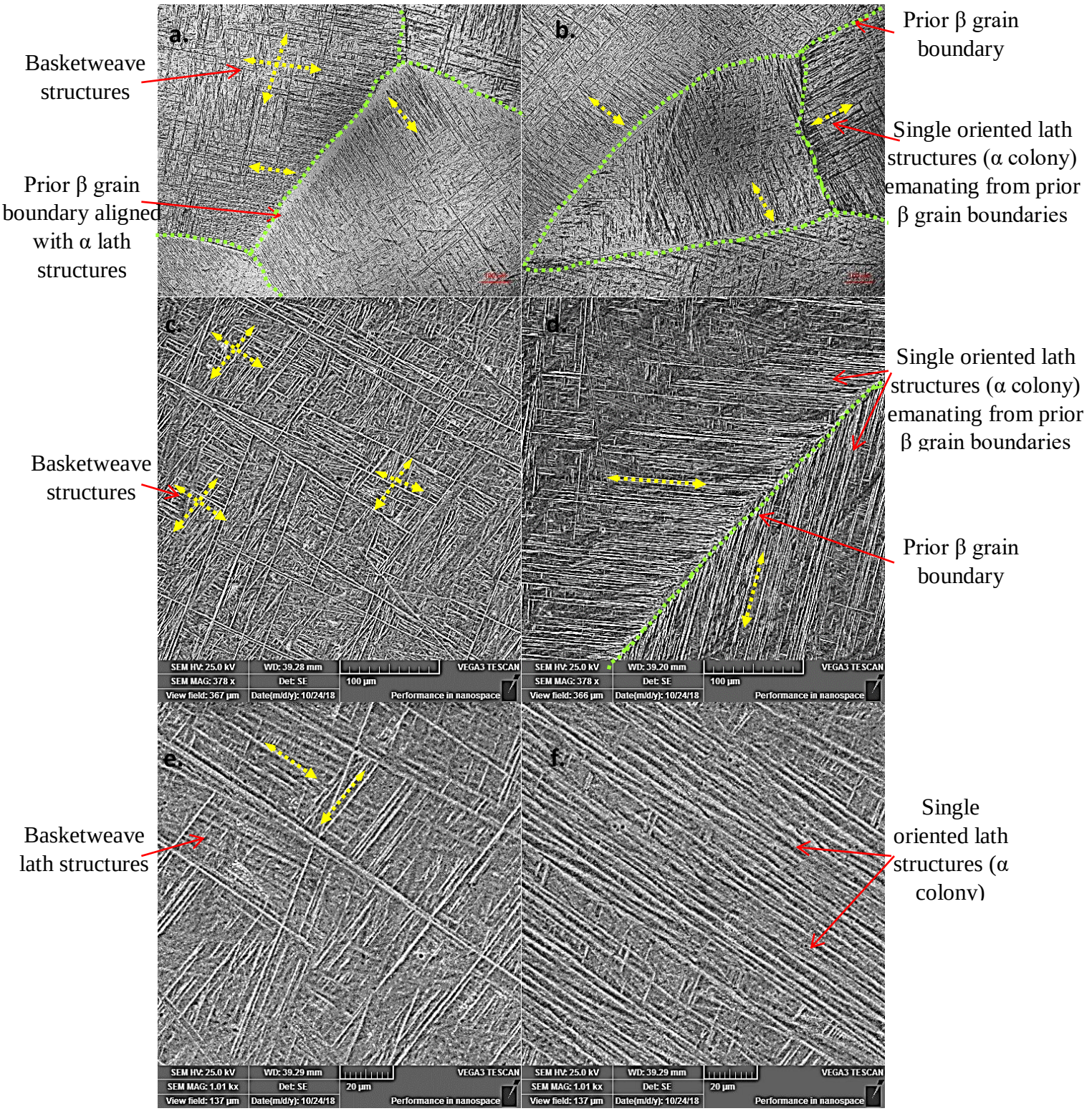

Figure 4.8 Optical and Secondary Electron (SEM) micrographs of the WQ200-CV Ti6Al4V sample showing lath structures and basket weave structures including single α lath structures emanating from prior beta grain boundaries

Figure 4.9 shows the microhardness indentations on the different structures observed in the heat-treated 3D printed, WQ200-3D, and conventional WQ200-CV Ti6Al4V ELI alloys. The average measured bulk sample's hardness of the WQ200-3D was 394 HV while the WQ200-CV sample was 331 HV, representing over 15% difference in hardness. In addition, the WQ200-3D has less than a 1% increase in hardness when compared with the WQ1080-3D sample while the WQ200-CV sample had more than 25% reduction in hardness when compared with the WQ1080-CV sample. This decrease in hardness is associated with the absence of the V-shaped structures in the WQ200-CV sample as shown in Figure 4.9. Irrespective of the processing technique used (either 3D printing or conventional processing), all the observed structural features in the WQ200-3D were relatively harder than the WQ200-CV sample as shown in Figure 4.9. This includes the dense lath structures, the basketweave and α-colonies.

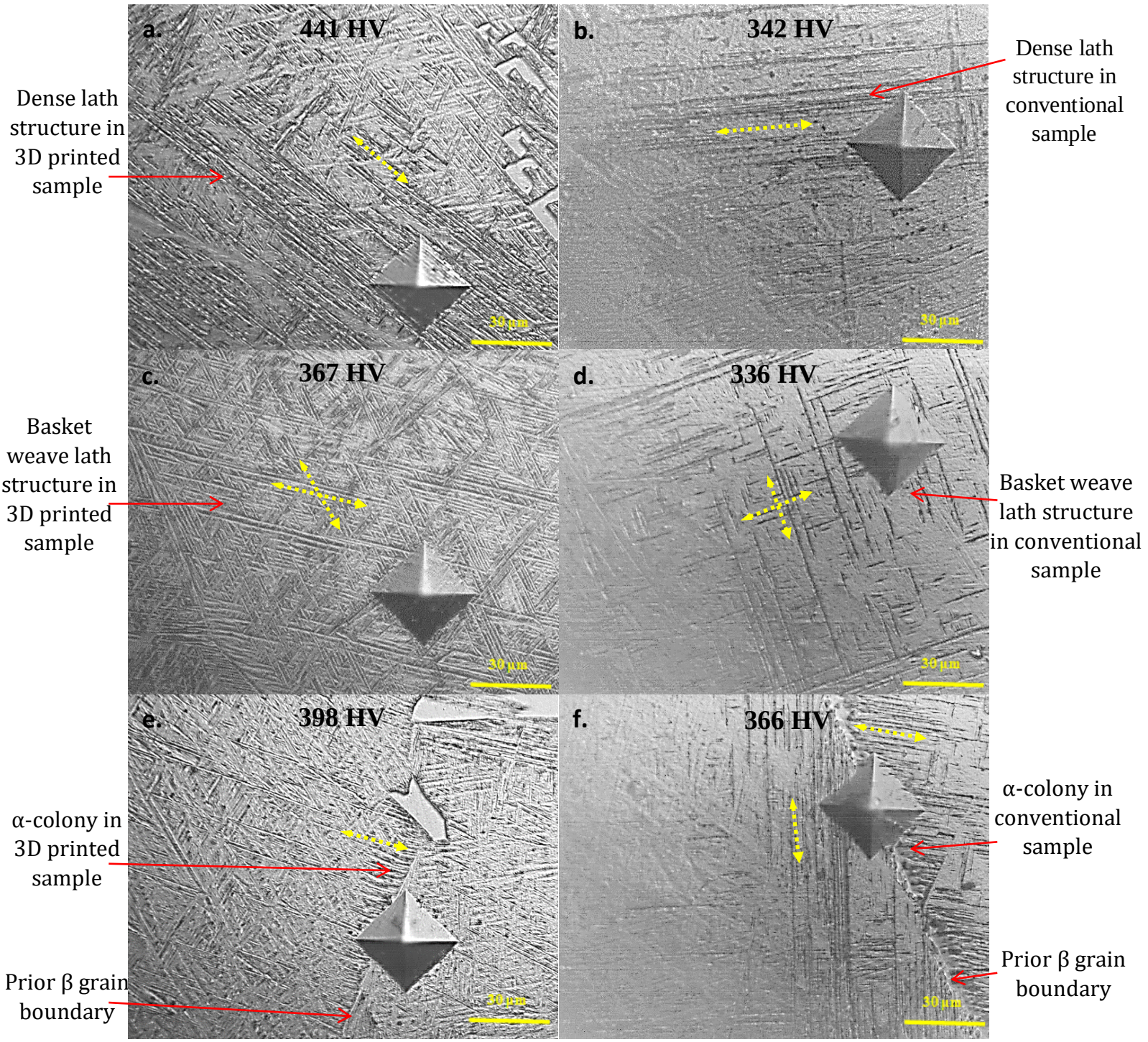

Figure 4.9 Microhardness indentations on the different structures observed in WQ200-3D and WQ200-CV Ti6Al4V samples

Again, after solutionization at 1080°C and water quenching, a group of both the 3D-printed and conventional Ti6Al4V samples were aged at 500°C for 4 hours, from here on referred to as WQ500-3D and WQ500-CV respectively. Figure 4.10 shows the observed microstructural features in the WQ500-3D sample. The sample had prior β grain boundaries aligned with α lath colonies, basketweave lath structures within prior β grains and prominent coarse V-shaped structures. On the other hand, the WQ500-CV sample had well-developed α lath colonies and basketweave lath structures as shown in Figure 4.11. Again, in contrast to the WQ500-3D at the same condition, there were no observed V-shaped structures in the WQ500-CV sample.

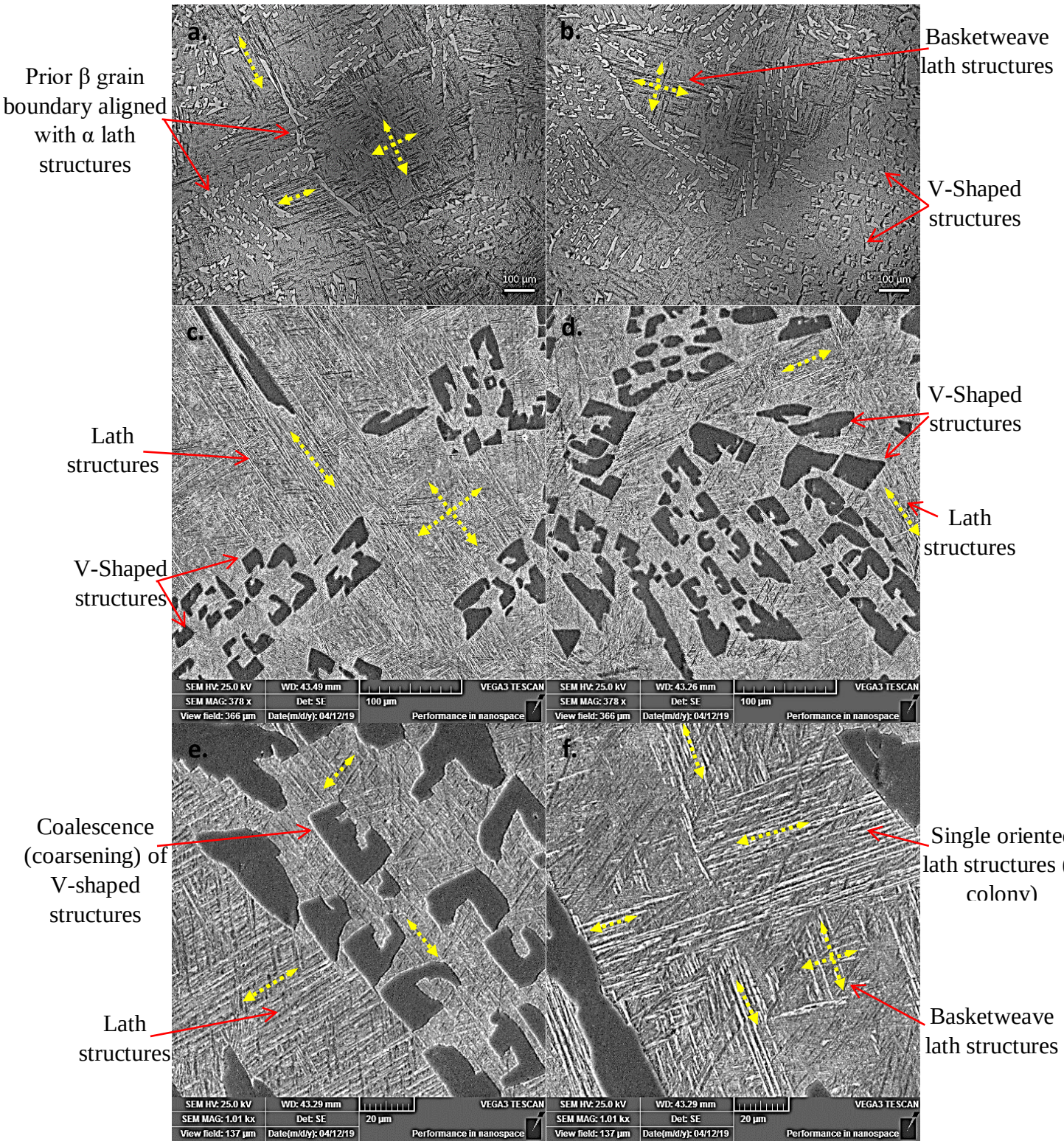

Figure 4.10 Optical and Secondary Electron (SEM) micrographs of the WQ500-3D Ti6Al4V sample showing lath structures/basketweave structures and coalescence (coarsening) of V-shaped structures

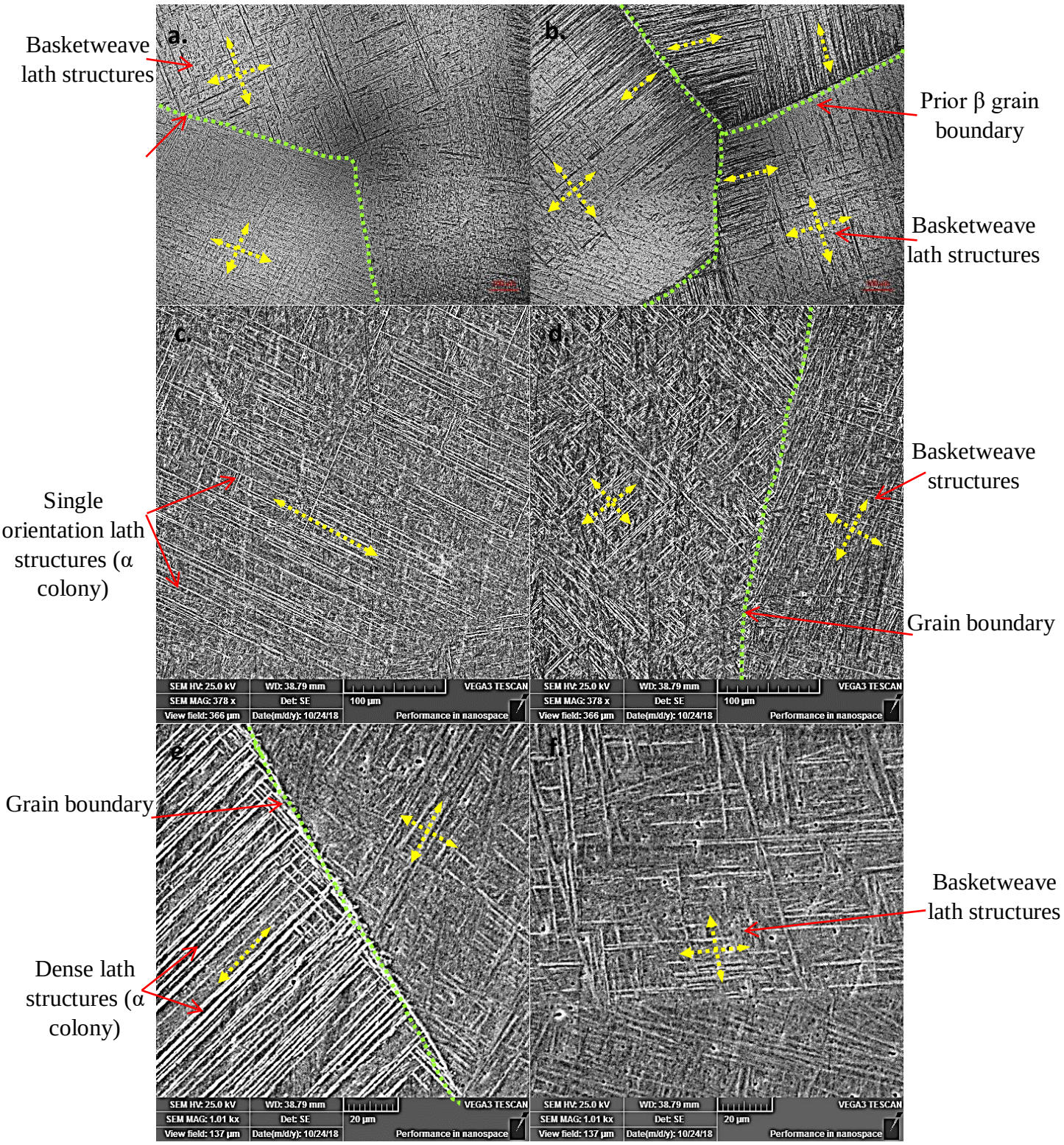

Figure 4.11 Optical and Secondary Electron (SEM) micrographs of the WQ500-CV Ti6Al4V sample showing lath and basket weave structures

Figure 4.12 shows the microhardness indentations on the different structures observed in the heat-treated 3D printed, WQ500-3D, and conventional WQ500-CV Ti6Al4V ELI alloys. The average measured bulk sample's hardness of the WQ500-3D was 447 HV while the WQ500-CV sample was 359 HV, representing over 19% difference in hardness. Also, this represented an over 13% increase in hardness when compared with the WQ200-3D and WQ1080-3D samples. Also, the hardness of the WQ500-3D was over 11% higher than the as-printed Ti6Al4V sample. Again, regardless of the processing technique used (either 3D printing or conventional processing), all the observed structural features in the WQ500-3D were relatively harder than the WQ500-CV sample as shown in Figure 4.12. The larger V-shaped structures exhibited higher hardness when compared with the smaller V-shaped structures as shown in Figure 4.12 (a) and (b).

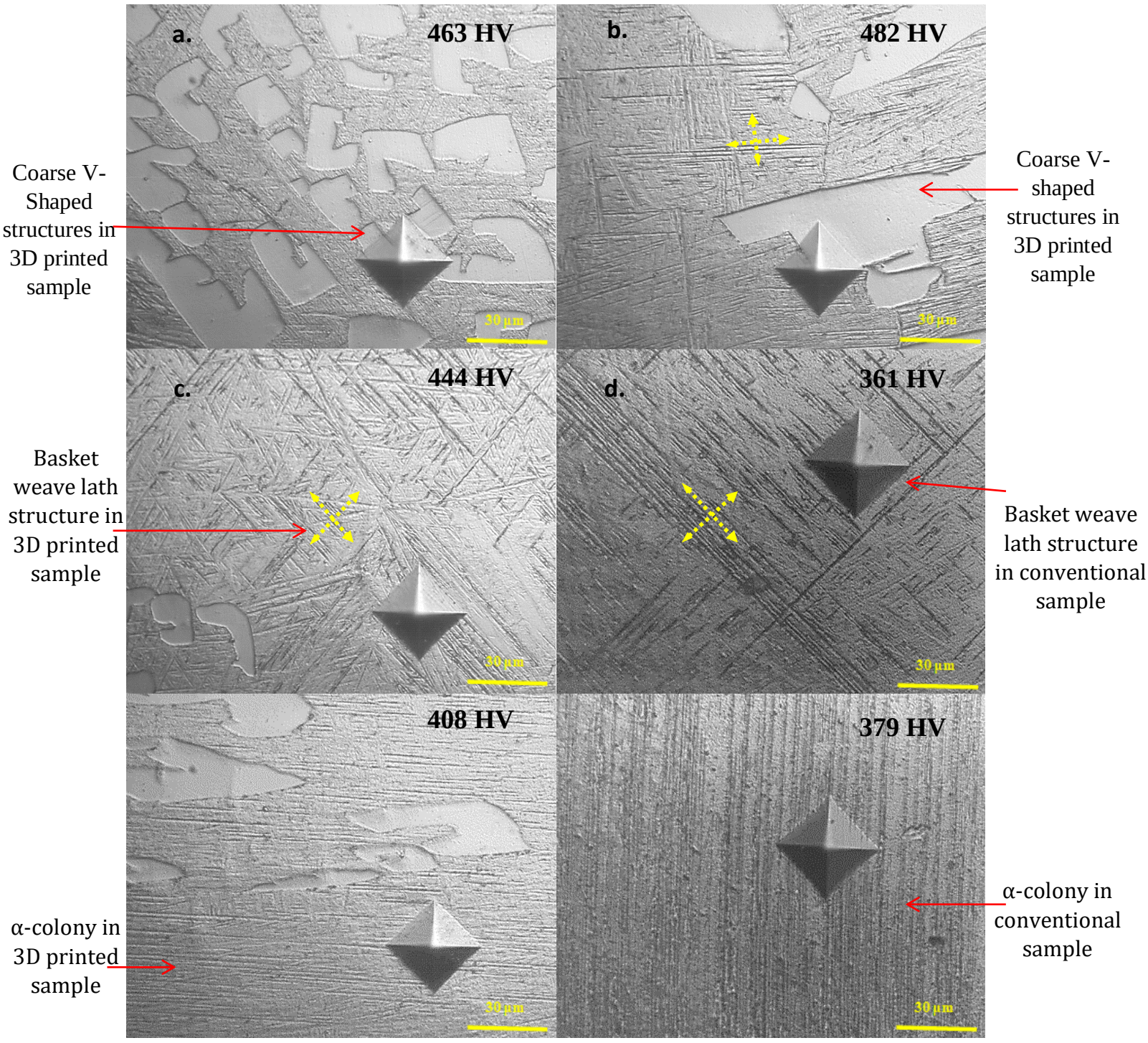

Figure 4.12 Microhardness indentations on the different structures observed in the WQ500-3D and WQ500-CV Ti6Al4V samples

After solutionization at 1080°C and water quenching, another group of both the 3D-printed and conventional Ti6Al4V samples were aged at 800°C for 4 hours, from here on referred to as WQ800-3D and WQ800-CV respectively. Figure 4.13 shows the observed microstructural features in the WQ800-3D sample showing relatively few non-distinct V-shaped structures when compared with the previous heat-treated 3D printed samples. The observed lath and basketweave structures in the WQ800-3D sample were relatively coarser and not well developed as shown in Figure 4.13. There was a new structure observed which appeared globular within the sample. The structure of the WQ800-CV sample also had relatively coarser lath structures with observed globules as shown in Figure 4.14. Again, there were no observed V-shaped structures in the WQ800-CV sample.

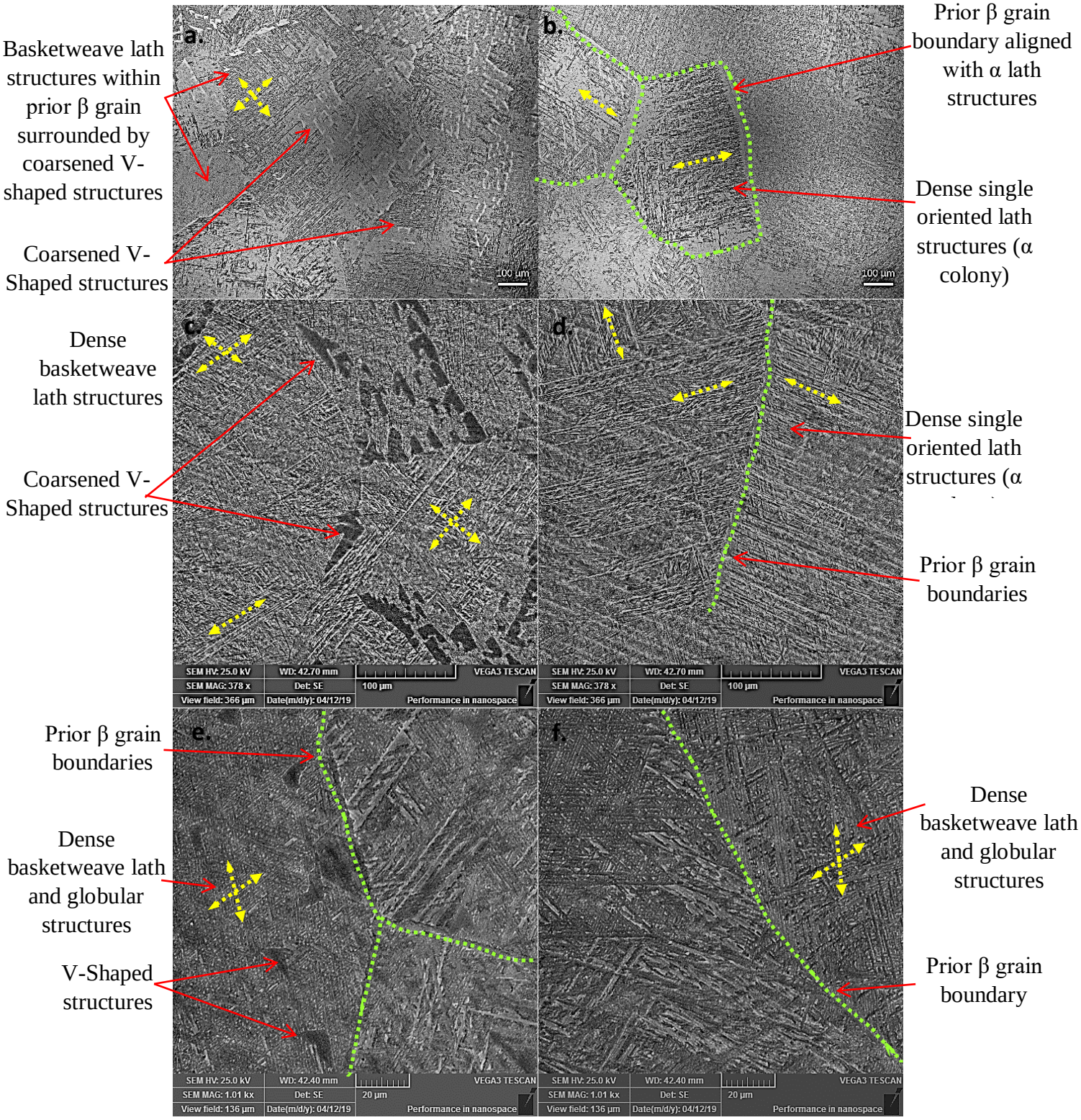

Figure 4.13 Optical and Secondary Electron (SEM) micrographs of the WQ800-3D Ti6Al4V sample showing dense lath structures/basketweave lath structures and coarsened non-distinct V-shaped and globular structures

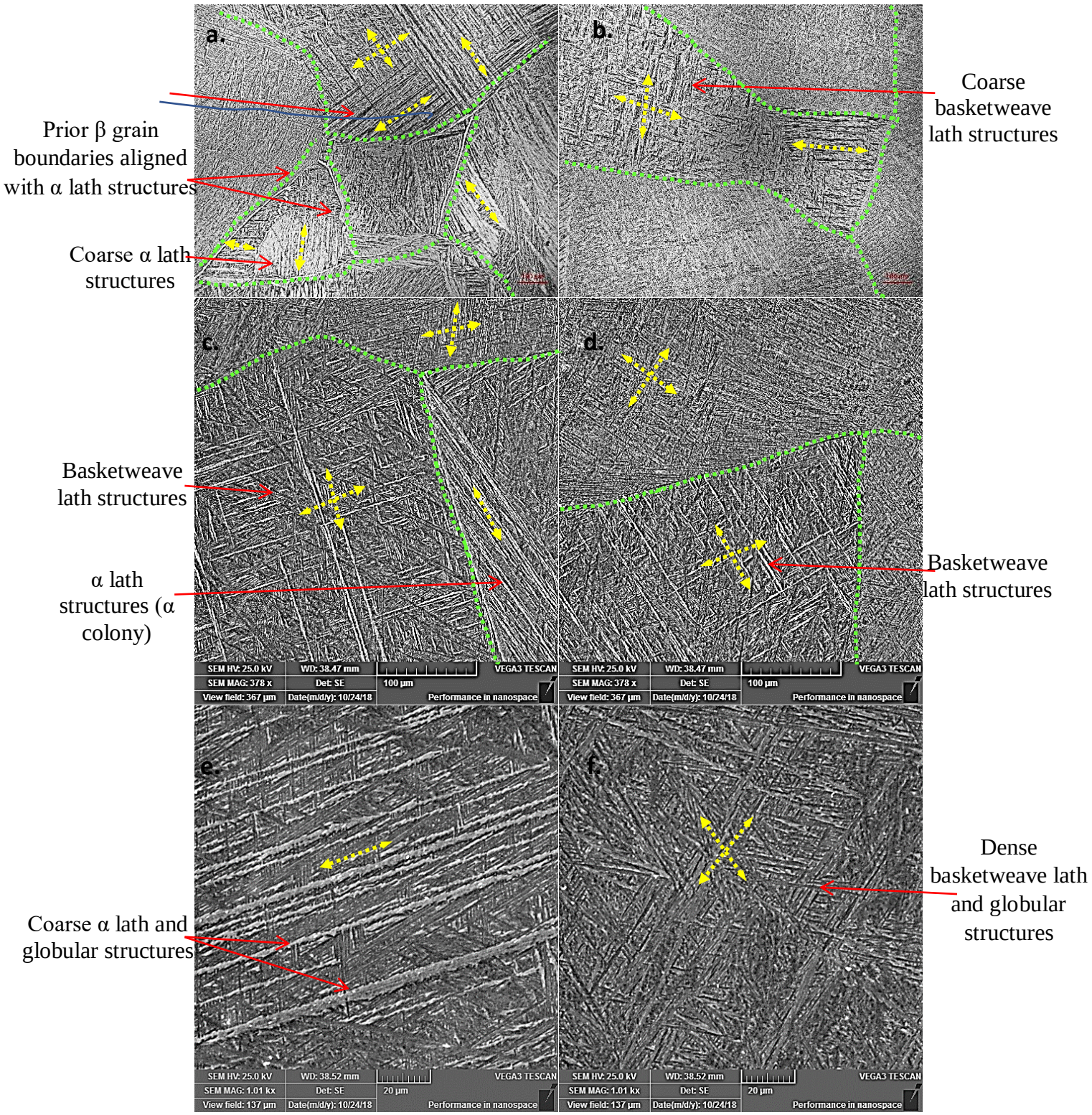

Figure 4.14 Optical and Secondary Electron (SEM) micrographs of the WQ800-CV Ti6Al4V sample showing prior β grain boundaries aligned with coarse α lath structures, coarse α lath/basketweave lath, and globular structures

The microhardness indentations on the different structures observed in the heat-treated 3D printed, W800-3D, and conventional WQ800-CV Ti6Al4V ELI alloys are shown in Figure 4.15. The average measured bulk sample's hardness of the WQ800-3D was 423 HV while the WQ800-CV sample was 347 HV, representing over 17% difference in hardness. Again, this represented a 5% higher hardness when the as-printed sample is compared with the WQ800-3D sample and a 5% reduction in hardness when the WQ800-3D is compared with the WQ500-3D which had the highest hardness in this group. As shown in Figure 4.15, all the different microstructural features in the WQ800-3D sample had relatively higher hardness than the WQ800-CV sample.

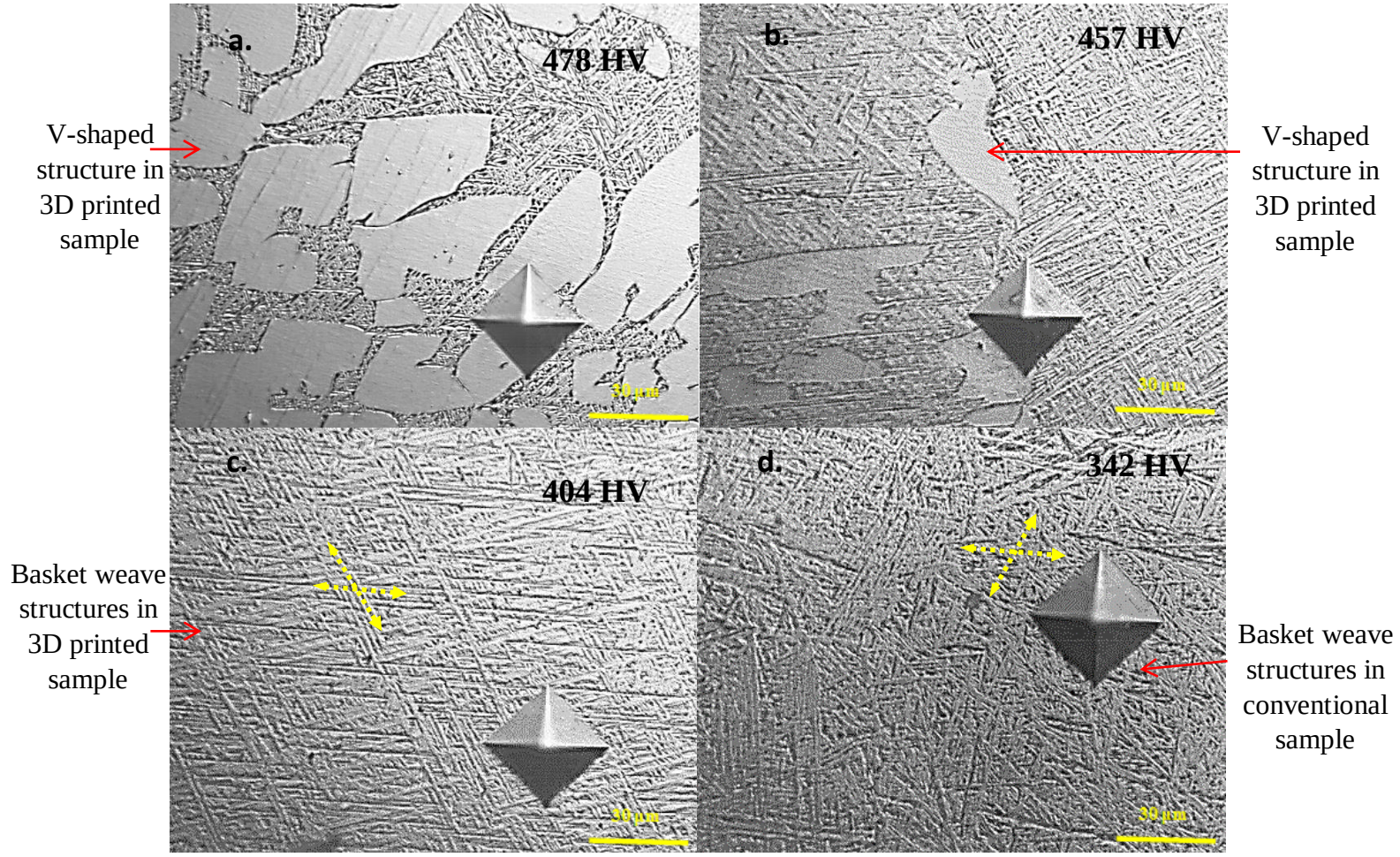

Figure 4.15 Microhardness indentations on the different structures observed in the WQ800-3D and WQ800-CV Ti6Al4V samples

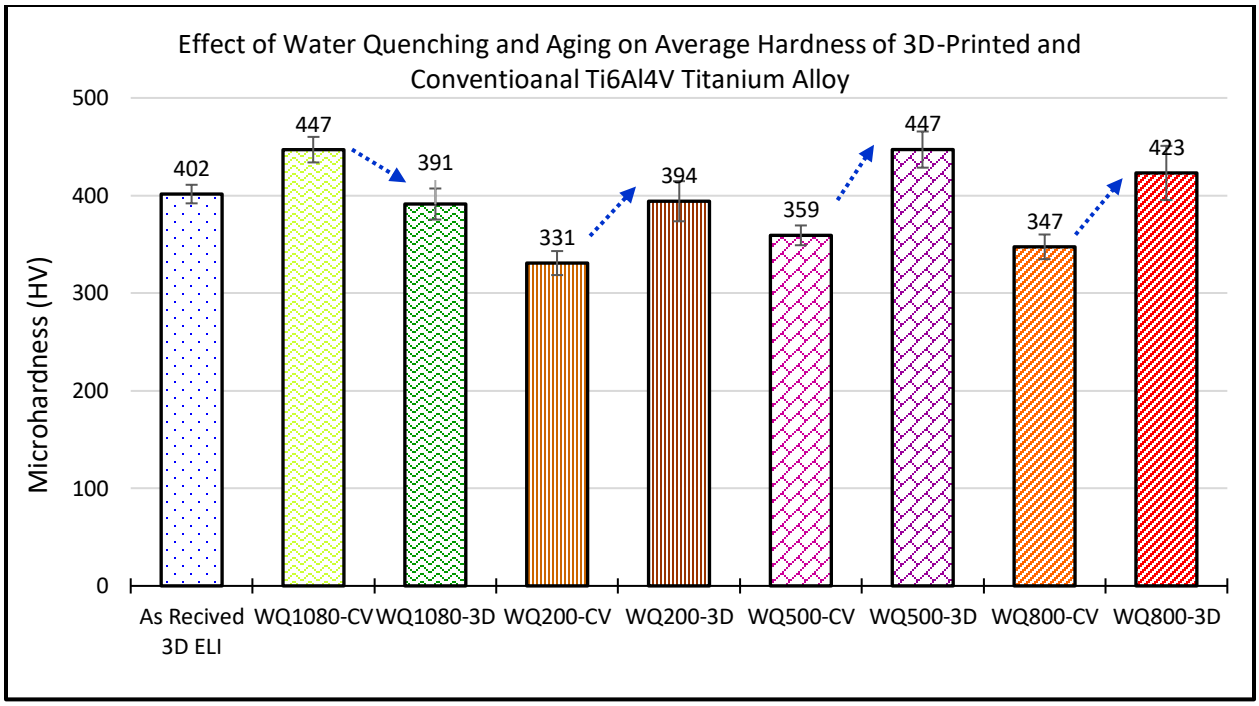

Figure 4.16 Effect of Water-quenching and aging on the average microhardness of 3D-printed and conventional Ti6Al4V titanium alloy

Figure 4.16 shows the effect of water-quenching and aging on the average microhardness of 3D-printed and conventional Ti6Al4V titanium alloy. The 3D printed samples had higher average hardness values compared to the conventionally manufactured titanium alloys. The WQ-1080-3D, WQ500-3D, and WQ800-3D had an average hardness of over 400 HV when compared to all the water-quenched samples.

4.3 Microstructural Evolution of the As-printed and Conventional Ti6Al4V Alloy Solutionized at 1080°C Followed by Air Cooling and Aged at 200°, 500°, and 800°.

To study the effect of heat treatment on the microstructural evolution of the as-printed and conventional samples, all the samples in this group were heat-treated at 1080℃ for 4 hours and air-cooled prior to aging. The 3D printed and conventional samples that were solutionized at 1080℃ for 4 hours and air-cooled are from here on referred to as AC1080-3D and AC1080-CV samples respectively. Figure 4.17 shows the observed microstructural features in the AC1080-3D sample. The microstructure was made up of few V-shaped structures, α lath structures with a high degree of orientation within prior β grain and α lath colonies aligned along prior β grain boundaries. The α lath colonies aligned along prior β grain boundaries were highly dense and well-developed when compared with the lath structures within the grains as shown in Figure 4.17 (c) and (e).

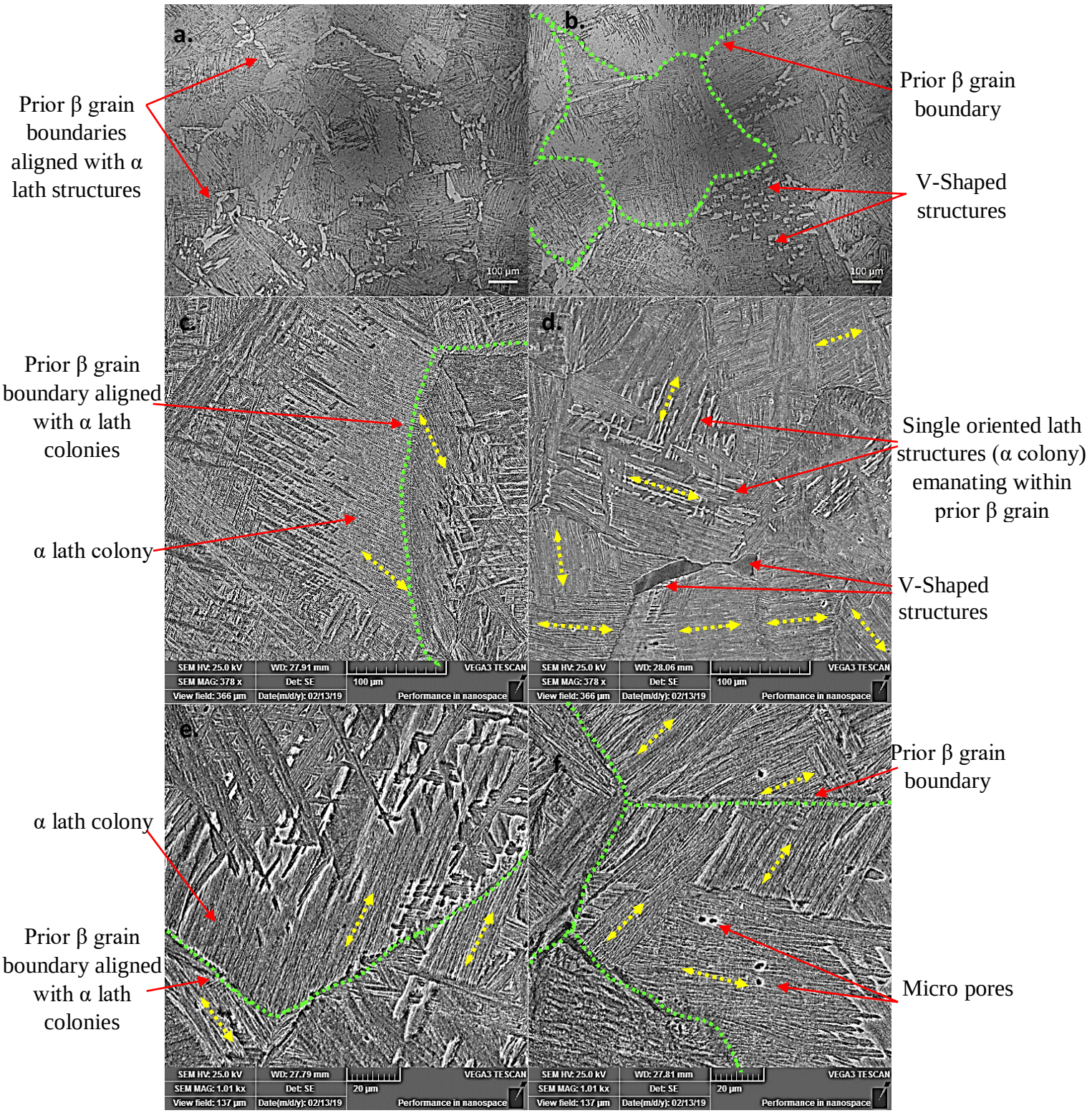

Figure 4.17 Optical and Secondary Electron (SEM) micrographs of the AC1080-3D Ti6Al4V sample showing prior β grain boundaries aligned with α lath structures, α lath colonies (Widmanstätten colonies) and V-shaped structures

Generally, the AC1080 sample had prior β grains and grain boundaries and precipitated needle-like α-lath structures with single and 90° lath orientations as shown in Figure 4.18. The needle-like α-lath structures precipitated out of the prior β grains and grain boundaries at room temperature in some regions of the material. Other regions of the sample did not have precipitated α-lath structures. The observed precipitated α-lath structures were relatively fine (needle-like) with distinct single orientations forming packets of lath structures. In addition, there were α-lath structures with nucleating 90° lath orientations to each other as shown in Figure 4.18 (b) to (d). In addition, tiny and fine α-lath structures were observed precipitating from prior β grain boundaries and grains as shown in Figure 4.18 (e) to (f). This demonstrates the metastable nature of the β grains at room temperature. Even though the prior β grains appeared as basket-weave lath structures with 90° lath orientations to each other, they were not prominent and appeared as flat background layers as shown in Figure 4.18 (f). There were no V-shaped structures within the AC1080-CV sample.

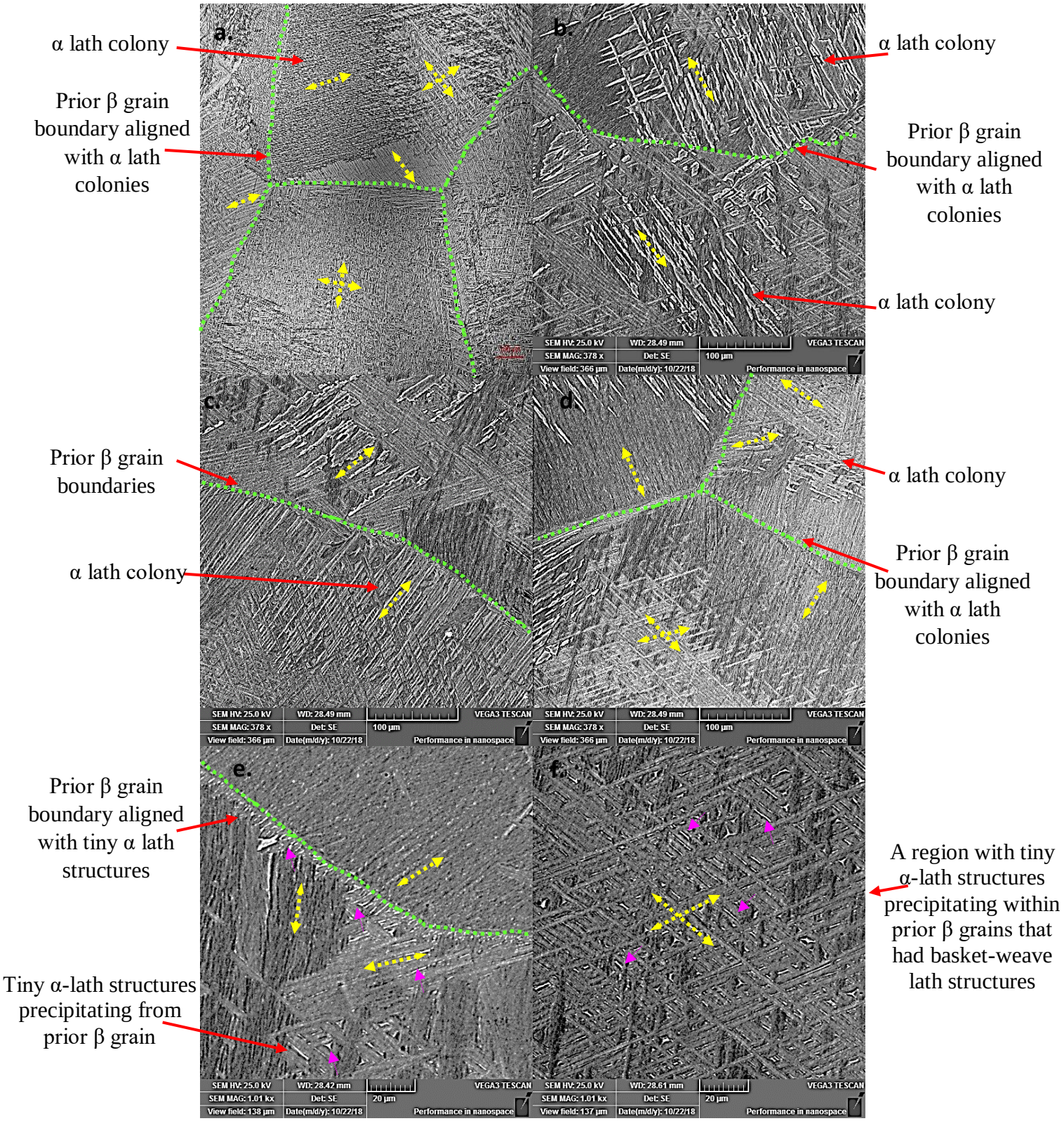

Figure 4.18 Optical and Scanning Electron Microscope (SEM) micrographs of the AC1080-CV showing prior β grain boundaries aligned with α lath structures and α lath colonies (Widmanstätten colonies)

The average measured bulk sample's hardness of the AC1080-3D was 396 HV while the AC1080-CV sample was 376 HV, representing over 5% difference in hardness. The bulk hardness of the AC1080-3D was approximately 1.5% lower than the as-printed sample. The microhardness indentations on the different structures observed in the AC1080-3D and AC1080-CV samples are shown in Figure 4.19. Generally, the different microstructural features, dense α lath, and basketweave lath structures were relatively harder in the AC1080-3D compared with the AC1080-CV. The precipitated lath structures close to the prior β grain boundaries were harder than the basketweave structures close to the grain boundary. Also, the precipitated lath structures close to the prior β grain boundaries were harder than the lath structures away from the prior β grain boundaries.

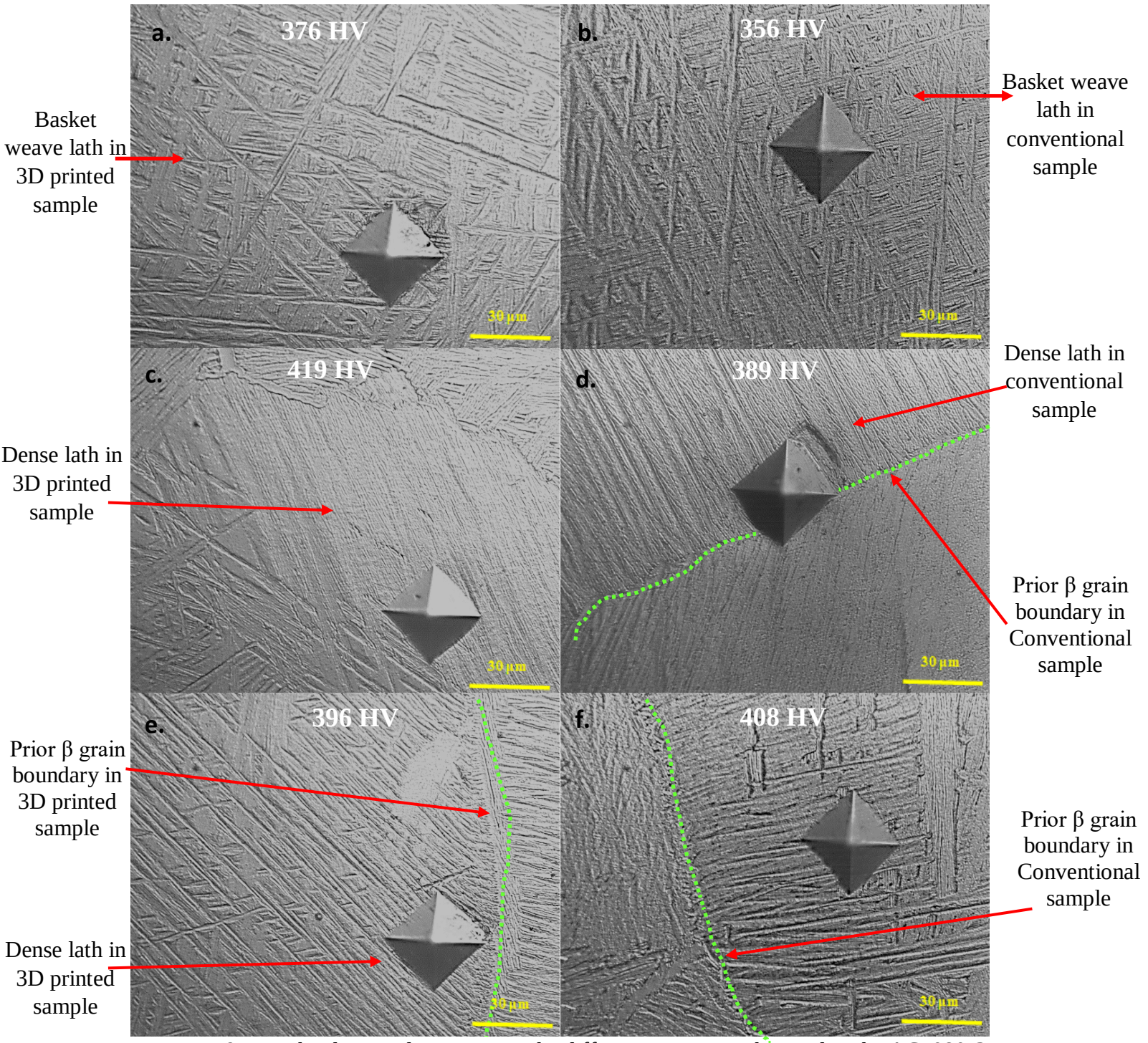

Figure 4.19 Microhardness indentations on the different structures observed in the AC1080-3D and AC1080-CV Ti6Al4V samples

After solutionization at 1080°C and air cooling, both the 3D-printed and conventional Ti6Al4V samples were aged at 200°C for 4 hours, from here on referred to as AC200-3D and AC200-CV samples respectively. Figure 4.20 shows the observed microstructural features in the AC200-3D sample. The microstructure was made up of prominent V-shaped structures, regions with tiny α-lath structures precipitating within prior β grains, single oriented lath structures (α colony) emanating from prior β grain and α lath structures within prior β grains. There was a high area fraction of coarsened V-shaped structures within prior β grains as shown in Figure 4.20 (c), (d) and (f). Generally, the AC200-CV sample had a high-volume fraction of distinct but relatively coarse α-lath structures, and prior β grain and grain boundaries. Some of the relatively coarse α-lath structures did not have well-defined lath orientations when compared to the AC1080-CV sample. Also, the relatively coarse α-lath structures were relatively shorter and discontinuous compared to the needle-like α-lath structures in the AC1080-CV. Some needle-like α-lath structures were observed close to large coarse α-lath structures as shown in Figure 4.21(d). The prior β grains were not apparent and appeared as flat background layers.

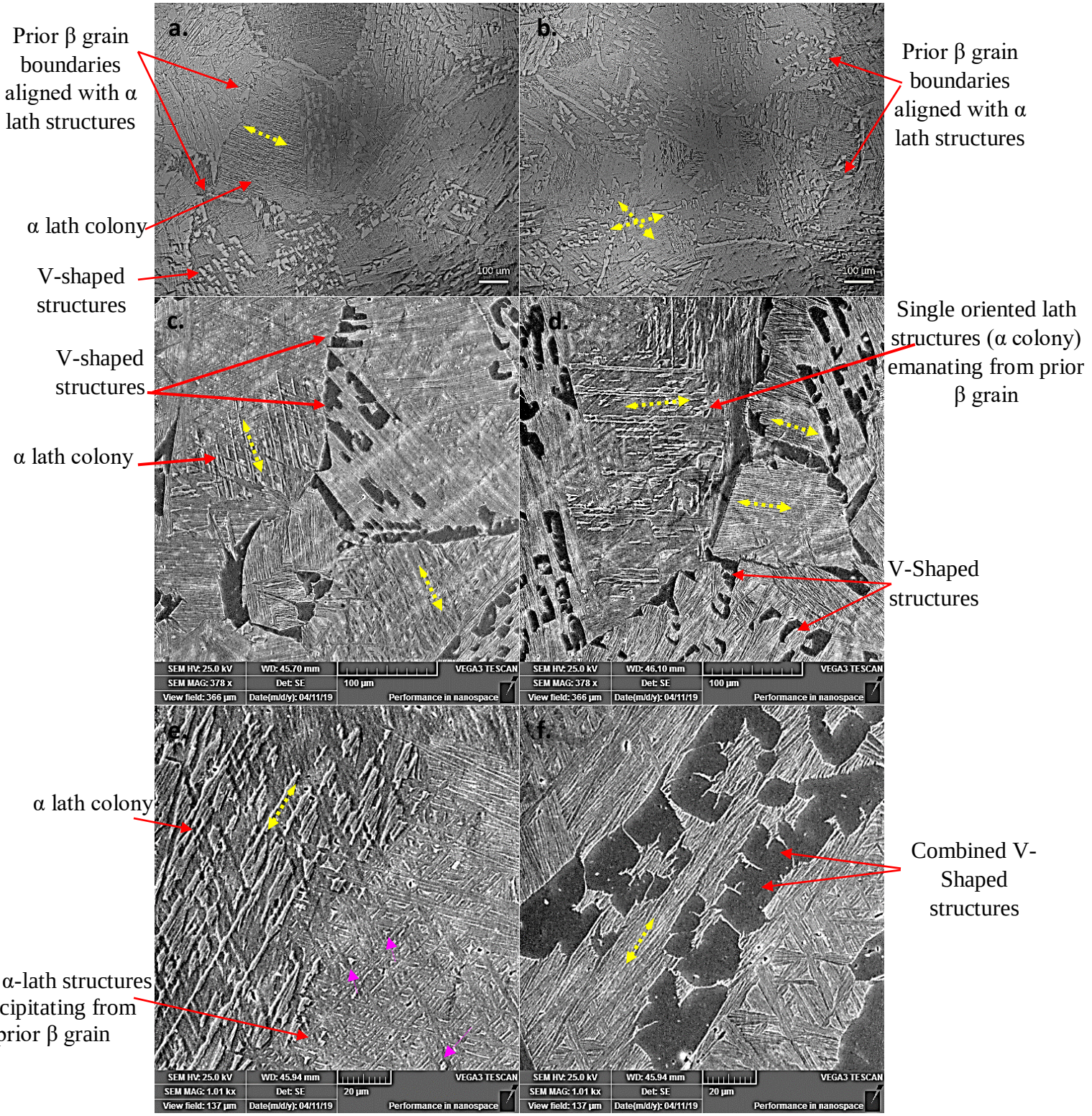

Figure 4.20 Optical and Secondary Electron (SEM) micrographs of the AC200-3D Ti6Al4V sample showing prior β grain boundaries aligned with α lath structures, α lath colonies (Widmanstätten colonies) and coarse V-shaped structures

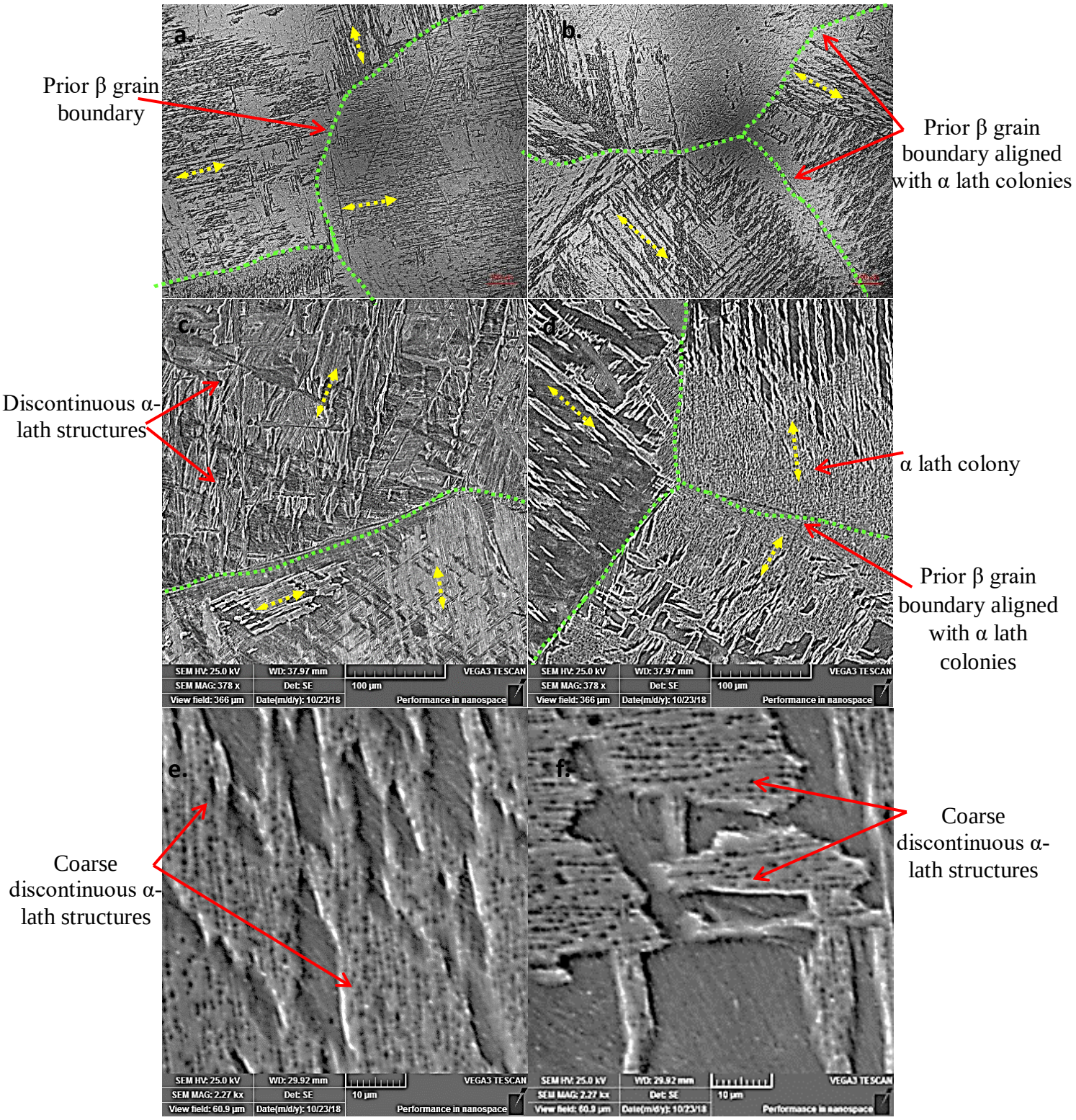

Figure 4.21 Optical and Scanning Electron Microscope (SEM) micrographs of the AC200-CV showing high volumes of distinct but relatively coarse and discontinuous α-lath structures and prior β grain boundaries aligned with α lath structures

The average measured bulk sample's hardness of the AC200-3D was 415 HV while the AC200-CV sample was 324 HV. The bulk hardness of the AC200-3D was approximately 28% higher than the AC200-CV sample and approximately 4% higher than the AC1080-3D sample. Also, the average microhardness of the AC200-CV sample was 14% lower than the AC1080-CV sample. The microhardness indentations on the different structures observed in the AC200-3D and AC200-CV samples are shown in Figure 4.22. Generally, the different microstructural features such as the basketweave lath structures were relatively harder in the AC200-3D compared with the AC200-CV. The distinct but relatively coarse discontinuous α-lath structures have lower hardness when compared to the needle-like, well oriented continuous α-lath structures. As always, the V-shaped structures have higher hardness compared to the lath structures.

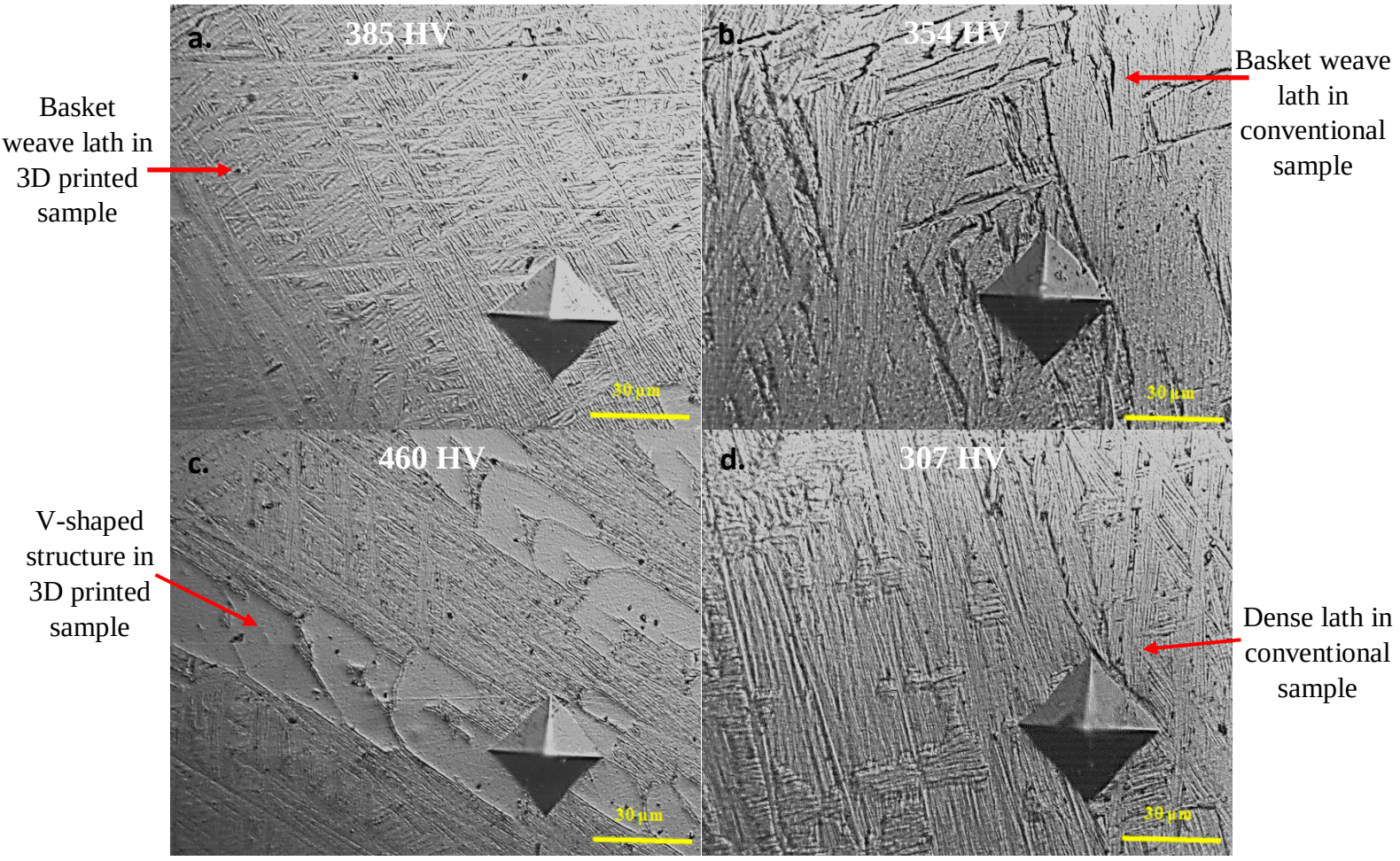

Figure 4.22Micro hardness indentations on the different structures observed in the AC200-3D and AC200-CV Ti6Al4V samples

After solutionization at 1080°C and air cooling, another group of both the 3D-printed and conventional Ti6Al4V samples were aged at 500°C for 4 hours, from here on referred to as AC500-3D and AC500-CV samples respectively. Figure 4.23 shows a high-volume fraction of coarse V-shaped structures and α lath colonies (Widmanstätten colonies) observed in the AC500-3D sample. The α lath and basketweave lath structures appeared discontinuous but highly oriented. Also, some of the coarse V-shaped structures were highly oriented along grain boundaries. Some V-shaped structures were observed coalescing within the prior β grains as shown in Figure 4.23 (e) and (f). On the other hand, the AC500-CV sample had prior β grains and grain boundaries and precipitated needle-like α-lath structures with no observed V-shaped structures as shown in Figure 4.24. The distinct α-lath structures were relatively fine (needle-like) compared with the AC500-3D sample. In addition, α-lath structures were discontinuous with well-defined lath orientations in some regions as shown in Figure 4.24. In addition, small volume fractions of tiny spheroidized α structures were observed within the specimens as shown in Figure 4.24 (e) and (f).

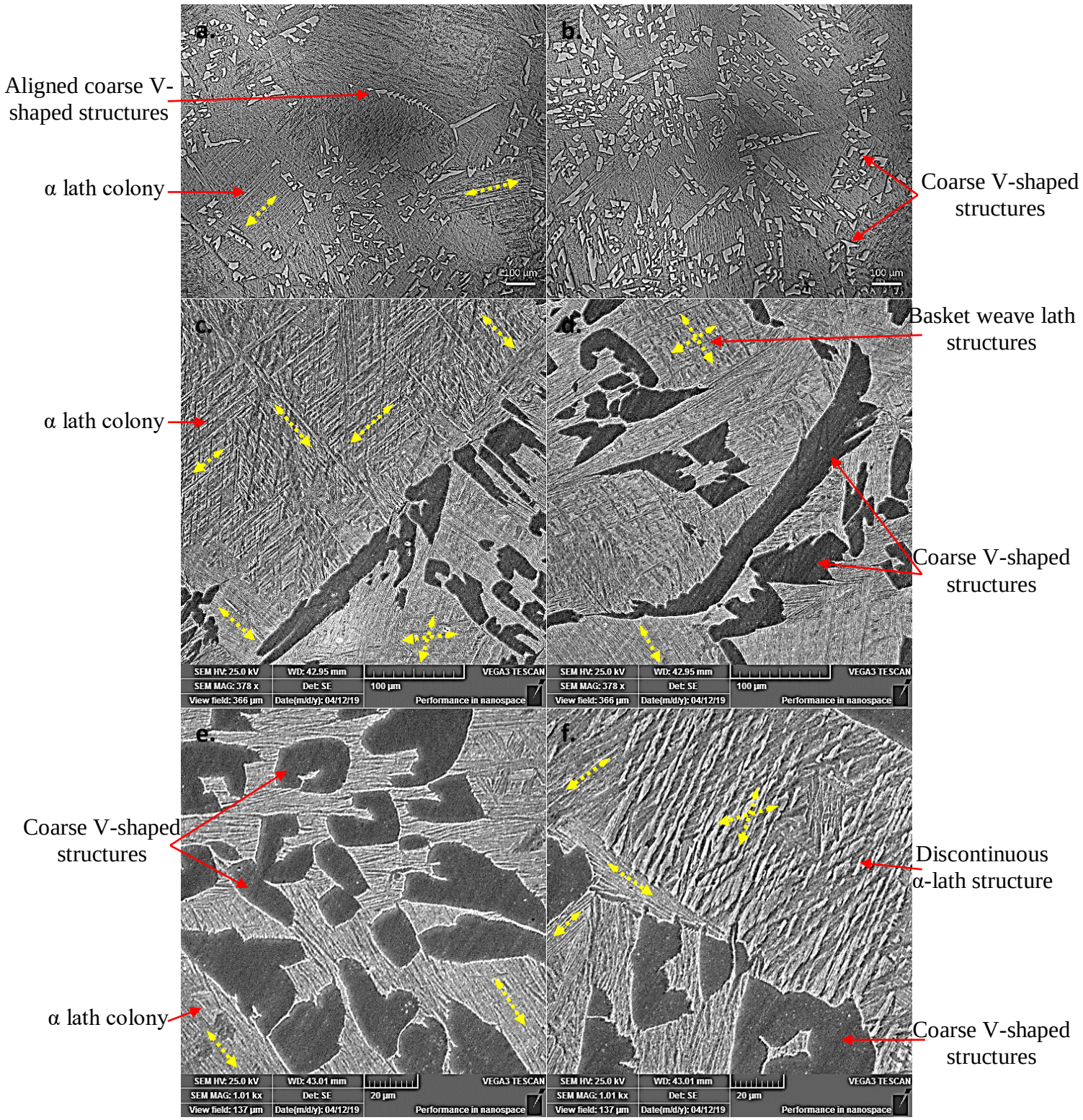

Figure 4.23 Optical and Secondary Electron (SEM) micrographs of the AC500-3D Ti6Al4V sample showing coarse V-shaped structures and α lath colonies (Widmanstätten colonies)

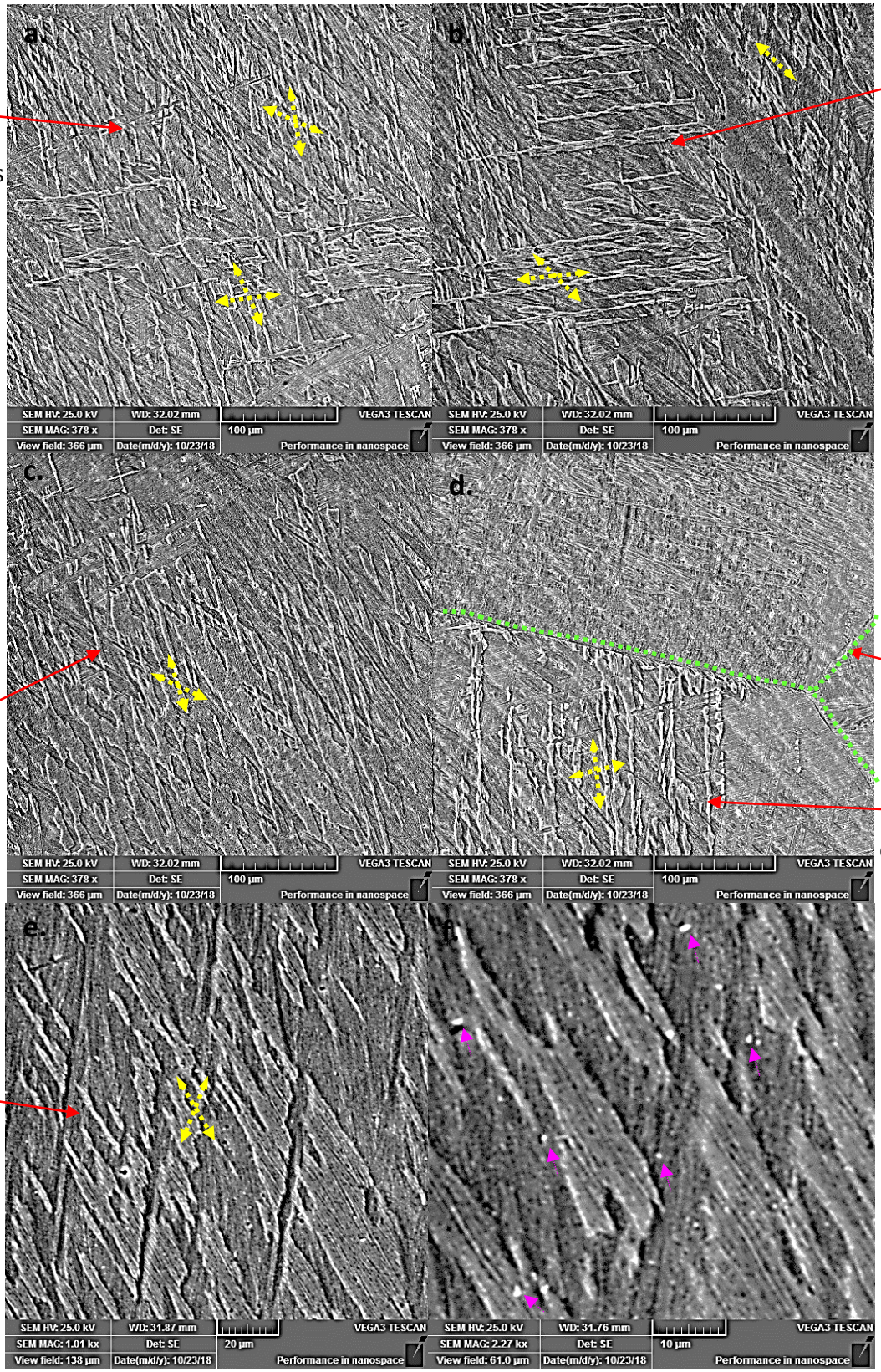

Figure 4.24 Scanning Electron Microscope (SEM) micrographs of the AC500-CV showing high volumes of distinct and relatively fine discontinuous α-lath and tiny spheroidized structures.

The AC500-3D sample had approximately 29% higher hardness than the AC500-CV with average microhardness of the AC500-3D sample being 440 HV while the AC500-CV was 339. Again, the AC500-3D sample had the highest hardness in this group when compared to all the heat-treated samples and the as-printed sample. The hardness of the AC500-3D sample was approximately 9% higher than the as-printed sample. Figure 4.25 shows the microhardness of the observed fine discontinuous lath structures in the AC500-CV sample compared with the V-shaped and the basketweave lath structures in the AC500-3D sample. In the AC500-CV sample, the observed needle-like discontinuous α-lath structures had higher hardness when compared to the coarse discontinuous α-lath structures. However, the V-shaped structures in the AC500-3D sample were extremely harder than all the observed microstructural features in the AC500-CV sample as shown in Figure 4.25.

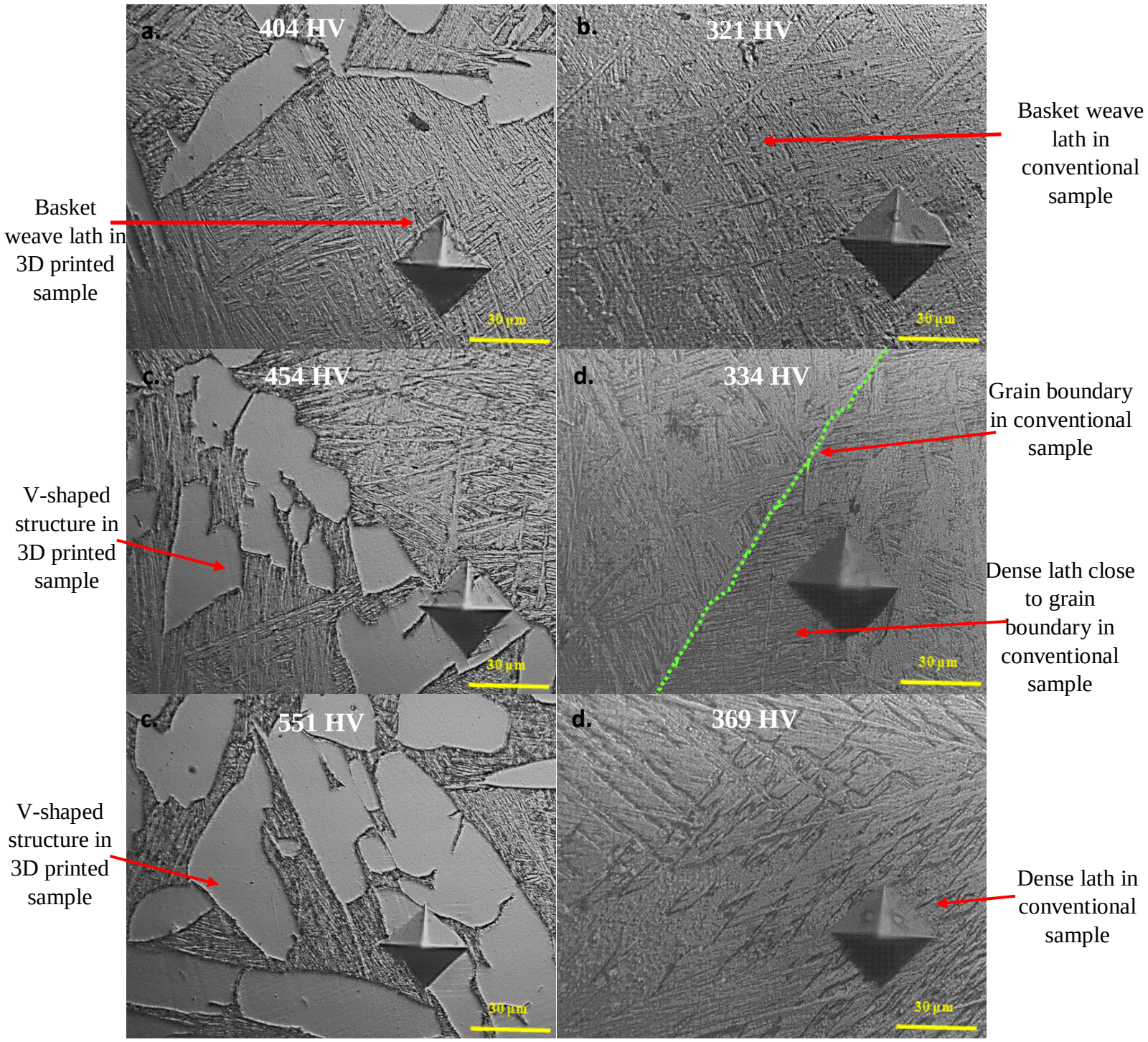

Figure 4.25 Microhardness indentations on the different structures observed in AC500-3D and AC500-CV Ti6Al4V samples

Again, after solutionization at 1080°C and air cooling, another group of both the 3D-printed and conventional Ti6Al4V samples were aged at 800°C for 4 hours, from here on referred to as AC800-3D and AC800-CV samples respectively. Figure 4.26 shows the optical and Secondary Electron (SEM) micrographs of the AC800-3D sample showing non-distinct V-shaped structures, basketweave, fine continuous and discontinuous α lath colonies with increasing misorientations. Figure 4.27 shows typical micrographs of the AC800-CV sample which had high volumes of distinct continuous and discontinuous α-lath, globularized lath structures and spheroids. The α-lath structures were relatively fine with distinct lath orientations. Globularized lath structures were the dominant structures observed in this specimen. In addition to the globularized lath structures, tiny spheroids were also observed as shown in Figure 4.27(d) to (f). Again, there were no V-shaped structures observed in this sample just like all the conventional solutionized, air-cooled and aged samples. The AC800-3D sample had a 16% higher hardness than the AC800-CV sample with an average microhardness of 391 HV for the AC800-3D while the AC800-CV had 337 HV.

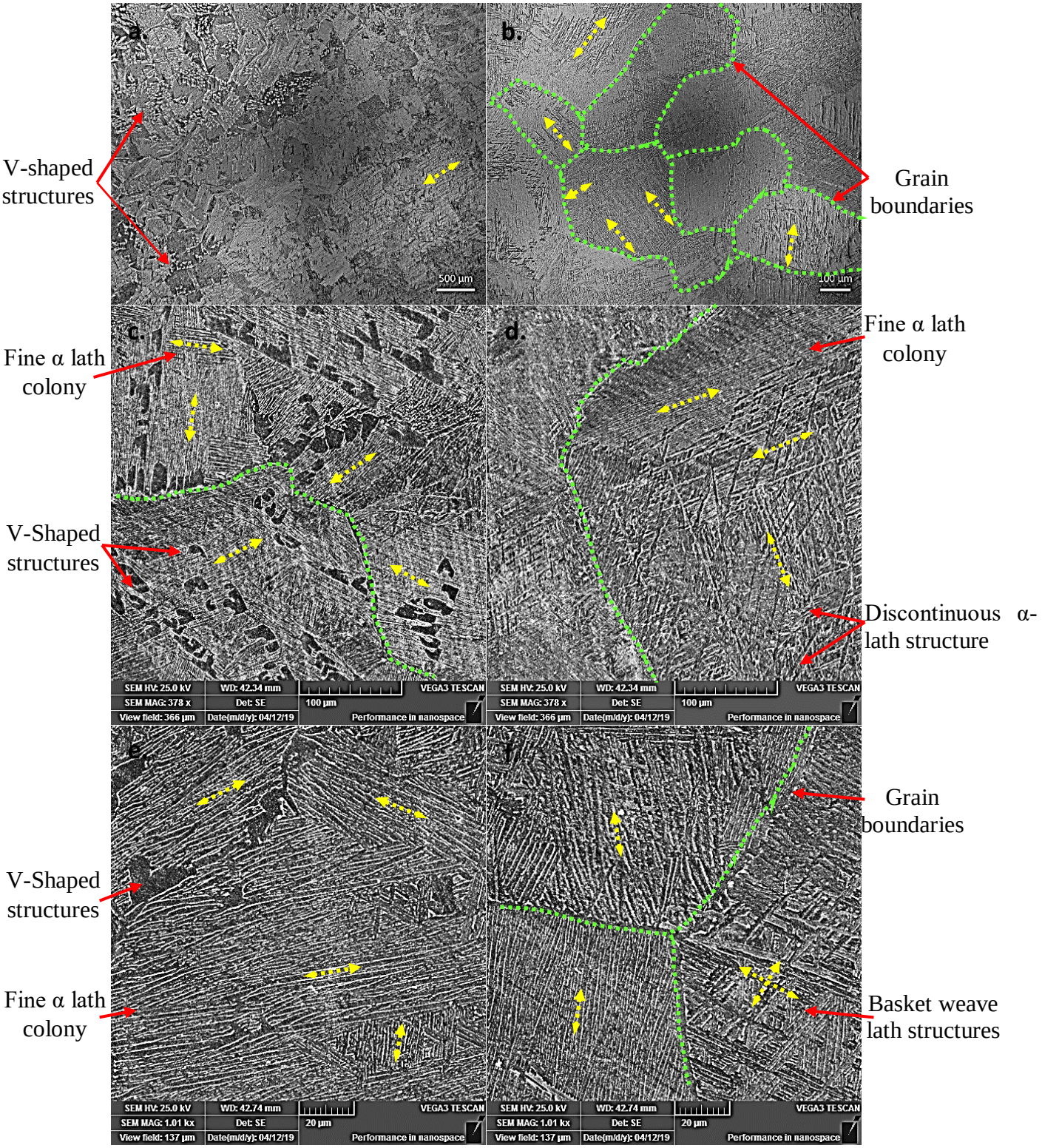

Figure 4.26 Optical and Secondary Electron (SEM) micrographs of the AC800-3D Ti6Al4V sample showing non-distinct V-shaped structures and fine α lath colonies (Widmanstätten colonies) with increasing misorientations

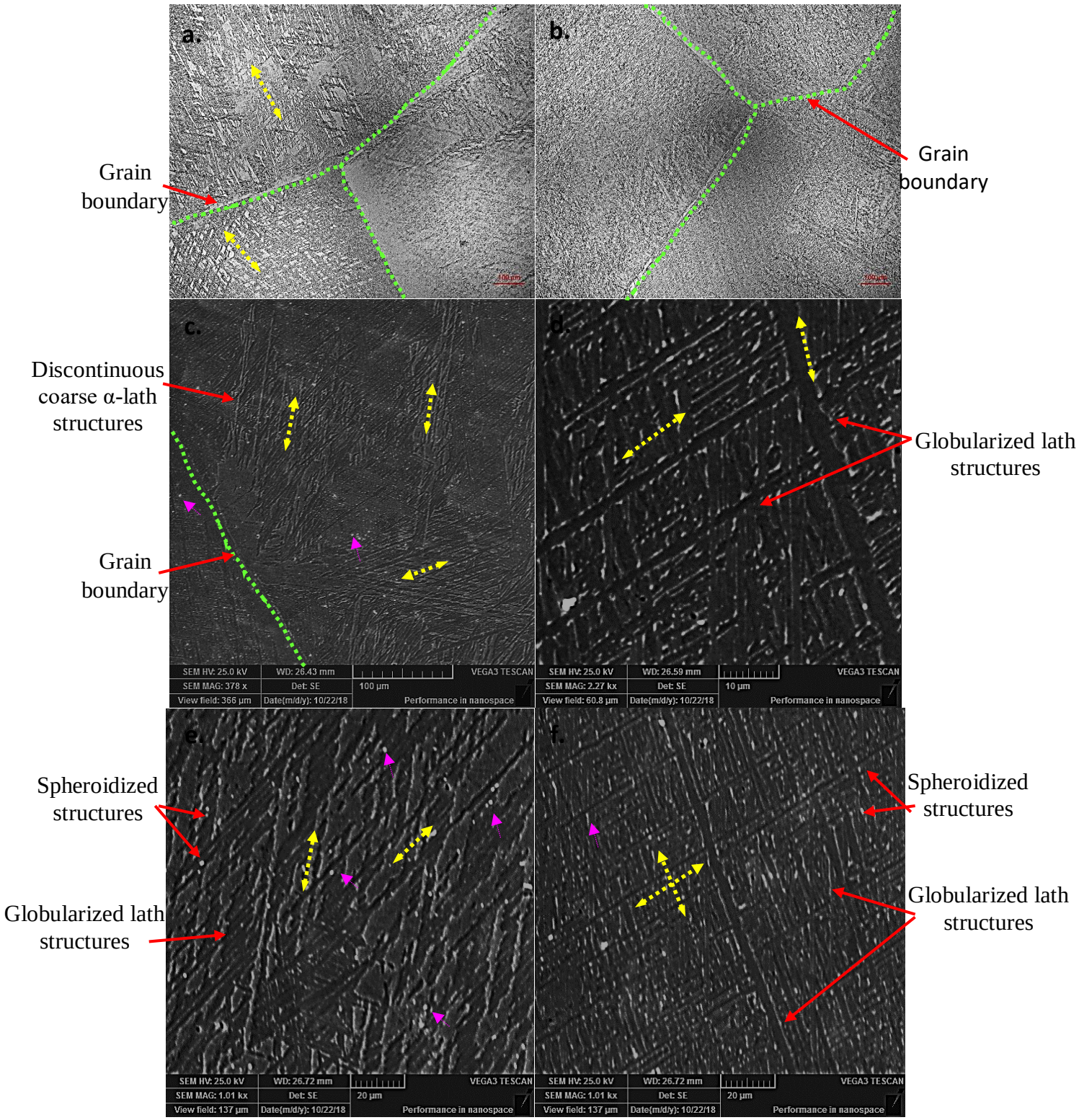

Figure 4.27 Scanning Electron Microscope (SEM) micrographs of the AC800-CV showing high volumes of distinct and relatively coarse discontinuous and continuous α-lath structures, globularized and spheroidized α structures

Figure 4.28 shows the effect of air-cooling and aging on the average microhardness of 3D-printed and conventional Ti6Al4V titanium alloy. Compared to the air-cooled samples, the water quenched samples had a relatively higher hardness. Similar to the water quenched samples' hardness, the 3D printed samples had higher average hardness values compared to the conventionally manufactured titanium alloys. The AC200-3D and AC500 are the only conditions with a hardness of over 400 HV among all air-cooled samples with the AC500-3D having the highest hardness as shown in Figure 4.28.

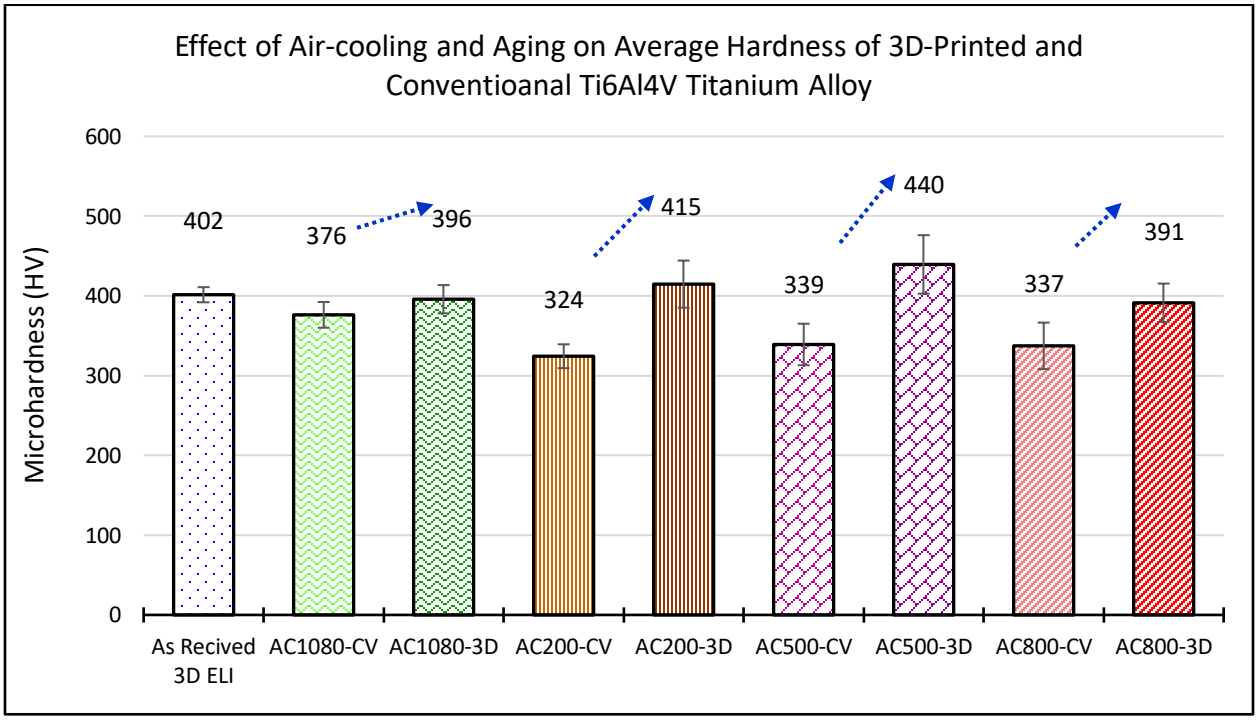

Figure 4.28 Effect of Air-Cooling and Aging on the average microhardness of 3D-printed and conventional Ti6Al4V titanium alloy

4.4 Effect of Heat Treatment on the Wear Properties of the 3D–Printed and Conventional Ti6Al4V Alloys

Prior to wear tests, the polished samples were studied using an optical profiler to document the surface roughness. Table 4.1 shows surface roughness values for the polished samples measured before wear test for both the 3D printed and conventional samples. Some sample surfaces that the surface roughness was investigated are shown in Figure 4.29. Figure 4.30 shows the graphs of the Coefficient of Friction (COF) and Mass Loss (ML) after wear tests for the water-quenched 3D-printed and conventional Ti6Al4V titanium alloys. The coefficient of friction (COF) data was continuously recorded by the UMT Tribolab system during the wear test. Figure 4.30 (a) shows the mean COF values for all the water-quenched samples. Of all the 3D printed samples, the WQ500-3D had the highest COF while the WQ200-3D had the lowest COF. Despite the fact that the WQ1080-CV had the same average hardness as the WQ500-3D sample, the mean COF of the WQ500-3D sample was relatively higher than the WQ1080-CV sample as shown in Figure 4.30(a). Also, of all the 3D printed samples, the WQ1080-3D had the lowest mass loss with the WQ500-3D sample having the highest mass loss when compared to all the water-quenched samples as shown in Figure 4.30(b). Even though the WQ200-CV had a significantly lower COF, it had the 2nd highest mass loss after the WQ500-3D sample.

Table 4.1 Surface roughness of Ti6Al4V alloys at different heat treatment conditions (nm).

Condition	As printed	WQ1080	WQ200	WQ500	WQ800	AC1080	AC200	AC500	AC800
Conventional	1.437	1.208	1.487	1.628	1.376	0.989	1.246	1.202	0.964
3D printed	1.573	1.896	1.504	1.569	1.222	1.320	1.591	1.473	1.791

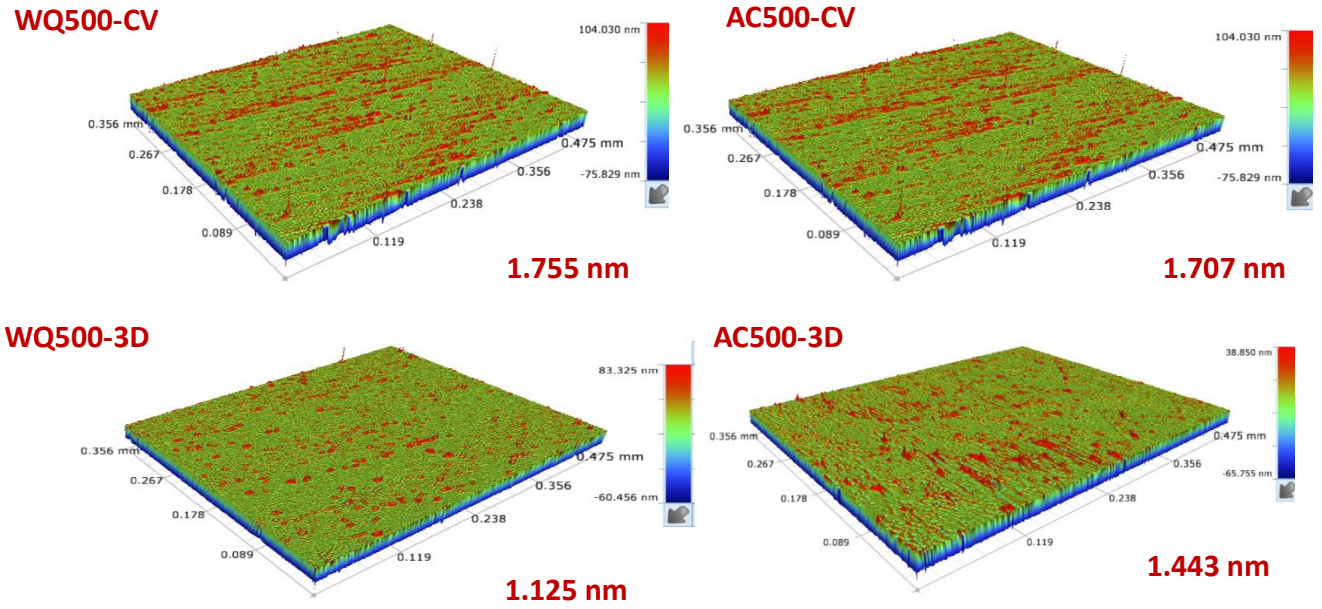

Figure 4.29 Examples of 3D printed and conventional Ti6Al4V surfaces that surface roughness measurement were investigated on.

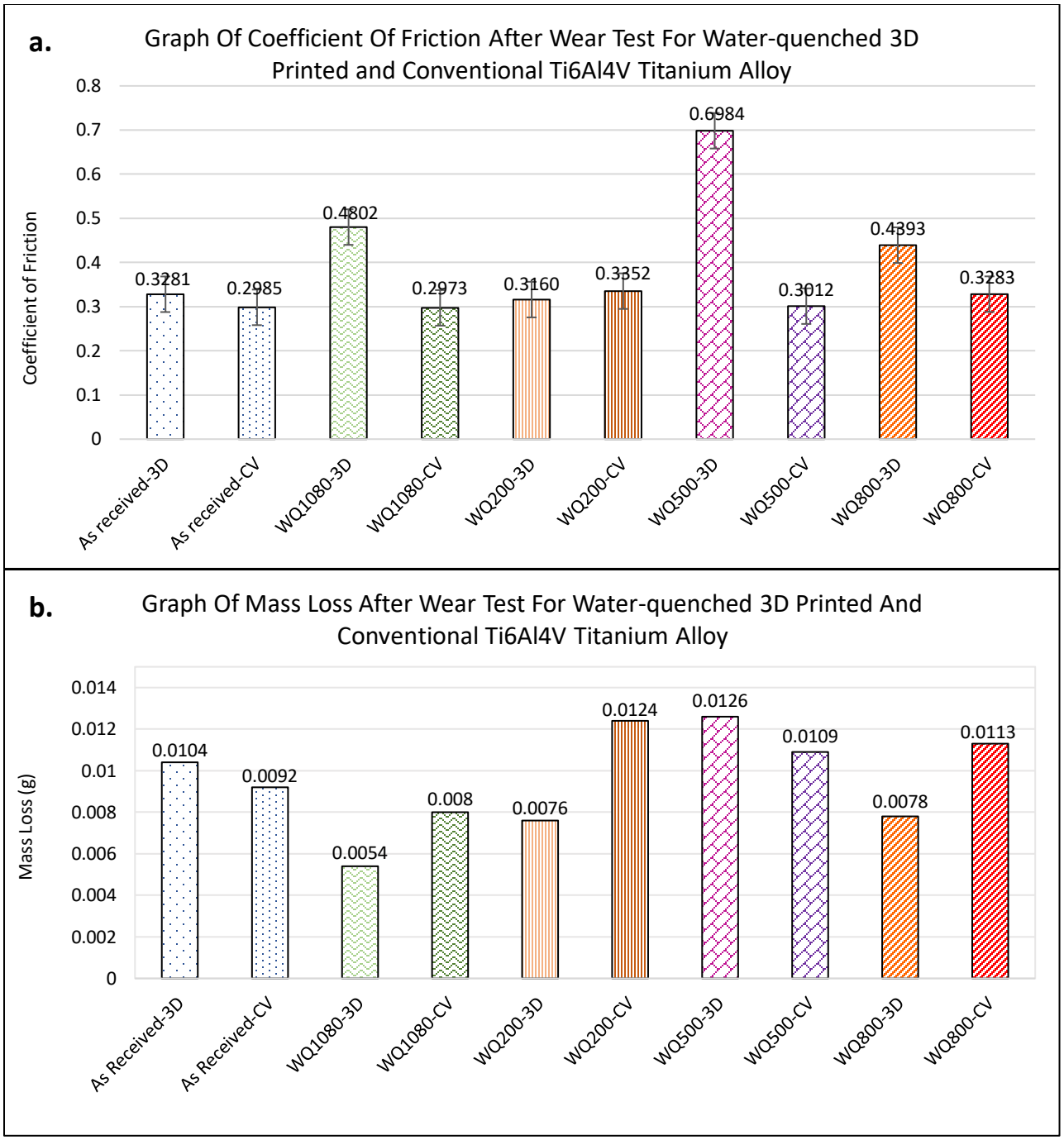

Figure 4.30 Graph of (a) Coefficient of Friction (b) Mass Loss after wear tests for water-quenched 3D-printed and conventional Ti6Al4V titanium alloy

Figure 4.31 shows the graphs of the Coefficient of Friction (COF) and Mass Loss (ML) after wear tests for the air-cooled 3D-printed and conventional Ti6Al4V titanium alloys. Again, of all the 3D printed samples, the AC500-3D had the highest COF while the as-printed sample had the lowest COF. On the other hand, even though the COF of the AC500-3D sample was the highest, it had a

significantly lower mass loss with the AC200-3D having the lowest mass loss followed by the AC800-3D as shown in Figure 4.31. The mass losses of the air-cooled samples were relatively lower than the mass loss of the water-quenched samples. Also, the conventional samples appeared to have a higher mass loss than the 3D printed samples as shown in both Figures 4.30 and 4.31.

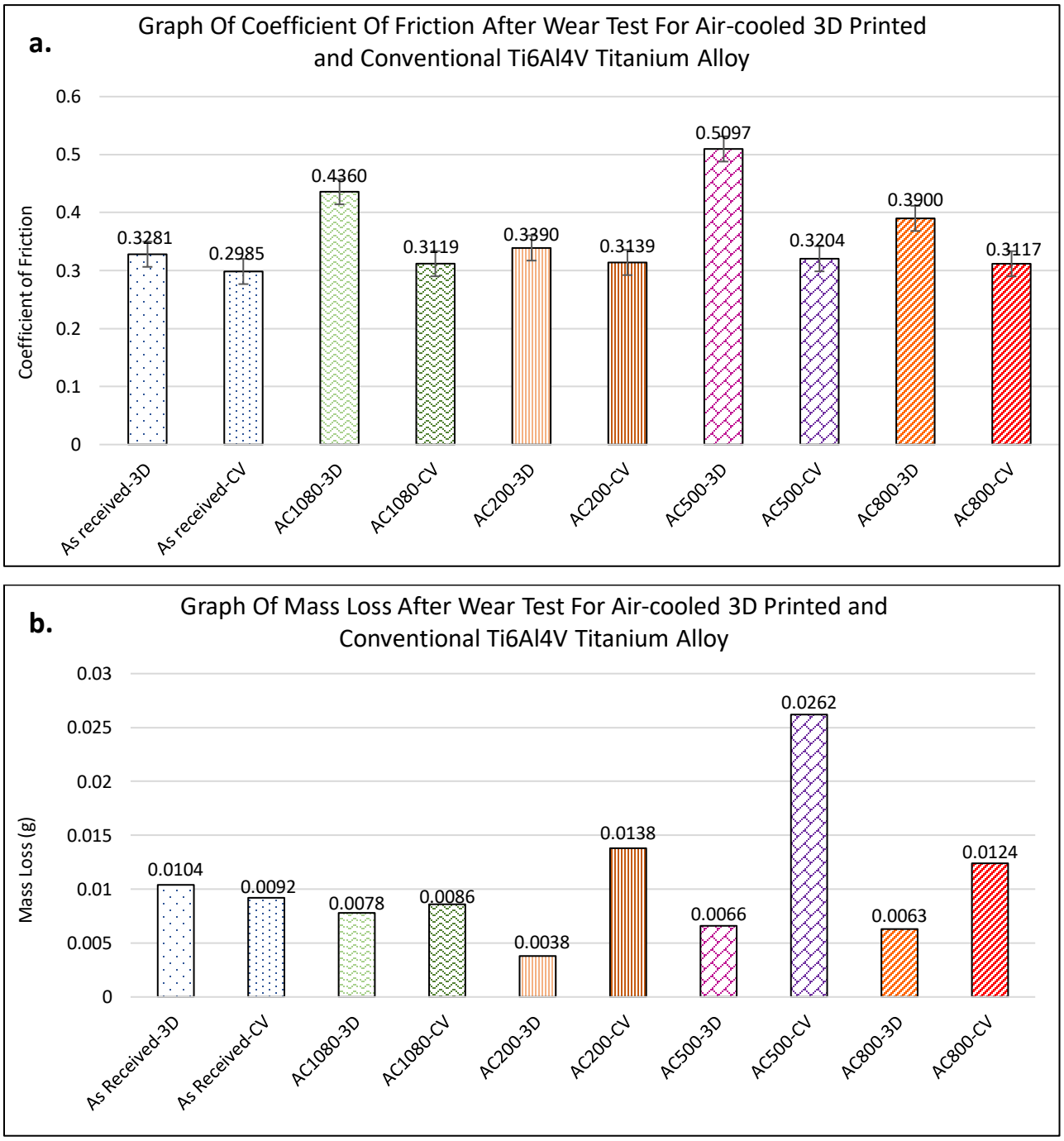

Figure 4.31 Graph of (a) Coefficient of Friction (b) Mass Loss after wear tests for water-quenched 3D-printed and conventional Ti6Al4V titanium alloy

Figures 4.32 and 4.33 show the optical profilometry scans of sections of the wear tracks for the as-printed, water-quenched and air-cooled samples respectively. Figure 4.32 (c) illustrates the shallowest wear track of the WQ1080-3D among all the water quenched samples as was shown by the mass loss. On the other hand, among all the air-cooled samples, AC200-3D which is shown in Figure 4.33 (c) had the lowest mass loss as shown by the optical profiler scans and the mass loss graphs. Of all the samples, the wear tracks were characterized by ridges and furrows with some samples having smooth ridges and furrows while other wear tracks had undulations along the ridges and furrows as shown in Figures 4.32 and 4.33.

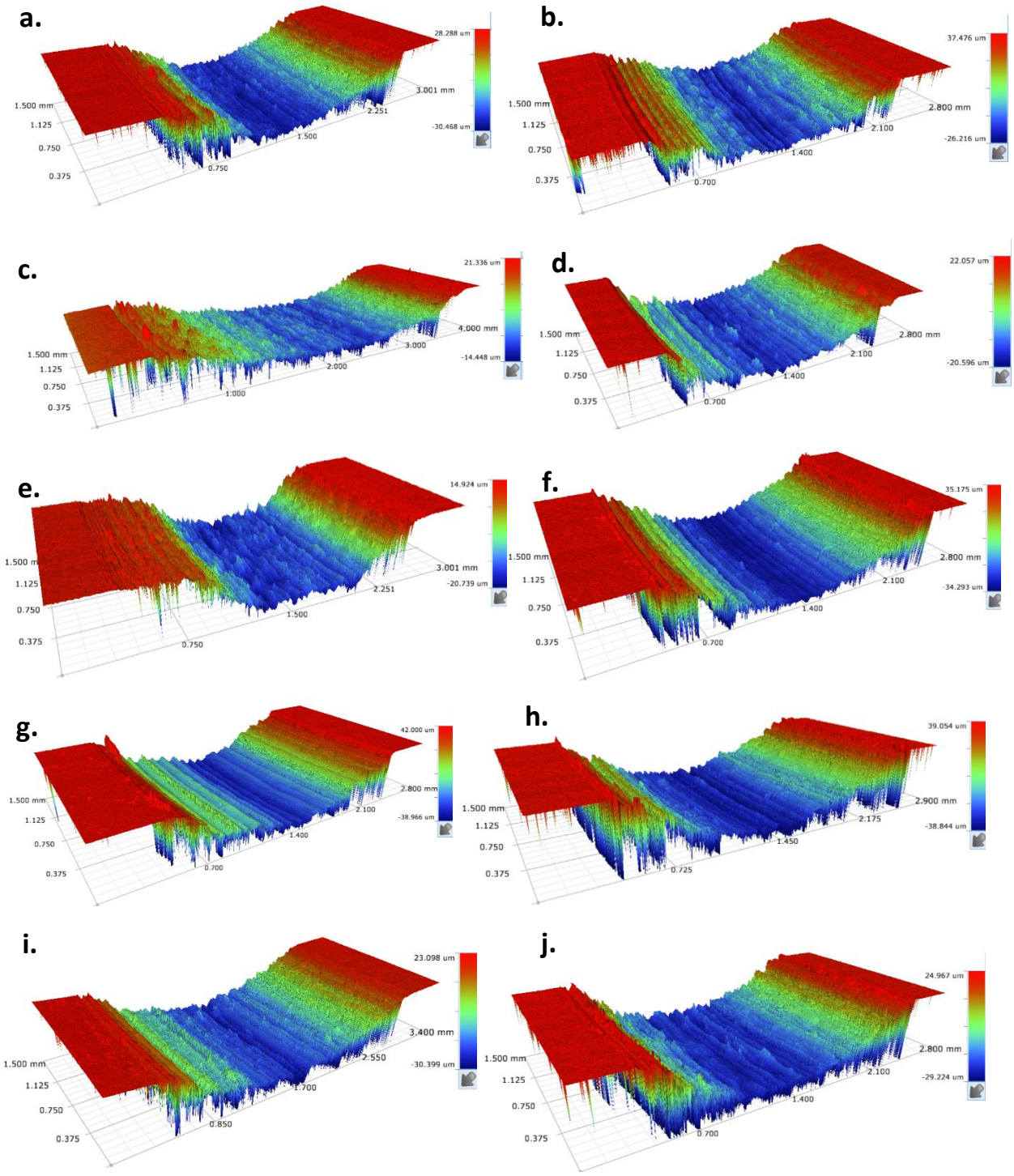

Figure 4.32 Optical profilometry scans of sections of the wear tracks for the as-printed and water quenched, 3D printed and conventional Ti6Al4V samples. a. AR-3D b. AR-CV c. WQ1080-3D d. WQ1080-CV e. WQ200-3D f. WQ200-CV g. WQ500-3D h. WQ500-CV i. WQ800-3D j. WQ800-CV.

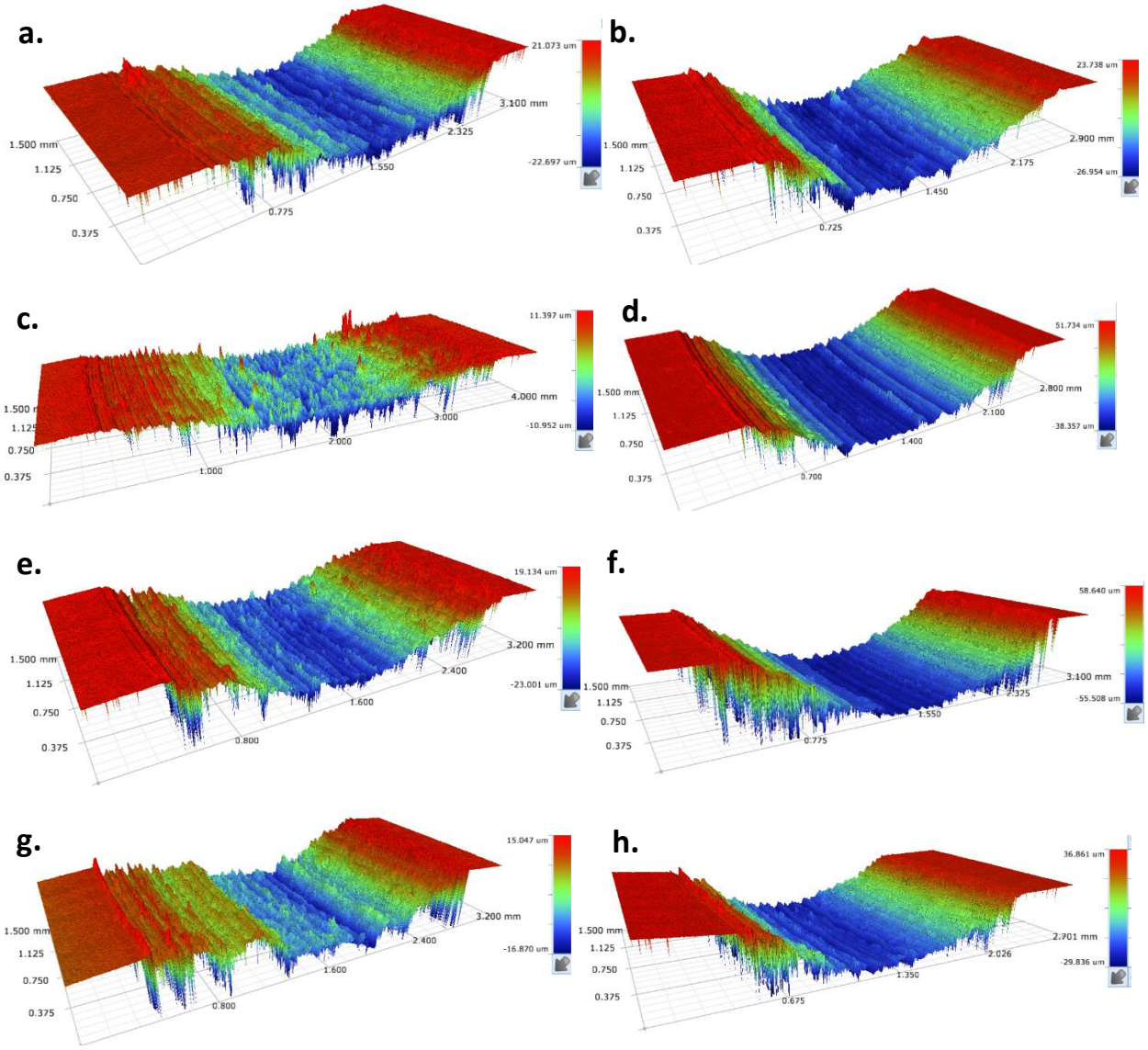

Figure 4.33Optical profilometry scans of sections of the wear tracks for the as-printed, air-cooled 3D printed and conventional Ti6Al4V alloys. a. AC1080-3D b. AC1080-CV c. AC200-3D d. AC200-CV e. AC500-3D f. AC500-CV g.AC800-3D h. AC800-CV.

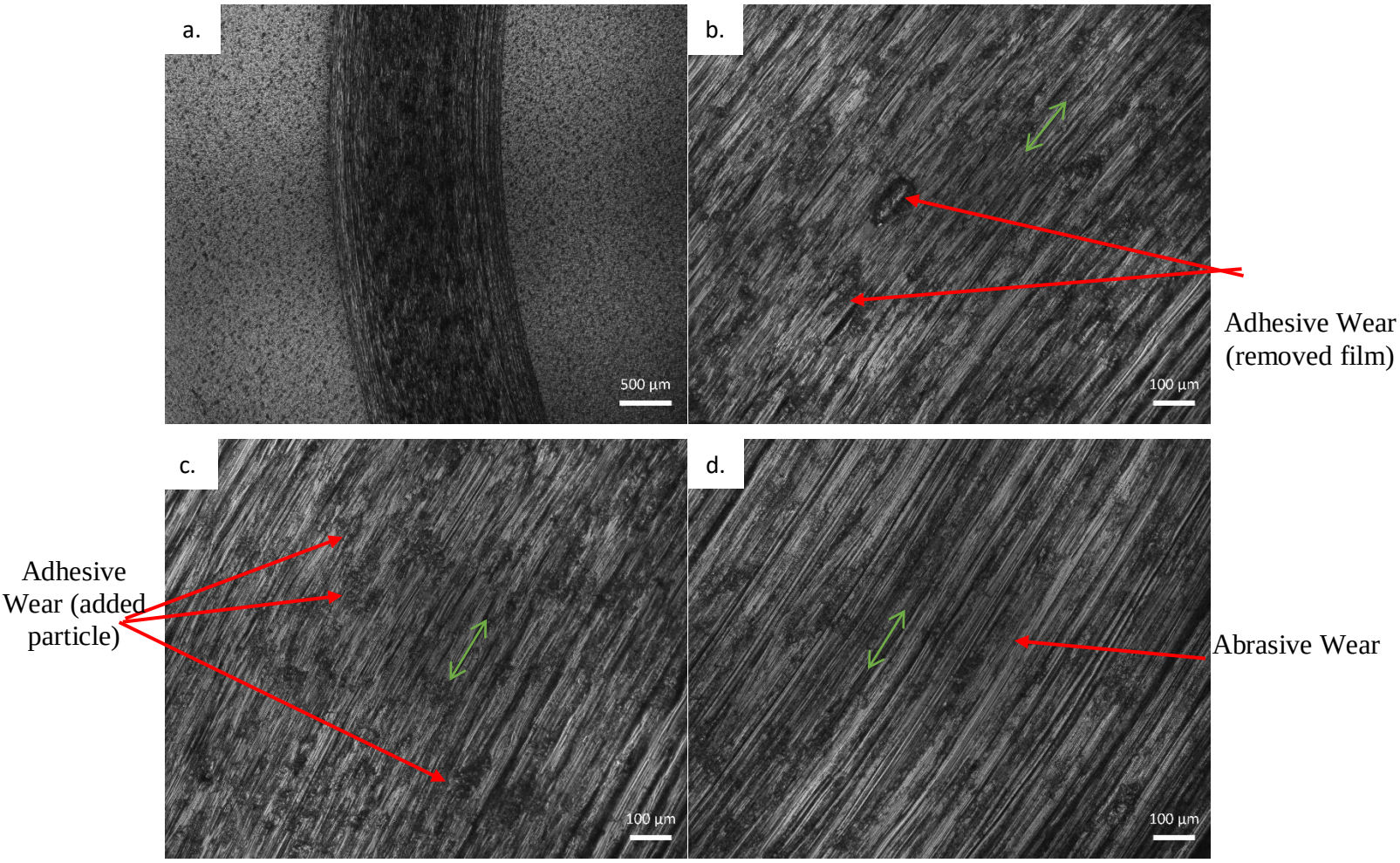

Figure 4.34 Micrographs showing wear mechanisms of as received 3D Printed Ti6Al4V ELI.

Figure 4.34 reveals the micrographs of the 3D printed Ti6Al4V wear track after 90 minutes of rotary wear test with NaCl as a lubricant. Two different wear mechanisms can be seen at different sections of the round wear track. The adhesive wear mechanism is shown in Figure 4.34b and 4.34c. This type of wear happens as a result of sliding two parts with different hardness against each other. Particles from the low hardness part cold-weld to the part with higher hardness. Depending on different microstructure, different hardness was expected, which explains the reason behind particle peel off in Figure 4.34b and stack up in Figure 4.34c. Abrasive wear mechanism is displayed in Figure 4.34d which could be as a result of 2 body or 3 body wear. In addition, the grooves observed in this condition are mostly shallow.

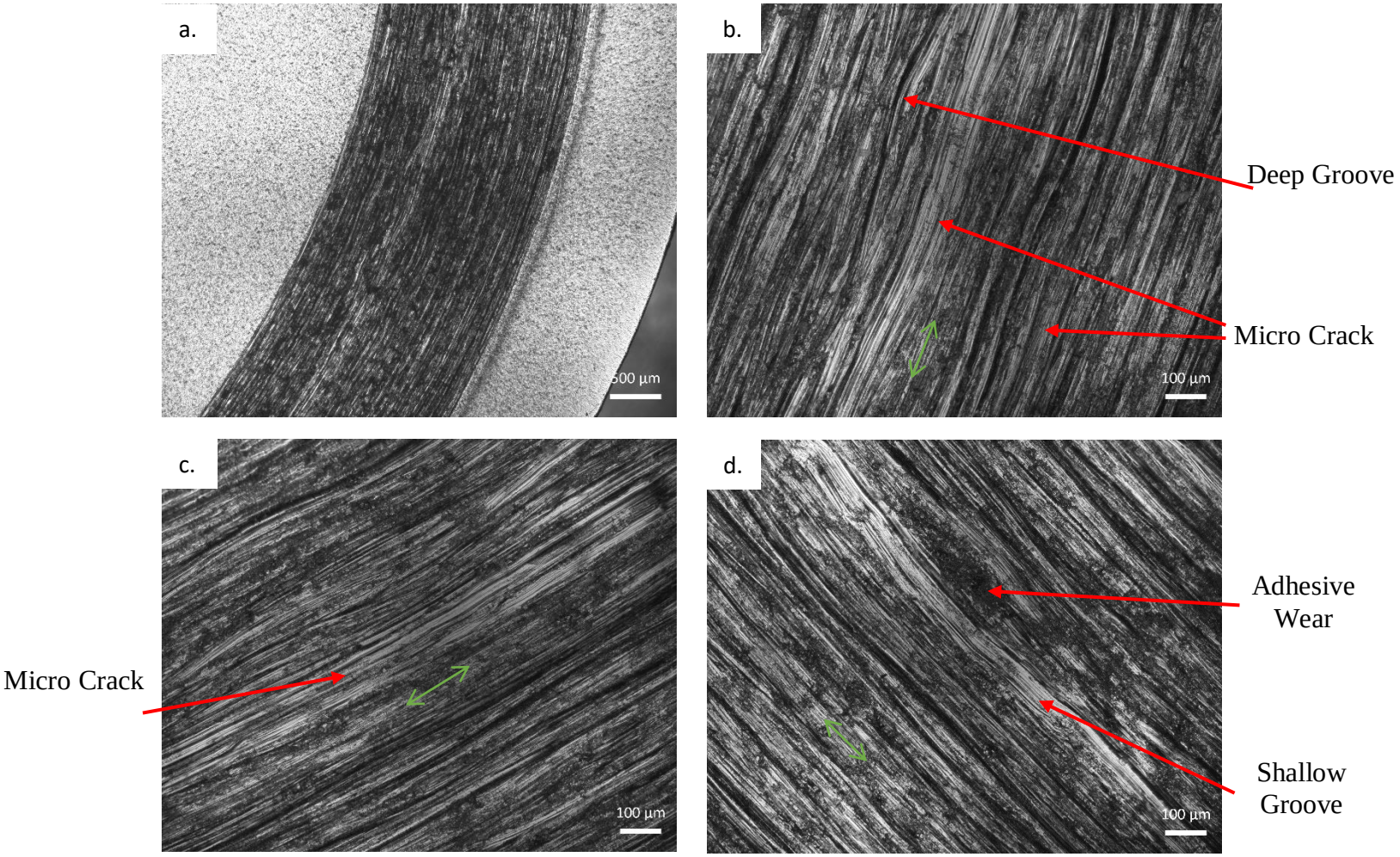

Figure 4.35 Micrographs showing wear mechanisms of as received conventional Ti6Al4V ELI

Different wear mechanisms observed after rotary wear test on the as-received conventional medical-grade Ti6Al4V are presented in Figure 4.35. Abrasive wear mechanism is observed in all micrographs while in some area grooves are deeper. Microcracks within the wear track in Figure 4.35b and 4.35d shows the early stages of the fatigue wear mechanisms. Similar to the as-received 3D printed specimen, the adhesive wear mechanism can be seen in some areas (Figure 35d). In general, both as-received specimens (3D and conventional) had adhesive and abrasive wear mechanisms in common while micro cracks present is their difference.

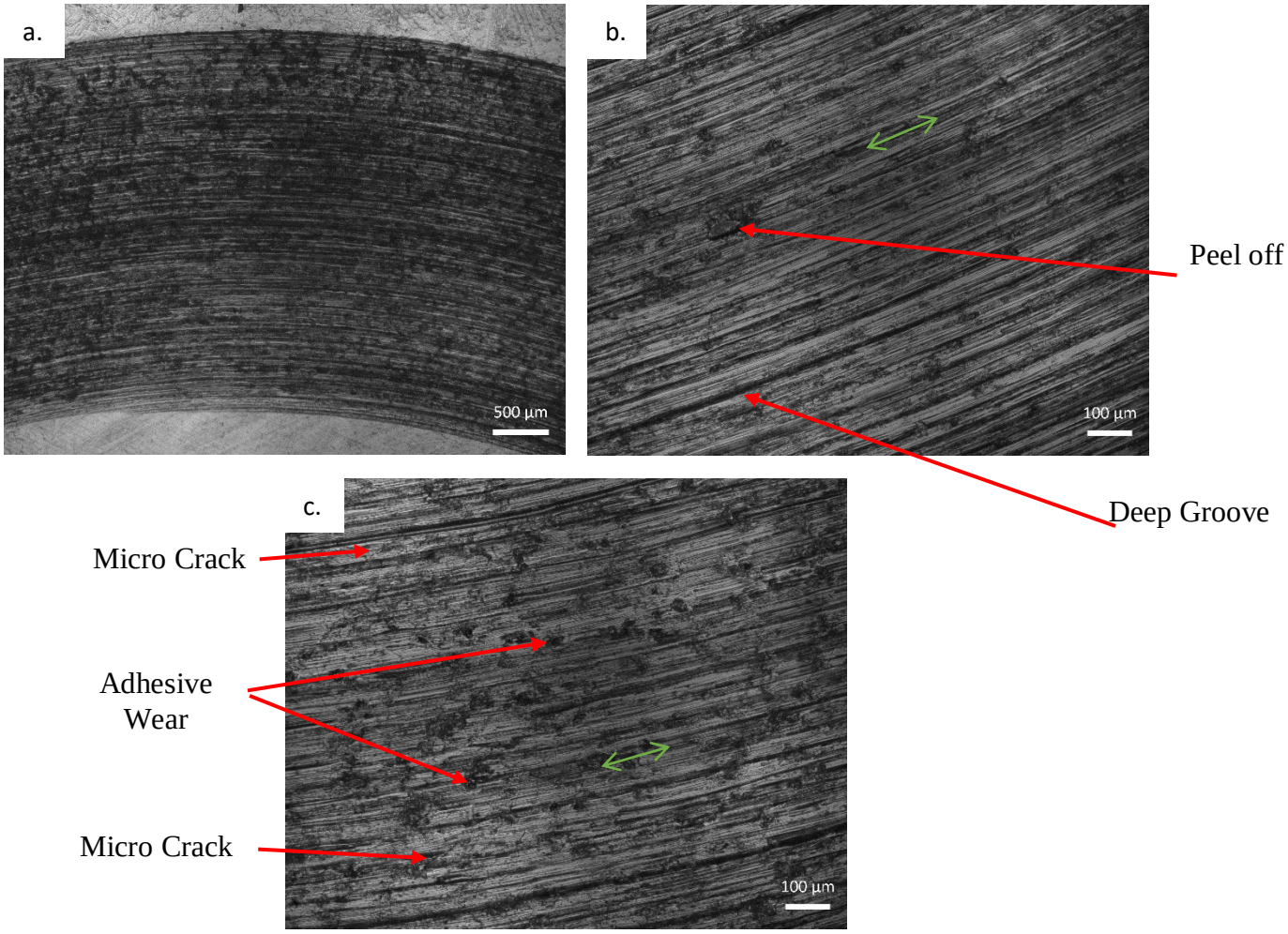

Figure 4.36 Micrographs showing wear mechanisms of 3D Printed Ti6Al4V ELI at WQ1080 condition.

Adhesive and abrasive wear mechanisms were the two common wear mechanisms observed in additively manufactured Ti6Al4V ELI solutionized at 1080°C followed by water quenching. Few micro-cracks were visible in between wear tracks. Figure 4.36 illustrates the three wear mechanisms in this condition. Some deep grooves as a result of abrasive wear are displayed in figure 4.36 b, and plenty of the materials peel off can be seen in figure 4.36 c.

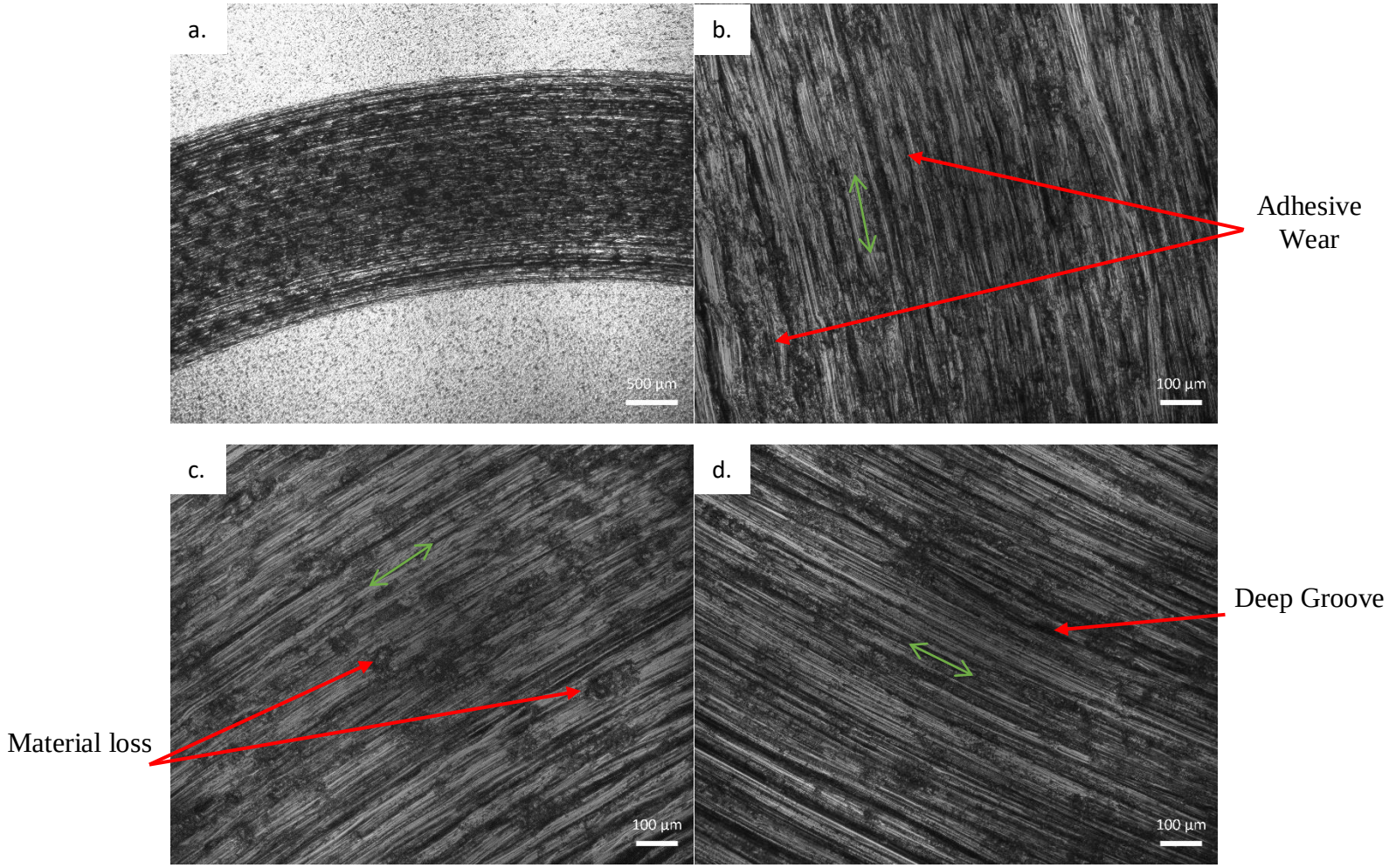

Figure 4.37 Micrographs showing wear mechanisms of conventional Ti6Al4V ELI at WQ1080

Wear track of conventional WQ1080 is shown in Fig 4.37. Abrasive and adhesive wear mechanisms can be seen in all micrographs. Some large material loss areas are displayed in Figure 4.37. b and 4.37.c. Also, the Abrasive wear mechanism was observed as a form of grooves with different depth following the wear track.

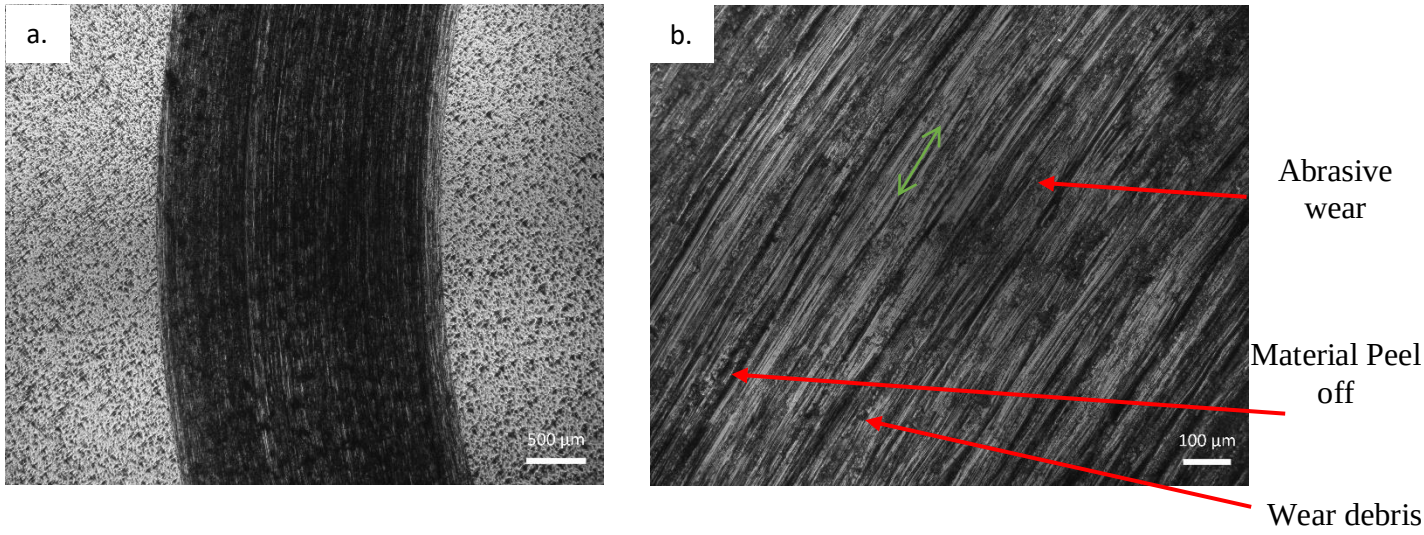

Figure 4.38 Wear mechanisms of the 3D printed sample at WQ200 condition

Figure 4.38 illustrates wear tracks and mechanisms of 3D printed WQ200 after wearing against a titanium alloy round ball for 90 mins. Few adhesive wear mechanisms in the form of material loss are seen in figure 4.38 b. In the same figure, abrasive wear occurs in the same direction of the wear track, while at this condition most of the grooves are shallow.

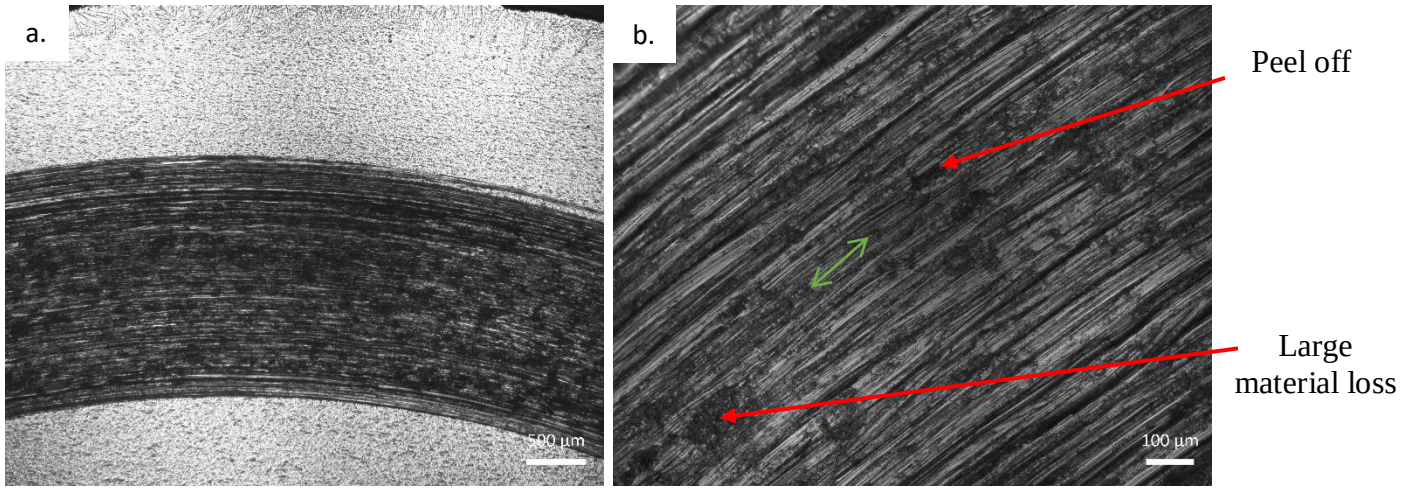

Figure 4.39 Wear mechanisms of the conventional sample at WQ200 condition

Wear track of conventional WQ200 is shown in figure 4.39. Large material peel-off is the significant feature of this wear track, while abrasive wear is causing all the grooves among the wear track.

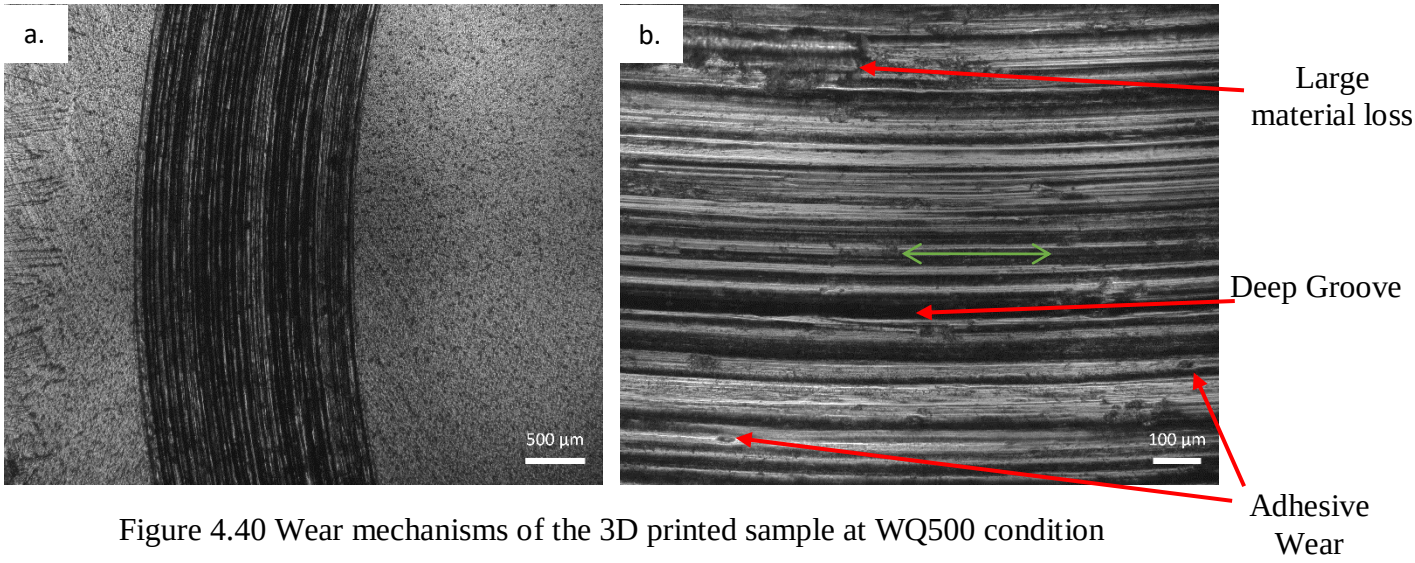

Figure 4.40 Wear mechanisms of the 3D printed sample at WQ500 condition

Wear track and mechanism of the 3D printed WQ500 is displayed in Figure 4.40. Abrasive wear is the significant wear mechanism for this condition, while there are some areas within the grooves that material loss is observed. Moreover, the grooves in this condition seem to be dramatically deep.

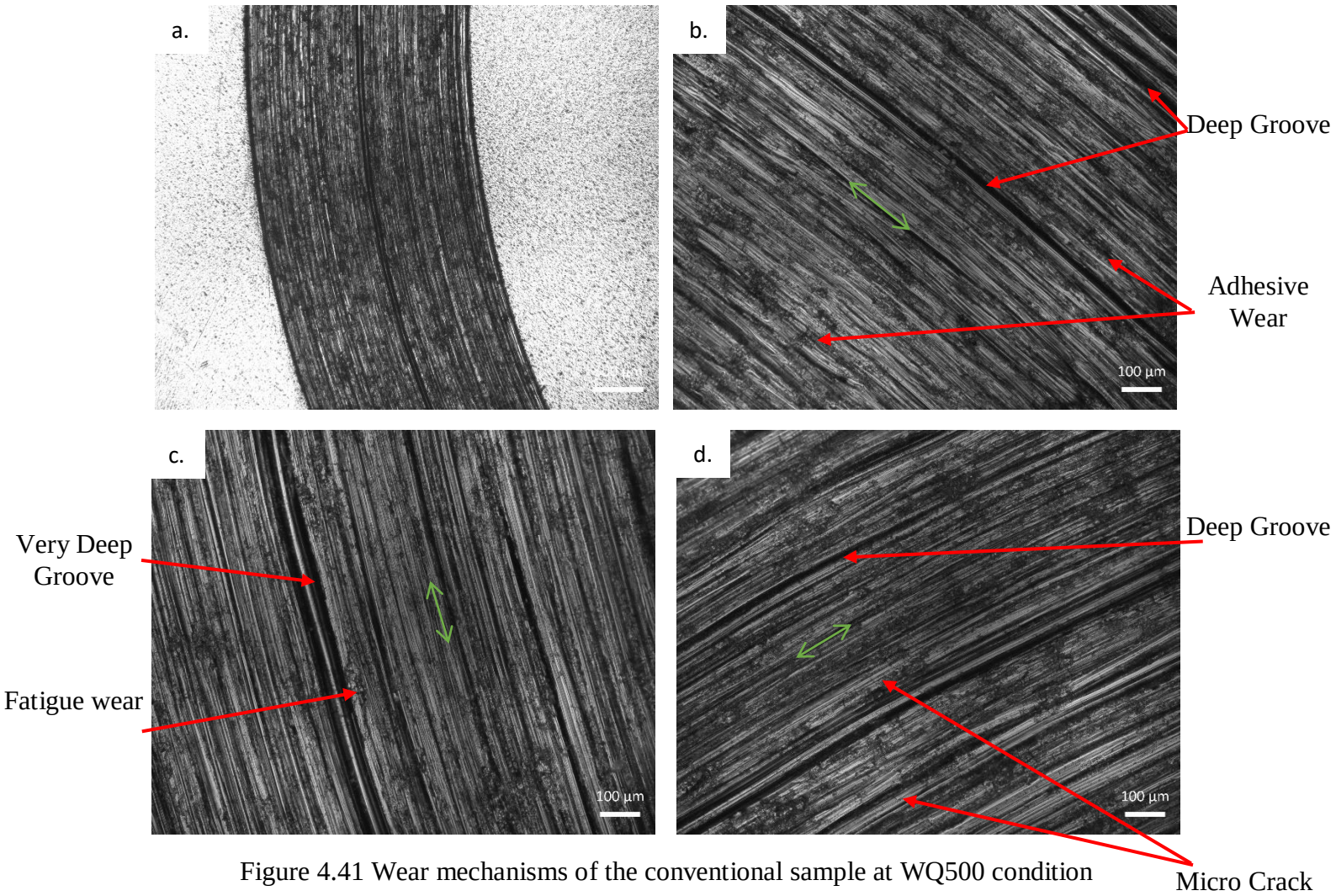

Figure 4.41 Wear mechanisms of the conventional sample at WQ500 condition

Figure 4.41 shown the wear track and mechanism of conventional WQ500 titanium alloy. In this condition, three wear mechanisms can be seen. Fig 4.41 b shows small round shaped material peel-off as well as grooves with different depth. There are two large grooves displayed in Fig 4.41.c which occurred as a result of third body abrasive wear. Some microcracks are presented in fig 4.41.c and 4.41.d, which in some areas are led to fatigue wear.

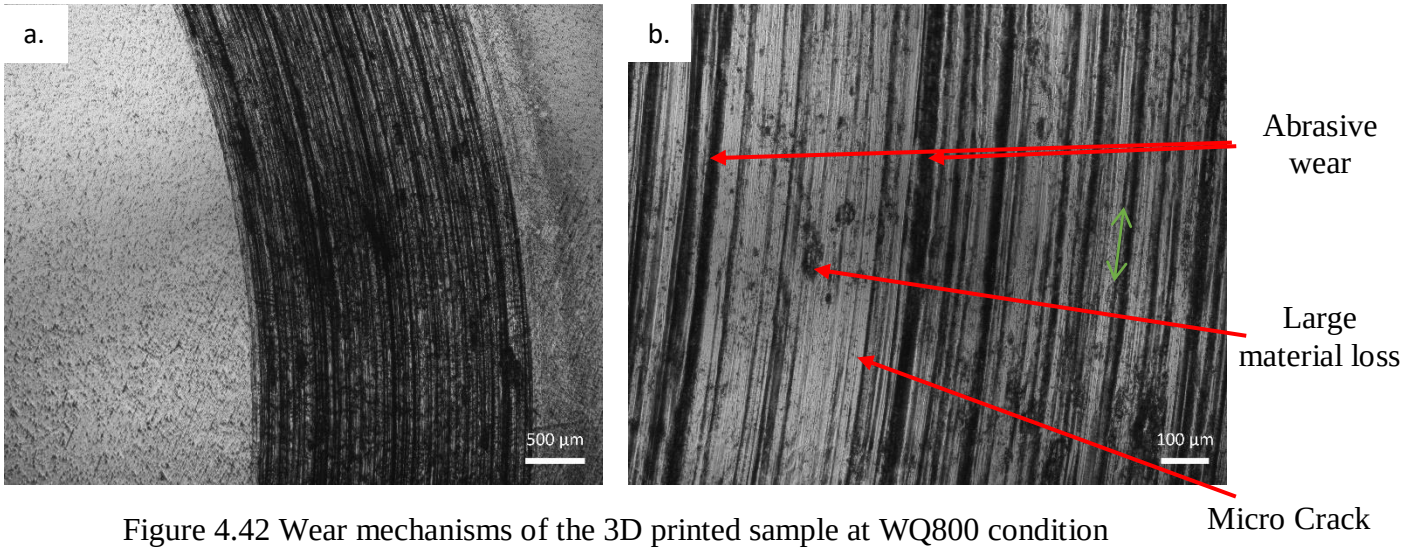

Figure 4.42 Wear mechanisms of the 3D printed sample at WQ800 condition

Wear track displayed in Fig 4.42 describes wear mechanisms seen in 3D printed WQ800. Abrasive wear can be seen in the form of grooves with different depth. Some microcracks are located on shallow grooves due to the tension and compression caused by sliding. Also, because of the different hardness in different sections, the adhesive mechanism is observed.

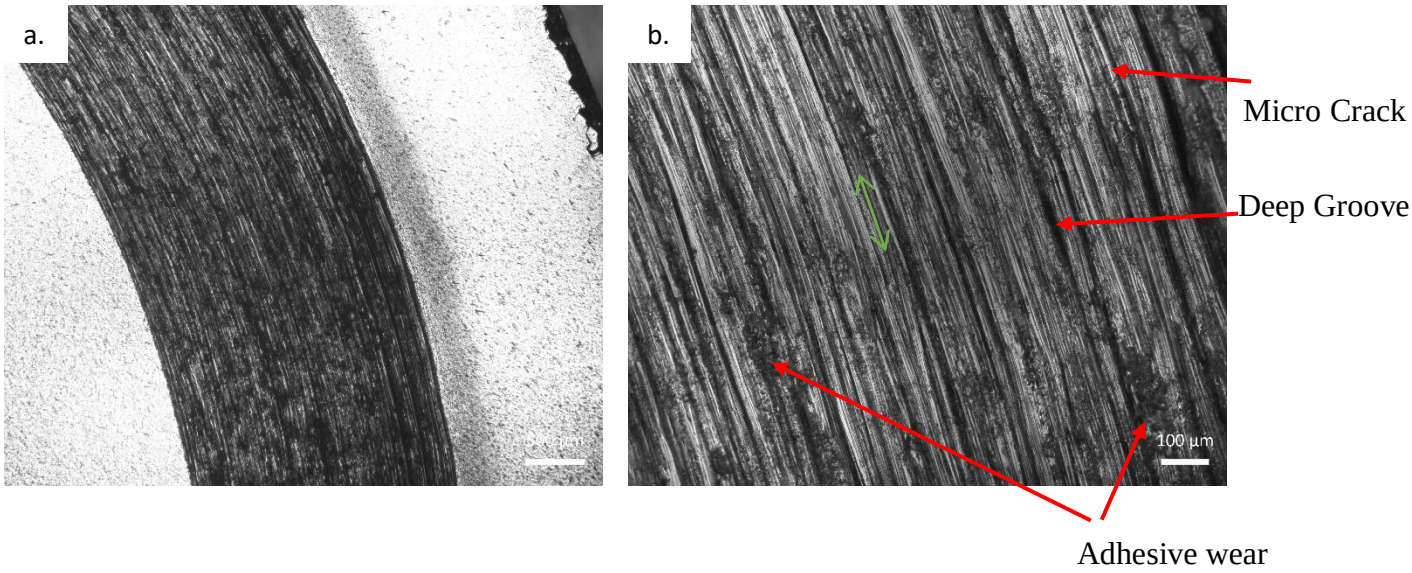

Figure 4.43 Wear mechanisms of the conventional sample at WQ800 condition

Fig 4.43 illustrates the wear track and wear mechanism related to conventional WQ800. Wear track displayed in Fig 4.43.b shows 3 different wear mechanisms; abrasive, adhesive and fatigue. Abrasive wear is shown in the form of grooves which in this condition, there are not a lot of deep grooves. The amount of material loss due to adhesive is large.

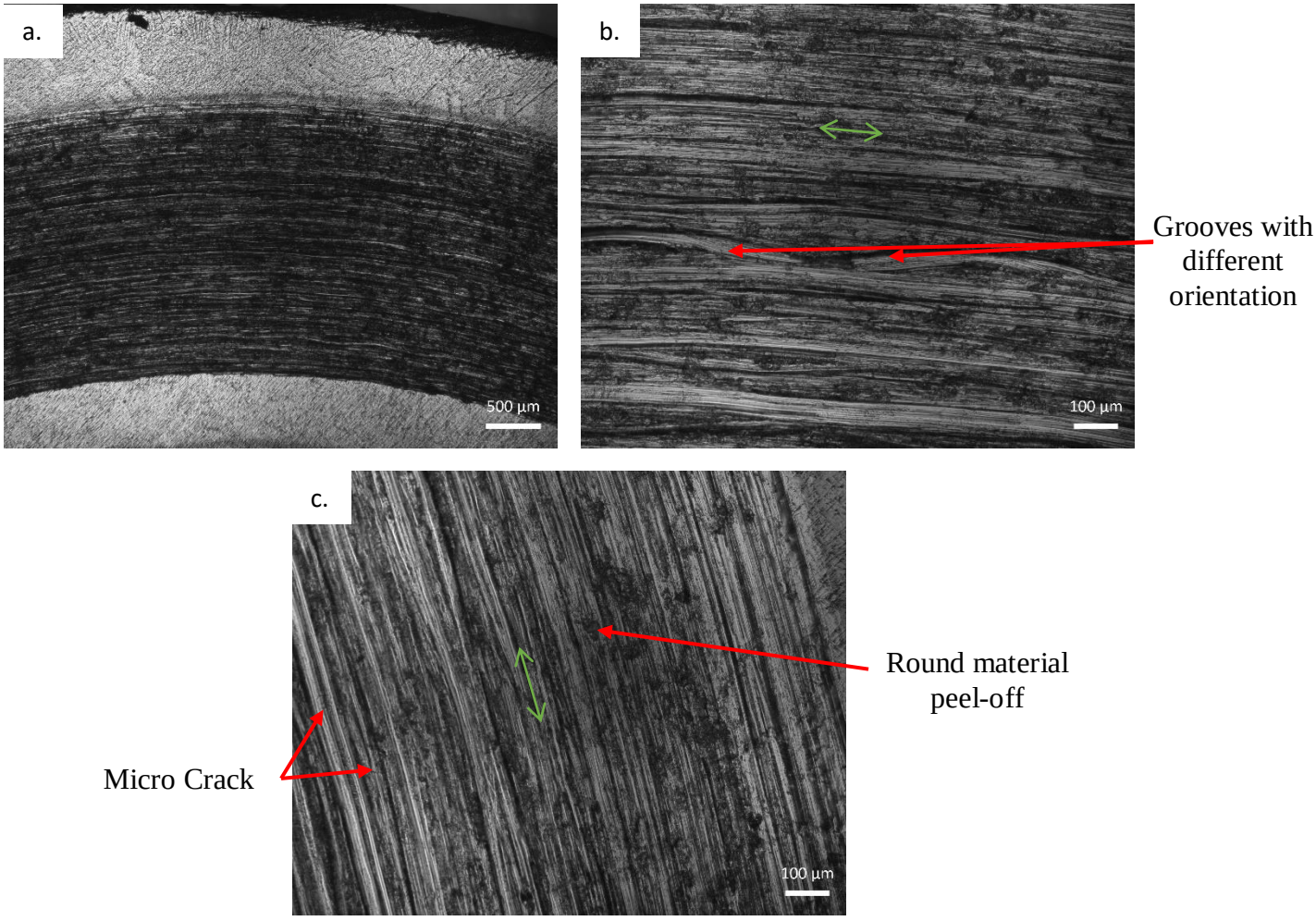

Figure 4.44 Wear mechanisms of the 3D printed sample at AC1080 condition

Wear mechanisms of 3D printed AC1080 are shown in fig 4.44. Abrasive wear shown in fig 4.44.b is displayed as grooves which at some sections the orientation is tilted. In fig 4.44.c, beside the groove lines aligned with wear track, microcracks and adhesive wear is observed. Wear tracks described in Fig 4.45 are assigned to conventional AC1080. Abrasive and adhesive wear can be seen in all displayed micrographs.

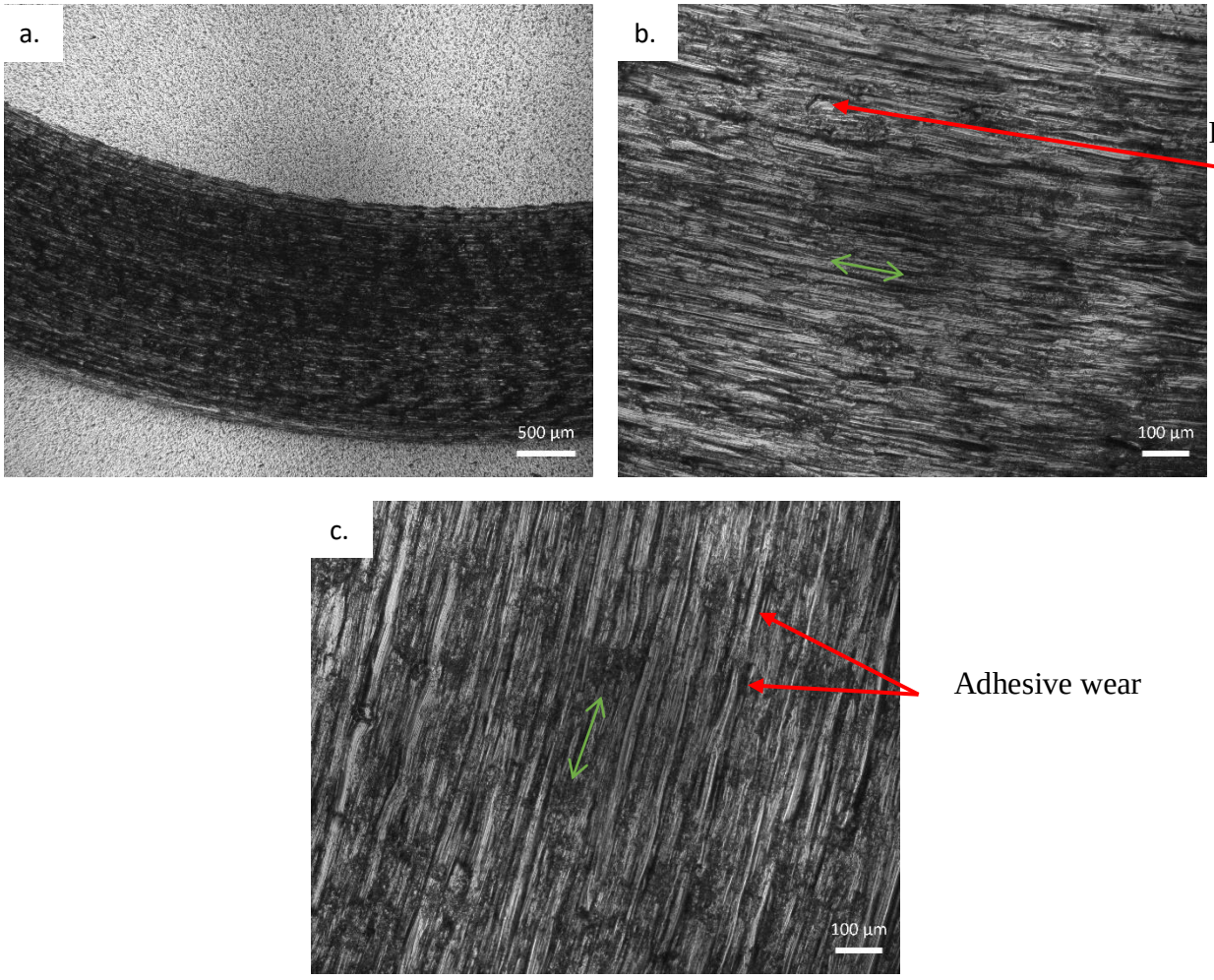

Figure 4.45 Wear mechanisms of the conventional sample at AC1080 condition

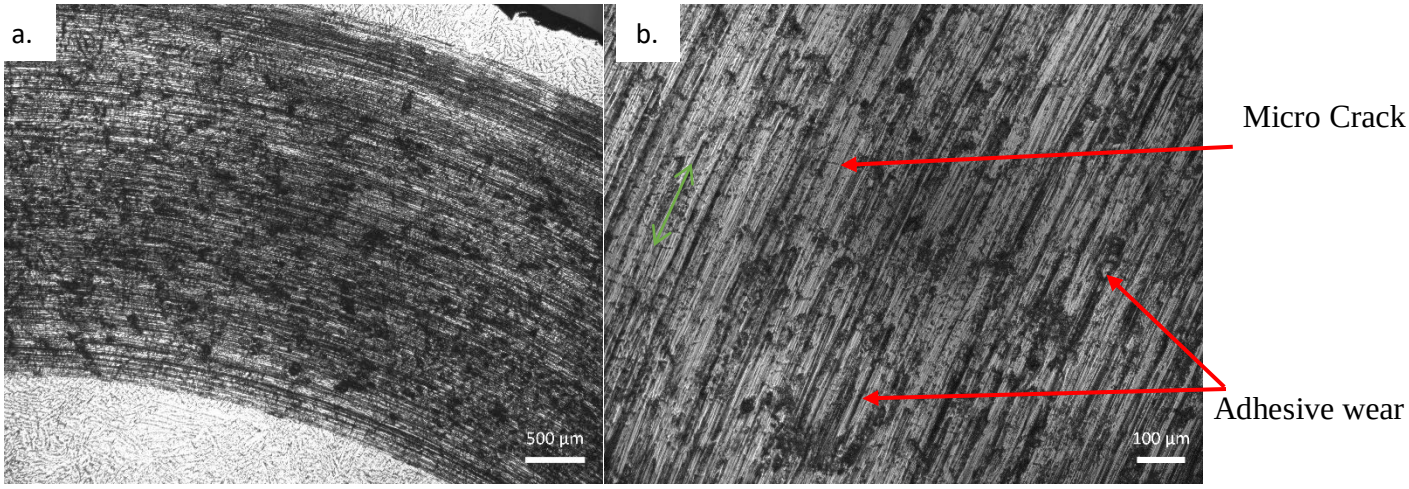

Figure 4.46 Wear mechanisms of the 3D Printed sample at AC200 condition

Fig 4.46. a shows an overview of the wear track for 3D printed AC200 sample. The wear track for this condition is not very deep. That is why the sample's surface can be seen in between some shallow grooves. Moreover, adhesive wear can also be seen on AC200 wear track.

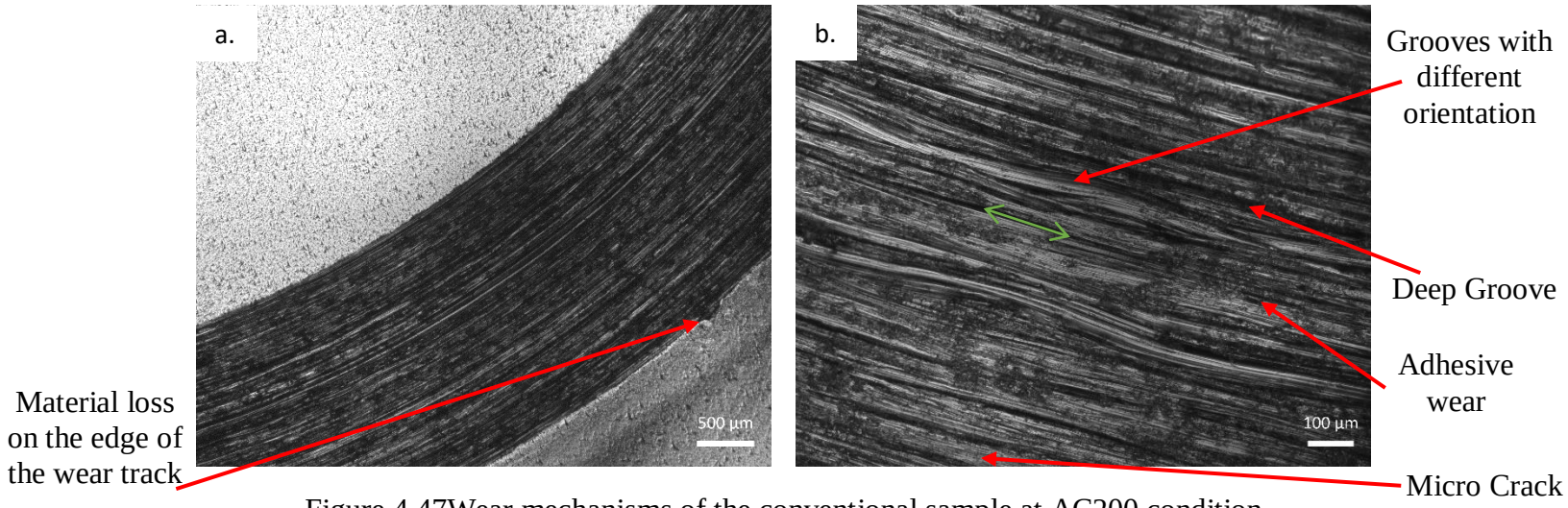

Figure 4.47Wear mechanisms of the conventional sample at AC200 condition

Wear mechanisms of conventional AC200 is described in fig 4.47. Fig 4.47.a is an overview of the round wear track. In the outer area of the wear track, some partial material loss can be observed. At a lower scale, significant wear mechanisms are observed (Fig 4.47 b). Abrasive, adhesive, and early-stage fatigue wear mechanisms are pointed in fig 4.47 b.

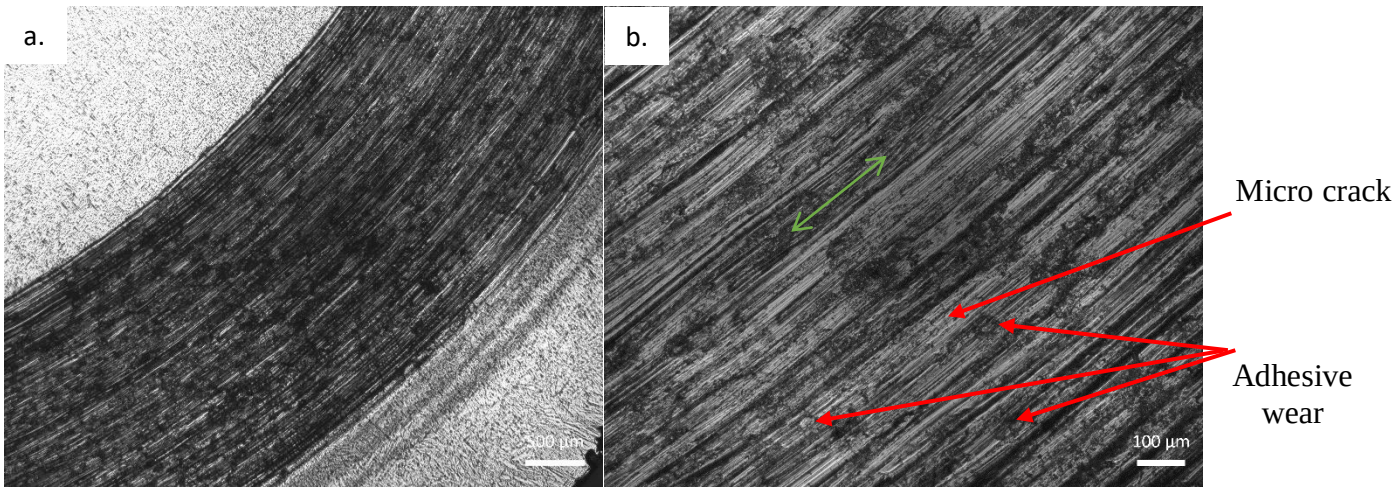

Figure 4.48Wear mechanisms of the 3D printed sample at AC500 condition

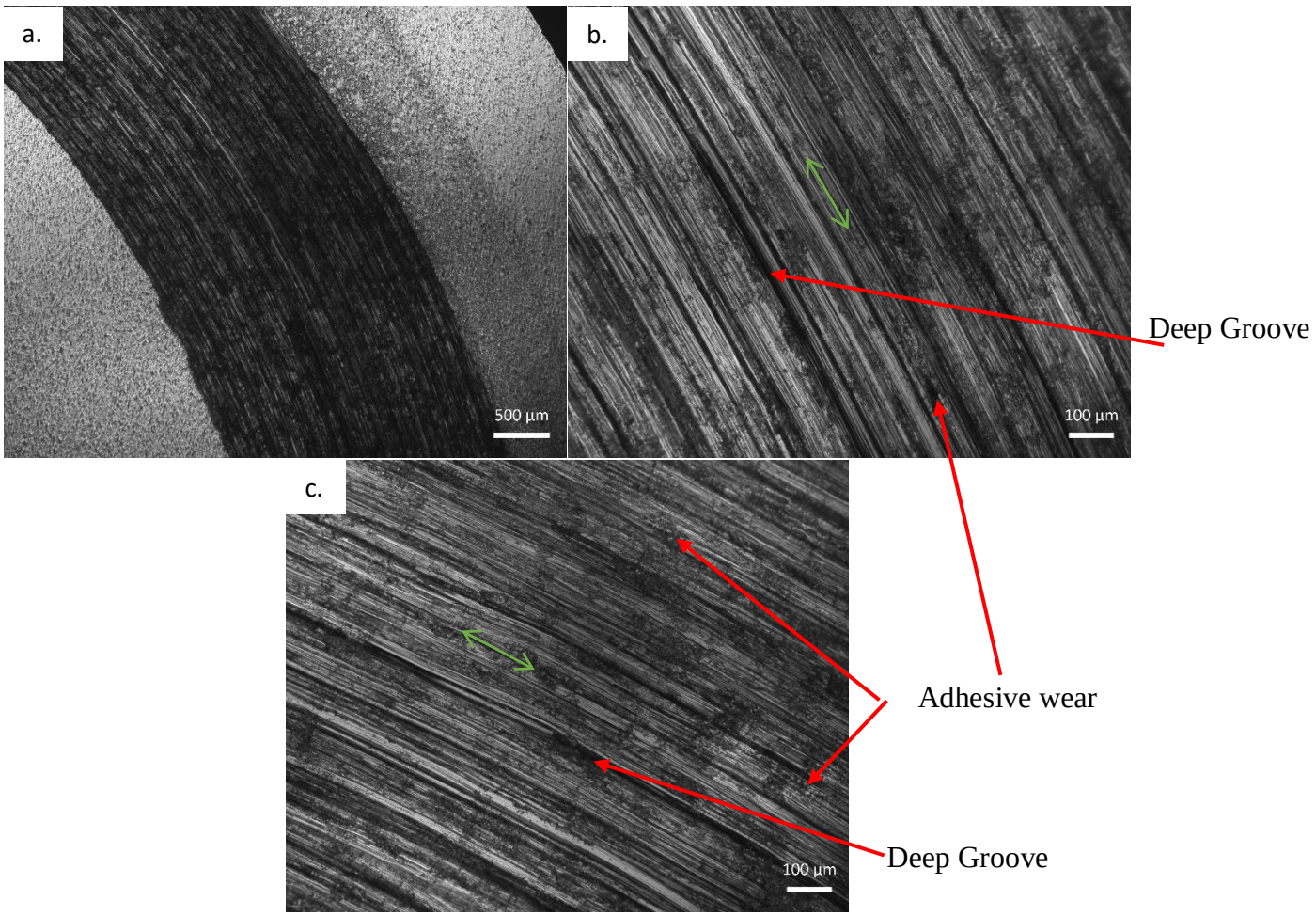

Figure 4.49 Wear mechanisms of the conventional sample at AC500 condition.

Micrographs shown in fig 4.48 and fig 4.49 are provided to describe the wear mechanisms observed in 3D printed and conventional manufactured AC500, respectively. Abrasive wear in the form of grooves with different depth, material loss due to adhesive wear and presence of microcrack due to tension and compression are three mechanisms in common in both conditions.

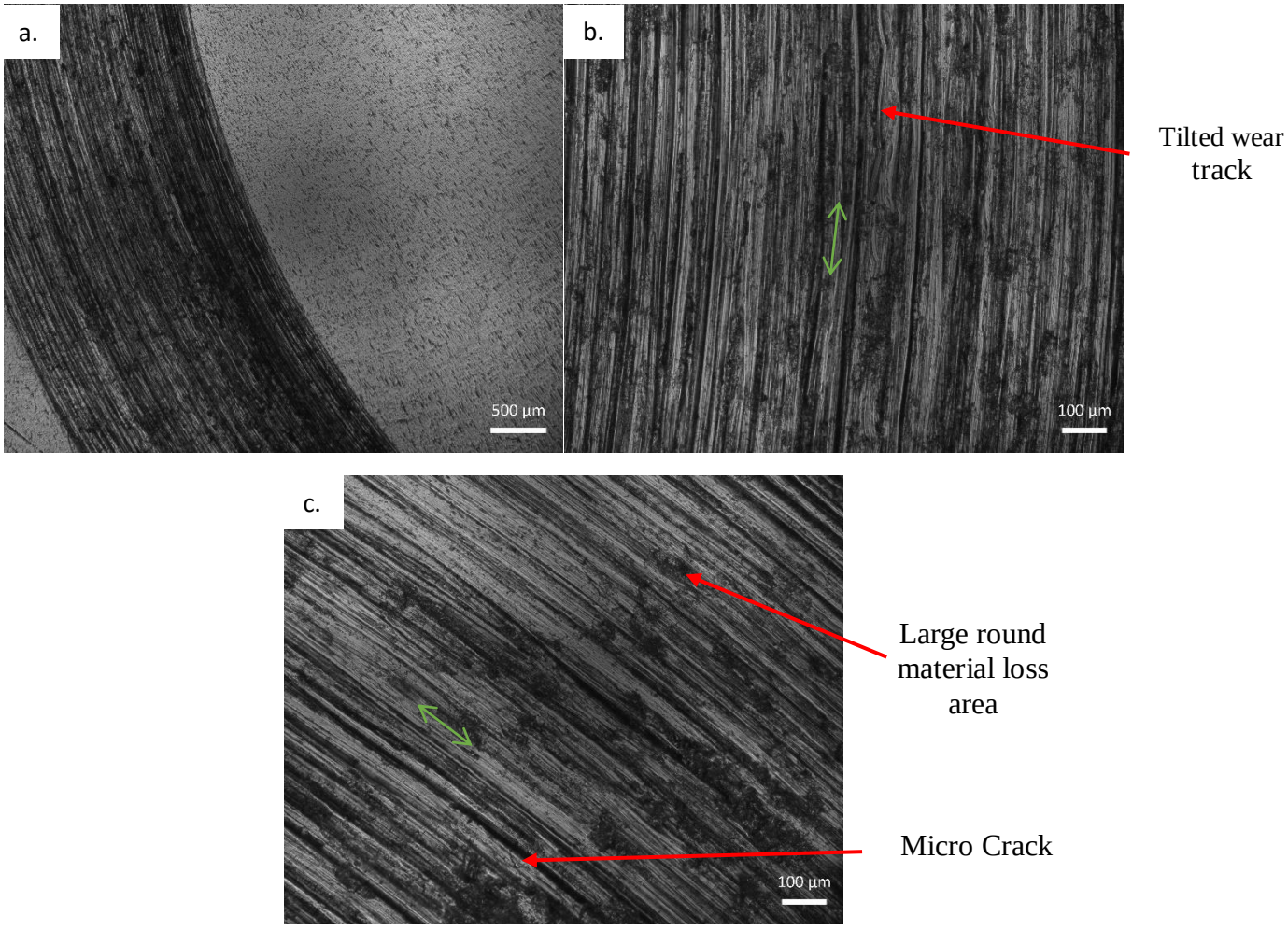

Figure 4.50Wear mechanisms of the 3D printed sample at AC800 condition

Micrographs in fig 4.50 describe the wear mechanisms found in 3D printed AC800 Ti6Al4V alloy. A tilted groove is observed in fig 4.50 b which appears as a result of third body abrasive wear. Besides the abrasive wear mechanism that is visible in all micrographs assigned to this condition, adhesive and microcracks are observed in fig 4.50 c.

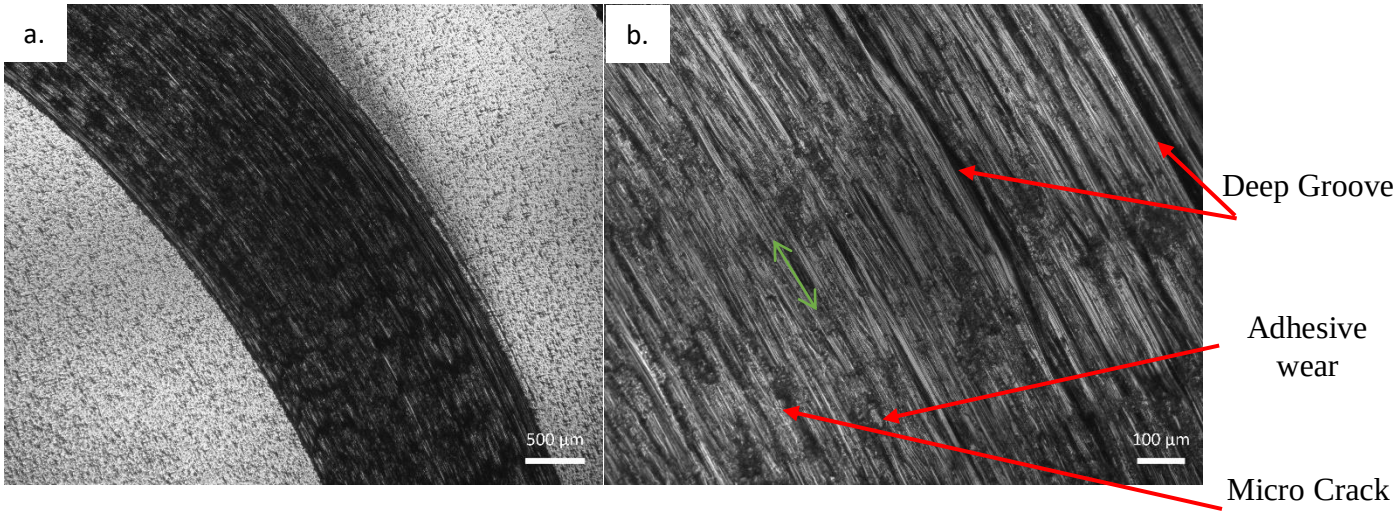

Figure 4.51 Wear mechanisms of the conventional sample at AC800 condition

Wear mechanisms of conventional AC800's wear track is shown in fig 4.51. Wear mechanisms described in this condition are abrasive wear with few deep grooves, fatigue wear initiated with microcracks, and adhesive wear. All these mechanisms are pointed in fig 4.51.b.

Therefore, based on all different wear mechanisms observed in each condition's wear track, adhesive wear is the only mechanism that has a direct connection with hardness. In other word, besides hardness, other factors such as surface roughness, material properties, and microstructure have effects on wear rate. In general, there were three different wear mechanisms found on each wear track which causes the mass loss in each condition. Fig 4.52 shows these three wear mechanisms, abrasive, adhesive, and fatigue wear that were found on wear tracks under Scanning Electron Microscope (SEM). Abrasive wear in the form of grooves with different depth can be seen in Fig 4.52.a. Abrasive wear can happen as a result of 2 body or 3 body wear. The microcrack is shown in Fig 4.52. b happened as a result of tension and compression zone formation on the wear track area. In this image, small debris is stuck in between the crack which may result in crack enlargement. Fig 4.52. c shows a large area of a material peels off which usually happens as a result of friction between two surfaces. Adhesive wear occurrence is dependable to material roughness, and basically, the roughness of one surface is becoming cold-welded to the second surface which is the reason behind the material transformation. It can be concluded that the hardness of the V-shaped structures results in a higher rate.

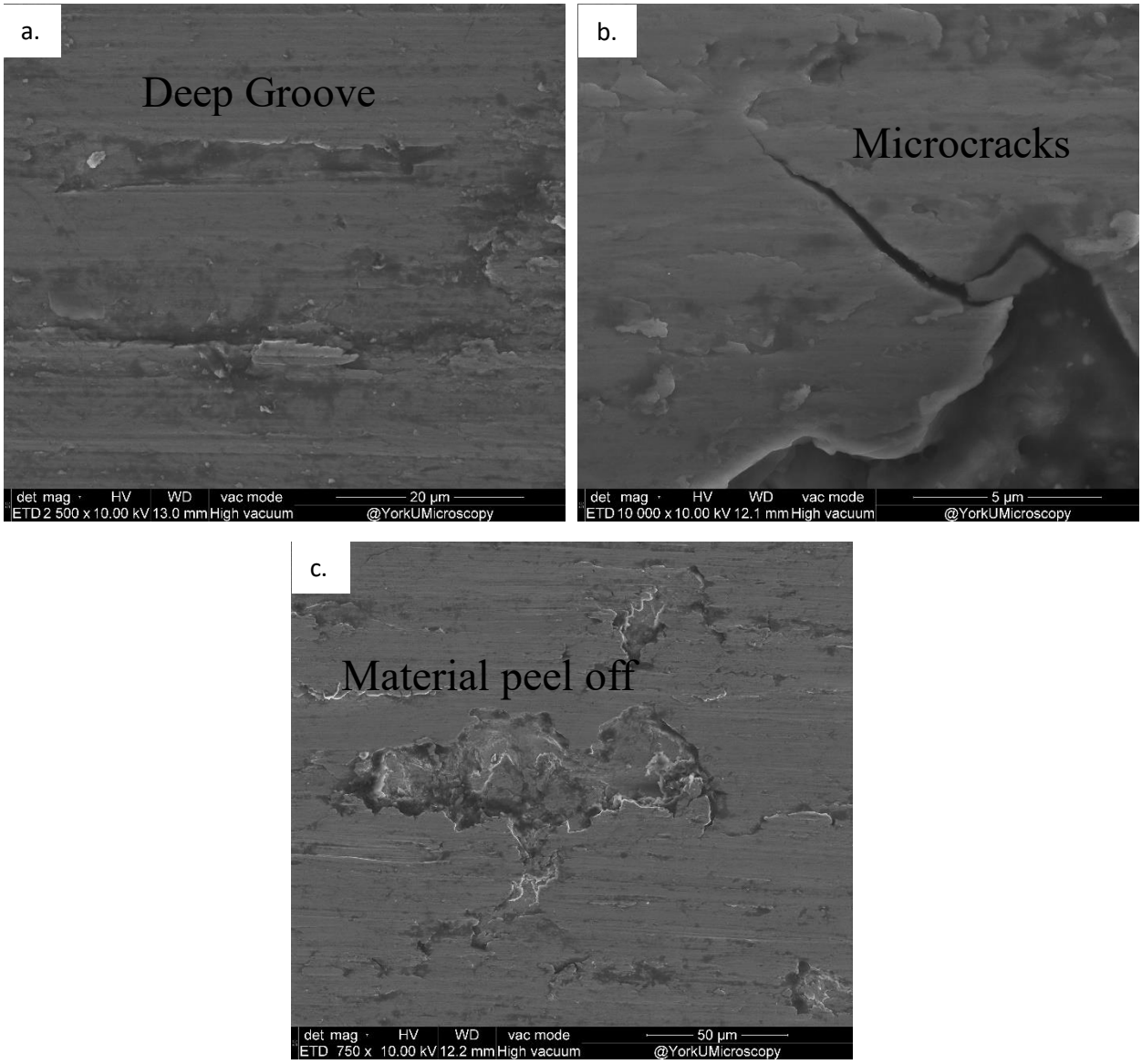

Figure 4.52 Three different wear mechanisms seen on the wear track a. Abrasive wear b. Fatigue wear c. Adhesive wear.

4.5 Chemical Composition and crystal structure analysis by EPMA and X-Ray

In the as printed specimen, the matrix was majorly Titanium with the spatial distribution of (Al, Ti, and V) particles as shown by the EPMA maps in Figures 4.53 to 4.57. After water quenching from solutionization at 1080℃, the structure comprised of lath structures emanating from prior beta grain boundaries in addition to the V-shaped structures. The prior beta grain boundary is rich in Al capable of forming Al-Ti intermetallic structure while the lath structures were rich in high Vanadium and some Titanium content. After aging to 500℃, the CV-WQ samples appeared to have a higher surface spread of the Al-Ti particles whereas the 3D samples exhibited localization and globalization of the intermetallic particles into the V-shaped structure which is of high Al content but depletion of V.

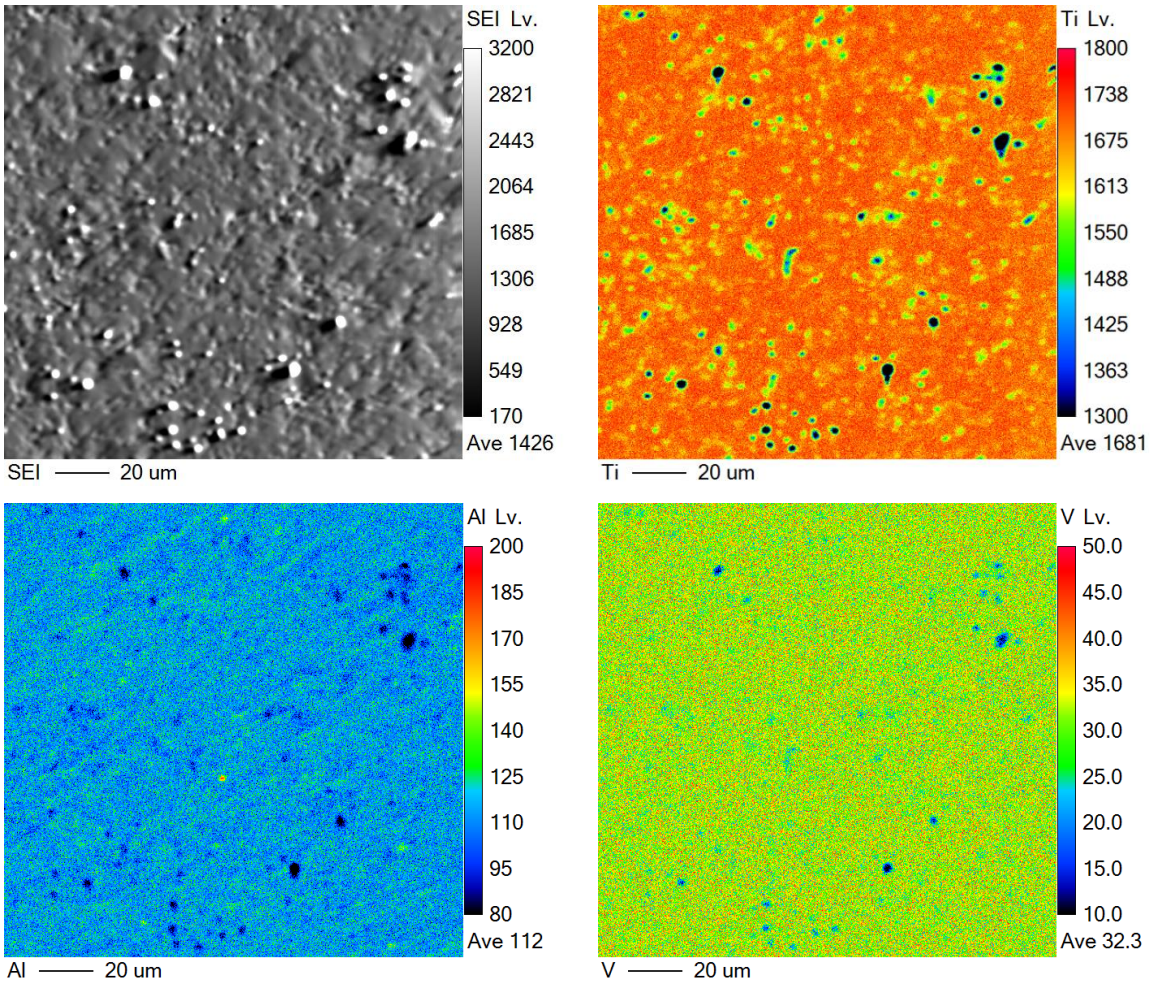

Figure 4.53 EPMA micrographs describe the Titanium, Aluminum, and Vanadium distribution in the As-Printed 3D Sample

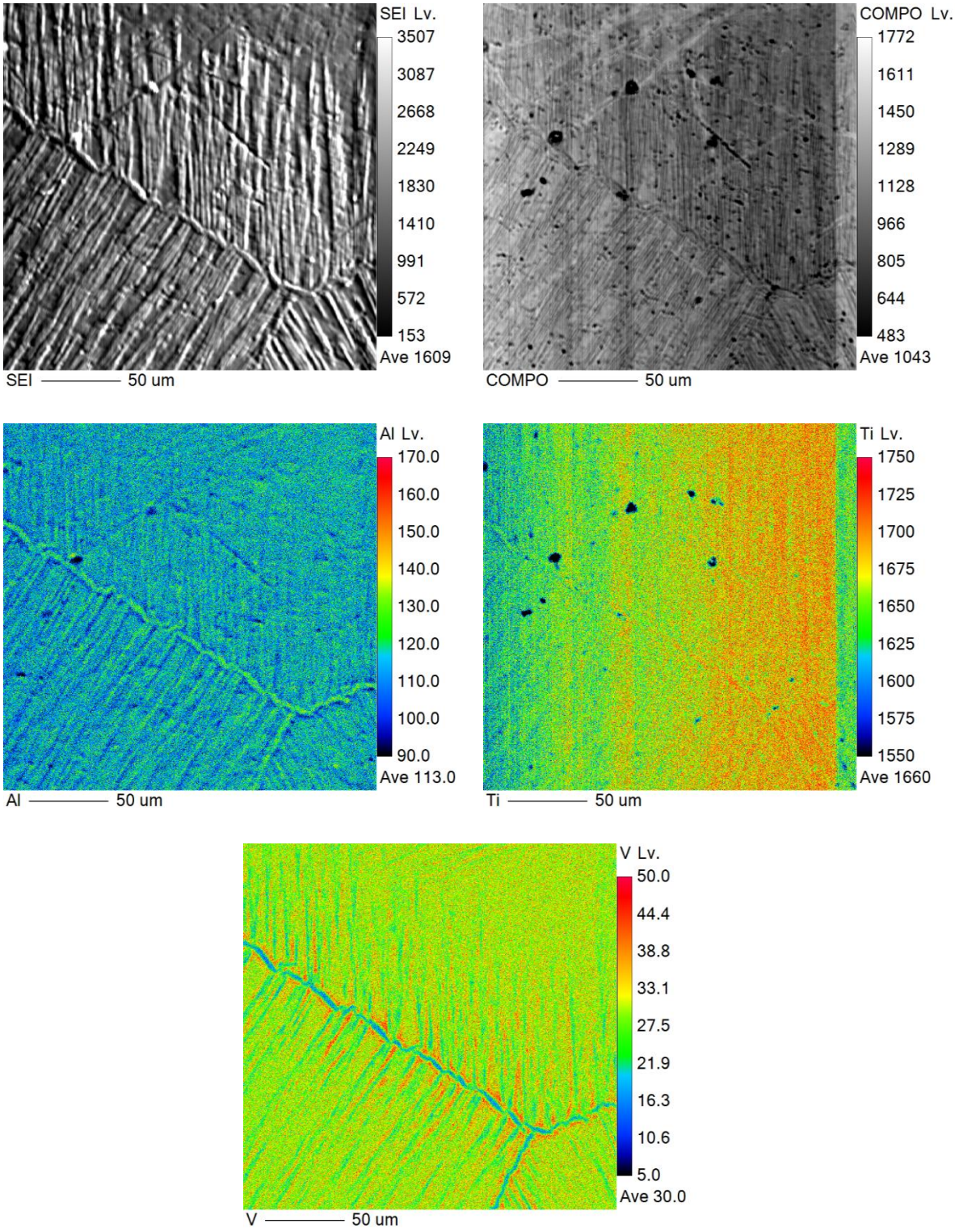

Figure 4.54 EPMA micrographs describe the Titanium, Aluminum, and Vanadium distribution in the WQ1080 CV Sample

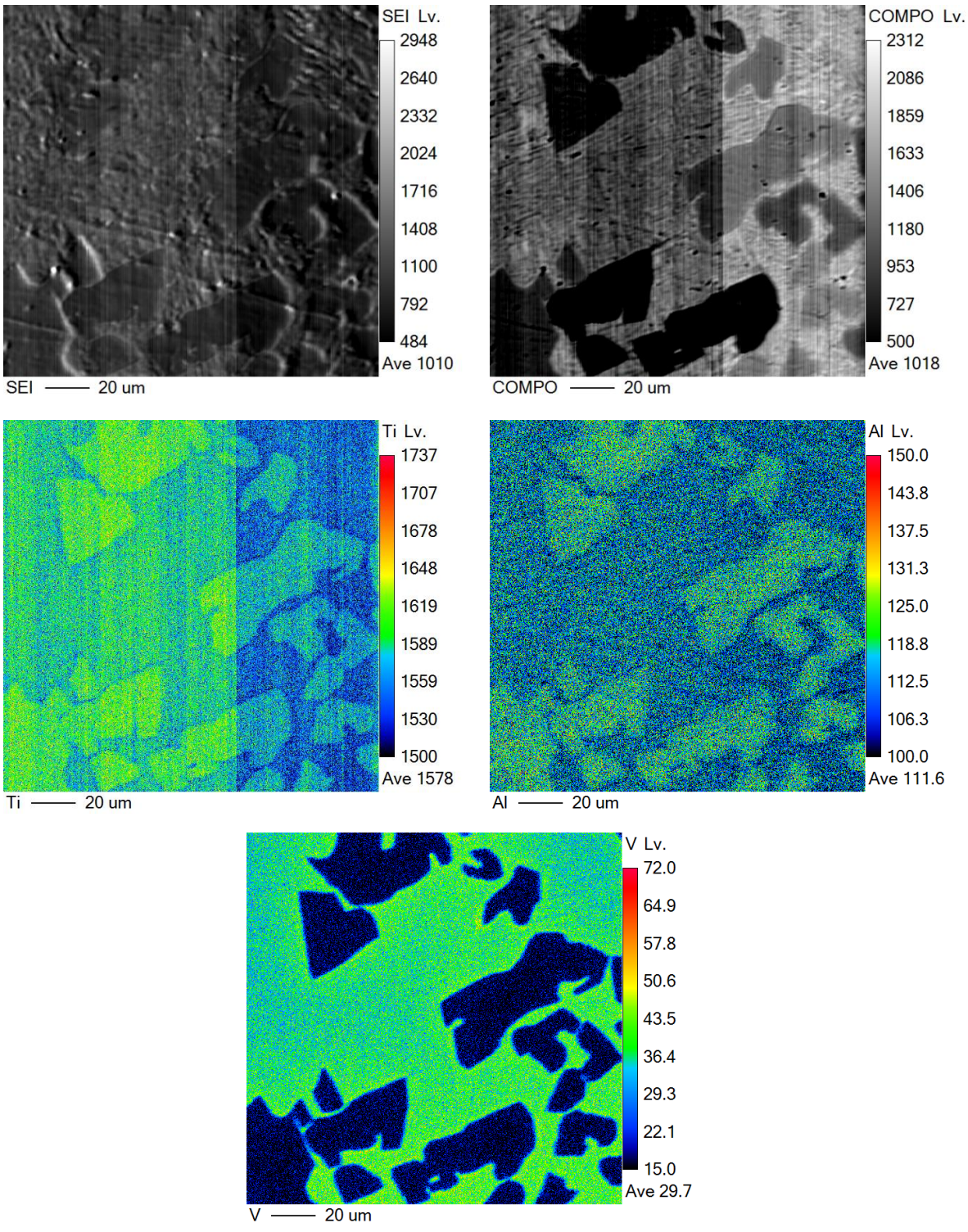

Figure 4.55 EPMA micrographs describe the Titanium, Aluminum, and Vanadium distribution in WQ1080 3D sample

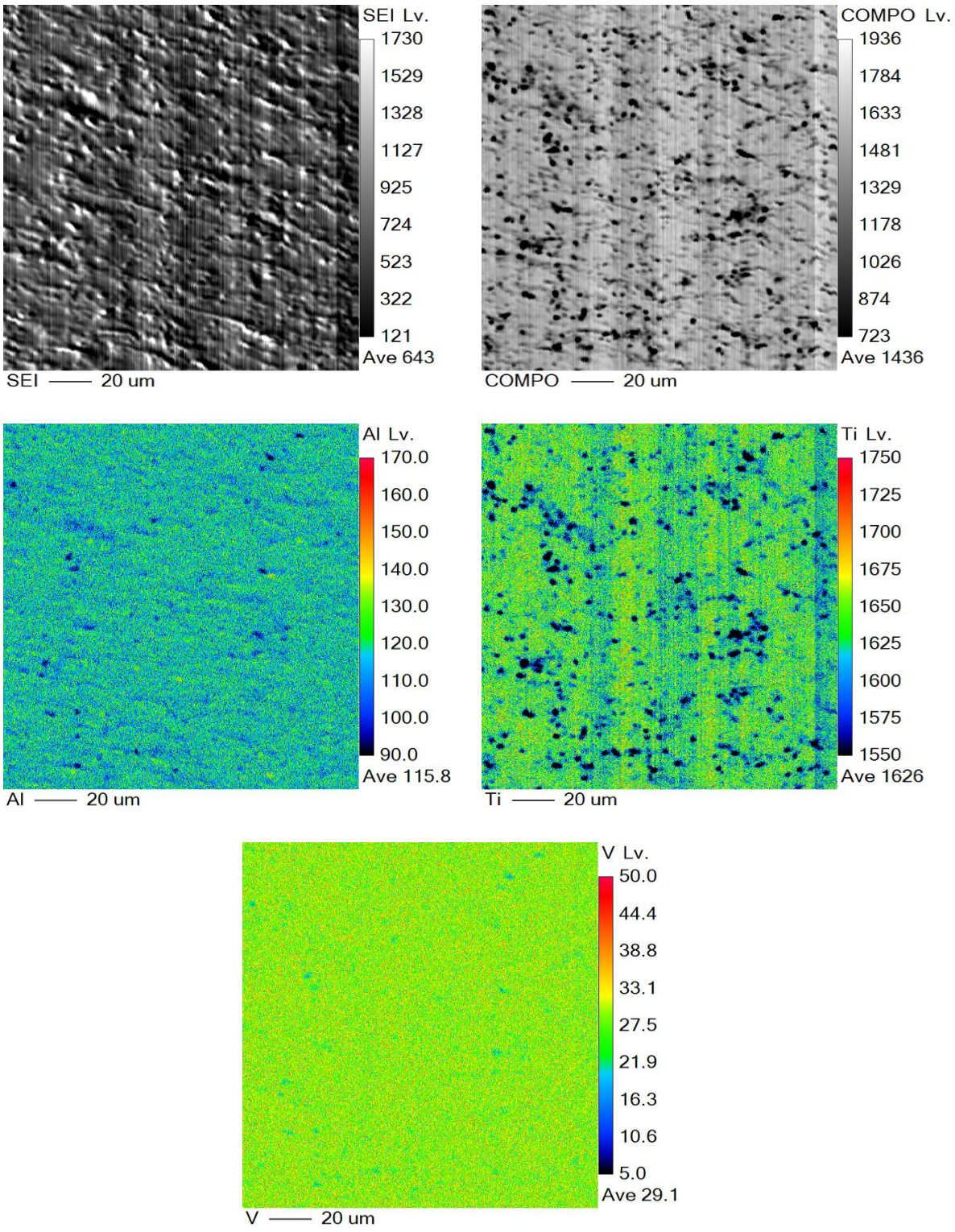

Figure 4.56 EPMA micrographs describe the Titanium, Aluminum, and Vanadium distribution in WQ500 CV Sample

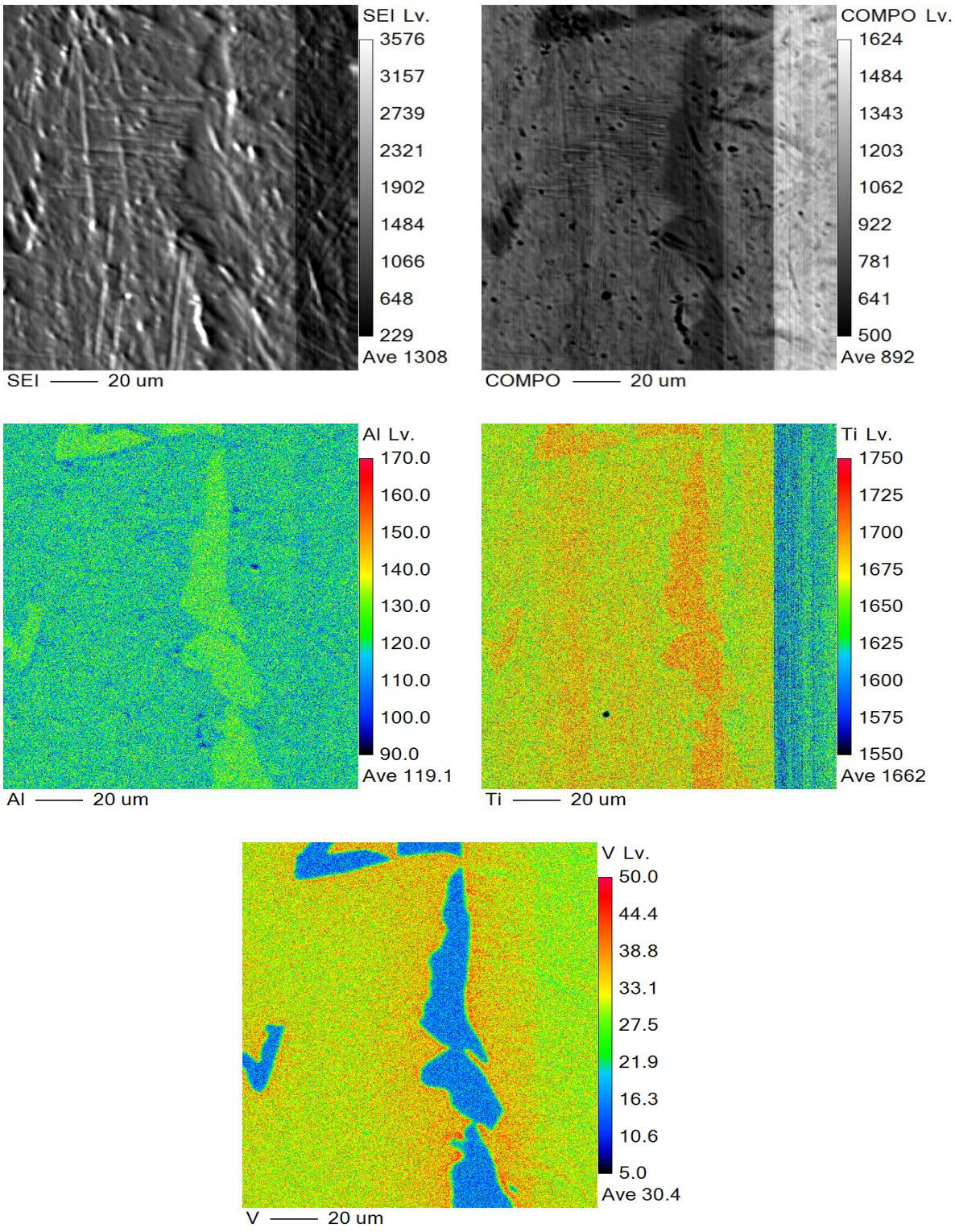

Figure 4.57 EPMA micrographs describe the Titanium, Aluminum, and Vanadium distribution in WQ500 3D Sample

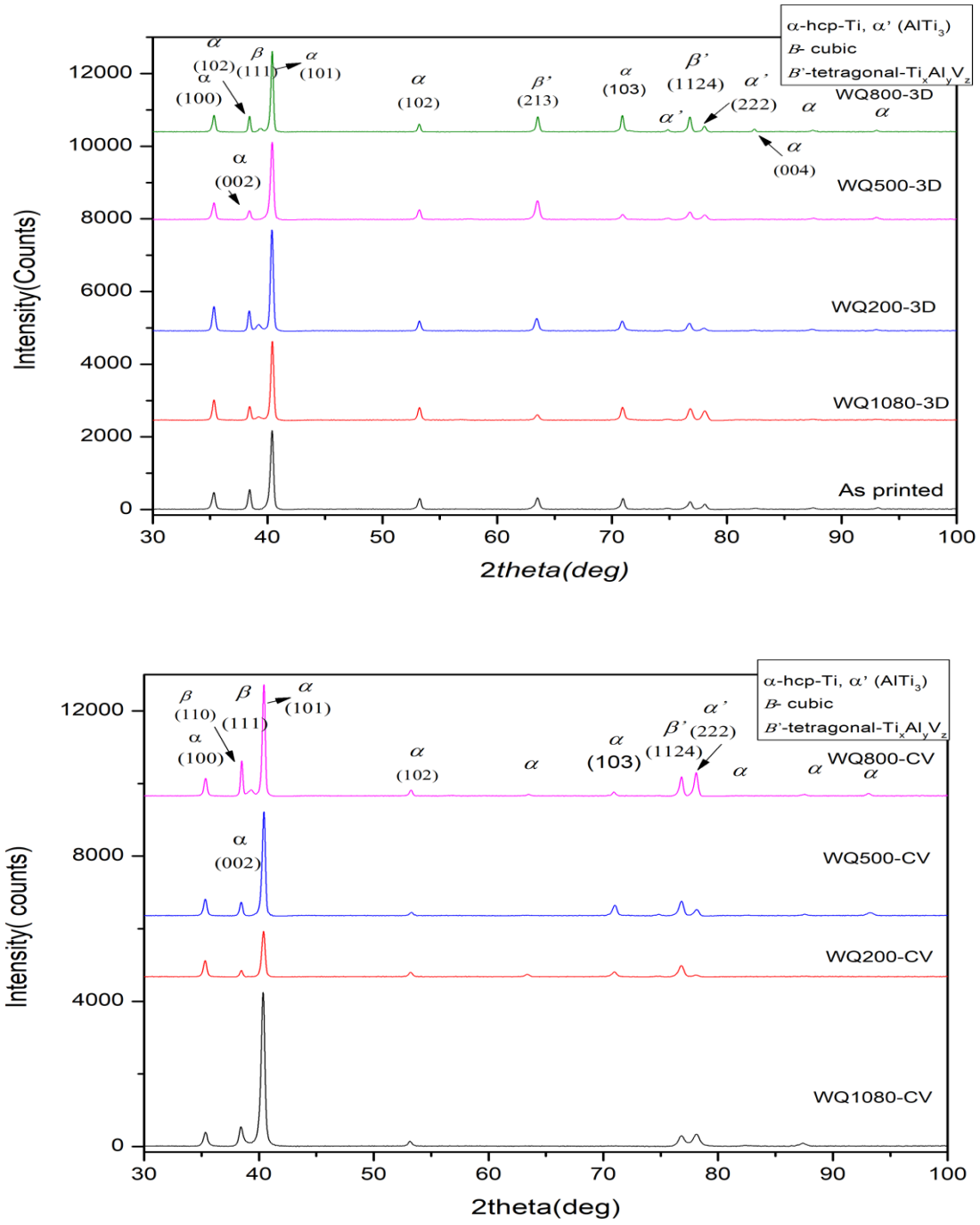

Figure 4.58 X-ray diffraction (XRD) analysis for water Quenched 3D printed and Conventional medical-grade Ti6Al4V

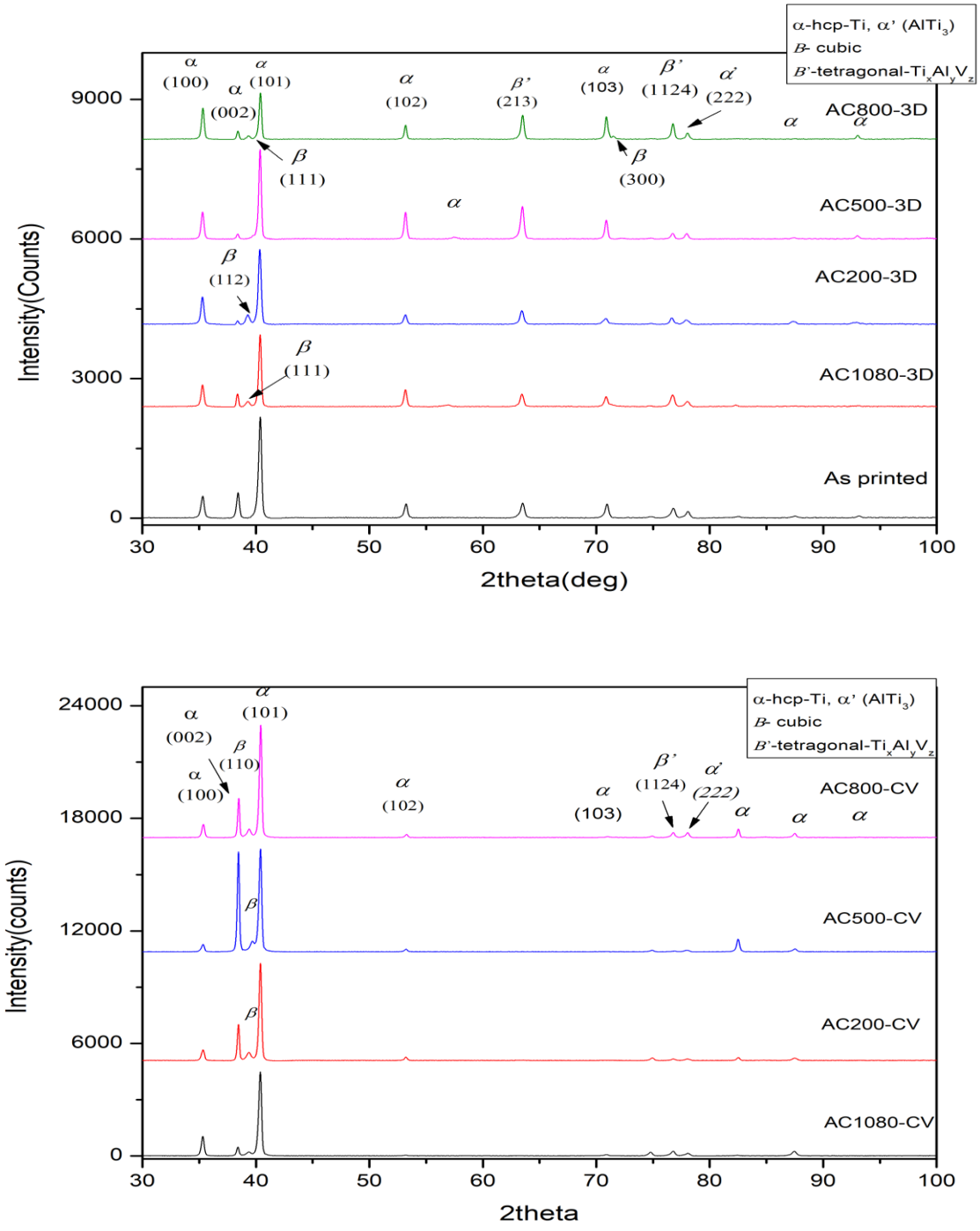

Figure 4.59 X-ray diffraction (XRD) analysis for Air-Cooled 3D printed and Conventional medical-grade Ti6Al4V

Figure 4.58 and Figure 4.59 show the X-ray diffraction (XRD) patterns of 3D printed and conventional specimens after heat treatment. In the conventional Ti6A4V alloy, XRD analysis shows that, after quenching to room temperature(RT) from the β solutionizing temperature (1080℃) and (α +β) aging (200-500)℃, the structure of the alloy is mostly consists of hcp α Ti phases at low angles with characteristic peak plane (101) occurring at diffraction angle (2θ) of 40.17 ^{o} with many subpeaks (100), (002), and (102). In addition, minor tetragonal prior-stable β phase (Al_9Ti_{23}) and hcp α' ($AlTi_3$) phases appeared at large angles of diffraction. In contrast, after air cooling, a small amount of retained cubic β phase is observed at 39.36 ^{o} (110) with suppression of the tetragonal phases as compared to the WQ samples. Generally, the intensity and sharpness of the water quenched specimen peaks were higher than the air-cooled specimens. Apart from the discontinuity at 500℃ aging, the intensity and sharpness of the characteristic α peak are mostly observed to decrease with a gradual increase in α to cubic β phase conversion at 39.215 ^{o} (110) and rise in the tetragonal phases at increasing aging temperatures. The highest intensity drops occurred after aging at 200℃ in both cooling media. After aging at 500℃, a significant increase in sharpness and intensity of α hcp characteristic peaks is observed from β → α transformation. Nonetheless, the WQ structure was enriched with cubic β phase only after aging at close to β transus temperature (800 ℃), with the emergence of extra α (103) hcp and increase in the volume fraction (intensity and sharpness) of tetragonal β' phases.

In the as printed material, the hcp α phase was also the prominently present occurring at (101) with many sub-peaks at (100), (102), (103) and α' (222)-$AlTi_3$ with any cubic β phase present. However, the emergence of additional tetragonal phases ($Al_3Ti_{0.8}V_{0.2}$ and Ti_9Al_{23}) at diffraction angles and planes of 63.5 ^{o}, (213) and 76.8, (1124), respectively were observed. The residual cubic β phase is observed after solutionizing at 1080 ℃ regardless of the cooling media. Air cooling led to higher cubic β phase formation compared to the water quenching. The level of conversion increased whereas the sharpness and intensity of α phase (101) are suppressed with increasing aging temperature in both cooling rates. But the α contents are more with sharper and intense peaks after water quenching than air-cooling. Nevertheless, like the conventional specimen, after aging at 500℃, the α characteristic peaks intensity was increased and turn out to be sharp with any cubic β phase. Heating to β transus (800 ℃), the reverse transformation of multiple retained cubic β phases (111) and a shoulder peak cubic β (300) are observed with drastic suppression of α (101)

peaks. In addition, the intensities of the α' (222)-$AlTi_3$ phase and the 2 tetragonal phases ($Al_3Ti_{0.8}V_{0.2}$ and Ti_9Al_{23}) increased gradually with increasing aging temperatures.

Chapter 5 Discussion

5.1 Microstructural Evolution of the 3D Printed and Heat-treated Ti6Al4V Alloy

Three main features were observed within the microstructures of the Ti6Al4V material employed in this study which were the lath, basketweave, and V-shaped structures. Toh et al. in their study observed α+β basket weave and colony structures in an as-printed electron beam melted Ti6Al4V and coarse β phase in as-cast samples [96]. The same microstructures can be seen in the as-printed sample manufactured by the DMLS technique (Direct Metal Laser Sintering). Prior to heat treatment, the 3D printed microstructure comprised mainly of the lath structures which were oriented parallel to one another in addition to basket-weave structures without any V-shaped structures. In addition, microstructural defects including some surface porosities were observed in the 3D printed samples.

Volume fractions and morphology of the lath, basketweave, and V-shaped structures are influenced by manufacturing methods, heating temperature, time, and cooling rate [97]. Generally, heat treatment of the as-printed materials leads to different microstructures with different properties [98], [99]. In the current study, all the samples were heated above the beta transus (1080℃) to form the β phase prior to water-quenching or air-cooling. After 3D printing, part of the as observed lath structures formed α colonies with different orientations whiles others were single-oriented and also formed the basket-weave lath structures. After water quenching, the α lath structures became very dense emanating from prior beta grain boundaries forming Widmanstätten colonies. Bracken's et al. in their study observed α lath structures that are formed from prior β grain in 3D printed Ti6Al4V after heating the sample to 1020℃ [100]. The basketweave structures after heat treatment became dense and globular within prior beta grains. In addition, heat-treating the samples led to the evolution of distinct, coalesced and coarsened V-shaped structures that were initially absent in the as-printed sample. On the other hand, the conventional samples had dense and coarse α colonies of lath structures after heat treatment with water quenching. After heat treatment at relatively higher temperatures, the dense and globular shaped basket weave structures evolved within the samples. Even though V-shaped structures were observed in the conventional samples after quenching, the V-shaped structures disappeared from the sample by being replaced with the basketweave structures, dense and globular structures. Y. Fan observed needle-like lath

structures as well as some semi-round shaped structures after water quenching Ti6Al4V right after heating to 1050℃ [101]. He also observed prior β phase boundaries transferring to α grain boundaries with basketweave structures forming after heating the sample to 1050℃ followed by air cooling.

Air-cooling after heat treatment of the 3D printed samples also resulted in precipitation of tiny α-lath structures from prior β grain. The α-lath structures orientation later became discontinuous lath structures without any basket weave structures present within the microstructure. In addition, coarse V-shaped structures evolved which later reduced in area fraction and become less distinct at higher aging temperatures. Also, the conventional Ti6Al4V samples treated at the same condition after air-cooling led to the formation of discontinuous α lath structures similar to those observed in the as-printed samples. However, these discontinuous α lath structures coalesce and coarsen to form spheroidized structures at relatively higher temperatures. The V-shaped and basketweave lath structures could rarely be observed within the microstructures after heat treating at elevated temperatures. Thus, manufacturing methods and cooling rates after heat treatment play a significant role in tailoring the microstructure of medical-grade Ti6Al4V material [97].

From the current study, it can be demonstrated that when the Ti6Al4V alloys are heated above the beta transus, the metastable β phase forms. During cooling, the boundaries of the metastable β phases begin to convert to α lath structures with a high degree of orientation as shown in Figure 5.1 (a) to (c). Increasing the aging temperature and/or time results in the growth of the α lath structures. The growth of the α lath structures consumes the prior β grain and grain boundaries which leads to the creation of the basketweave lath structures. Further continuous aging at elevated temperatures and or time results in the creation of the V-shaped structures, globular structures, and spheroids. It is inferred that the starting microstructure of the material, quenching or air-cooling, rate of diffusion, aging temperature and time have a significant effect on the microstructural features that evolve in the Ti6Al4V medical-grade titanium alloy regardless of the manufacturing process.

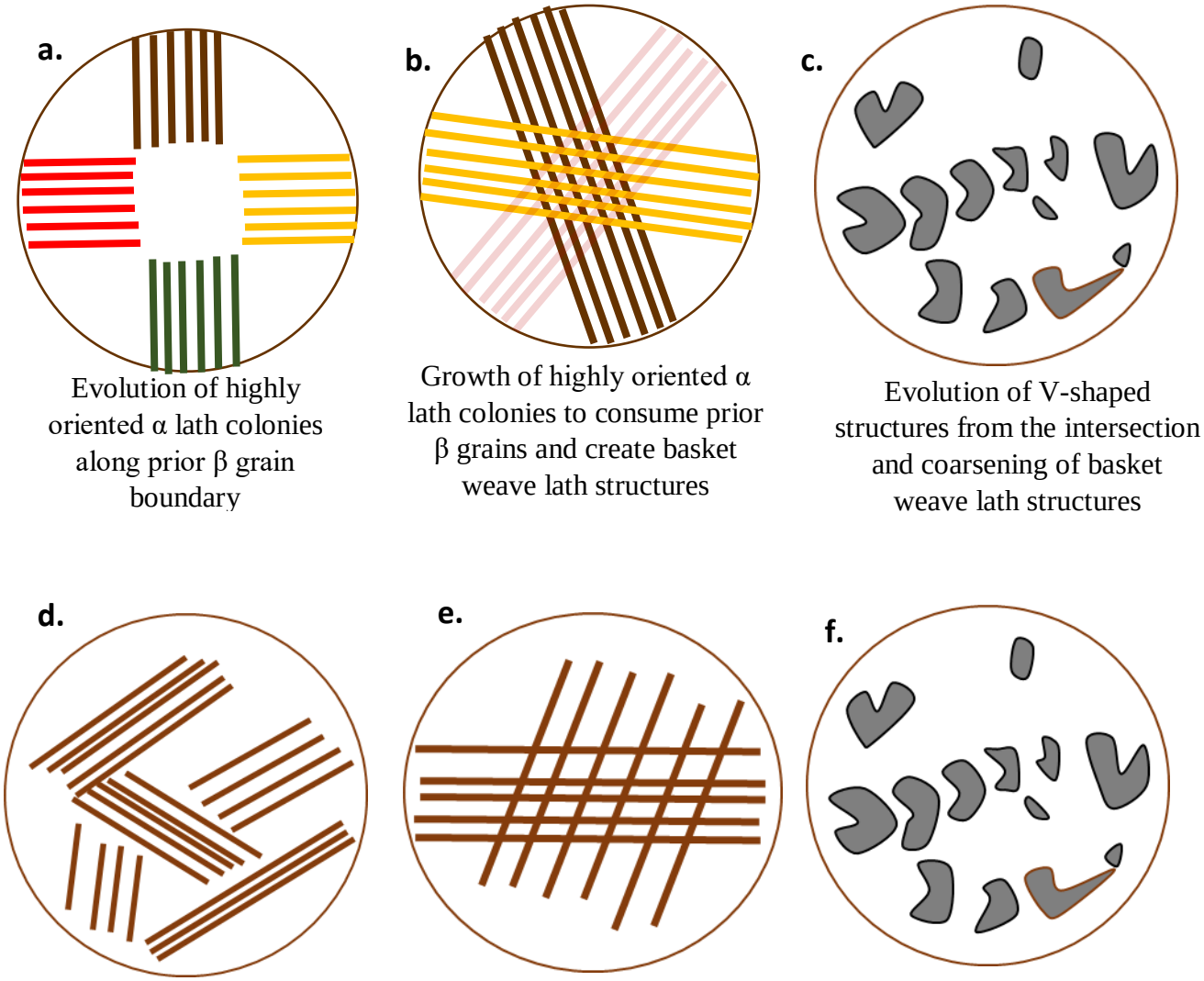

Figure 5.1 Schematics of different microstructural features visible on Ti6Al4V ELI. (a) – (c) evolution of the different microstructural features after cooling below the β transus. d. lath structures with varying hardness based on the depth, length, and density of the needle lath shapes. e. basket weave lath structures which have the lowest hardness value among all the other lath structures. f. V-shaped structure with the highest microhardness regardless of the heat treatment conditions or manufacturing process

5.2 Properties of the 3D Printed and Heat-treated Ti6Al4V Alloy

Strengthening in Ti6Al4V alloys occurs based on two mechanisms; solid solution phase transformation and precipitation hardening. But the desired strength is usually achieved by solutionization and aging heat treatments [6], [11]. Depending on the cooling rate from above the β transus, hardening types may vary. For instance, slow cooling Ti6Al4V from 1080°C (above β transus) to room temperature result in solid solution phase transformations that lead to hardening. Fast cooling methods like water quenching result in high dislocation density which causes hardening via dislocation strengthening [6], [11]. According to the effect of heat treatment on Ti6Al4V ELI alloys hardening, two different cooling rates and three different aging temperatures were chosen for this study. From the result, water quenched samples had the highest hardness values which are attributed to the creation of high densities of dislocations during quenching and the phase transformations. In the current study, it can be demonstrated that regardless of the starting microstructure of the material, quenching or air-cooling, diffusion process, aging temperature and time, the α lath, basketweave lath, globular and V-shaped structures had distinct properties. The globular and spheroidal structures had the lowest hardness followed by the basket weave lath and the α lath structures respectively (Figure 5.1 (d) to (f)). The V-shaped lath structures were always harder than all the other microstructural features. The decrease in hardness is attributed to the lack of V-shaped structures or the formation of globular structures and spheroids. Wear test result was reported in term of mass loss and coefficient friction (COF). Generally, the 3D printed samples had relatively higher wear resistance when compared with the 3D printed samples. R.Sahoo [102] and Emiliani and Brown [103] came up with a relation between hardness and wear rate in which wear rate decreases in Ti6Al4V alloys if the hardness increases. On the other hand, Naim and Bahadur [104]–[106] and Ambrosini and Bahadur [107] reported that by the increase in hardness, wear rate also increases. Toh [96] in his study on as-cast titanium and 3D printed Ti6Al4V alloys reported that the COF of the as-cast samples were always lower than the 3D printed samples. In this study, the conventional samples exhibited a lower coefficient of friction value compared to the 3D printed samples. This could be due to the formation of soft α lath structures which are single-oriented, emanating from prior β grain boundaries compared to the relatively hard and brittle V-shaped structures that were prominent in the 3D printed samples. Cvijovic [108] in his study on the effect of heat treatment on Ti6Al4V medical-grade titanium alloys, observed varying wear rate for this alloy after heat treatment which was attributed to the

varying and different microstructural features observed for the samples. It was reported that the presence of primary α lath structures improves the wear rate.

Another area that was investigated in this research was the chemical composition and crystal structure of the V-shaped structures as well as the grain boundaries in Ti6Al4V. The XRD data confirmed the presence of α and β phases in this alloy. The TiAl combination in this alloy was resulted to have a hexagonal closed packed crystal structure, while the TiV mixture was presented to have a body-centered cubic crystal structure. Results from the EPMA showed that V-shaped structures that had the highest hardness among all the other structures mostly consisted of titanium and aluminum. The same elements combination was found in grain boundaries which by comparing the result from the XRD, it can be concluded that the V-shaped structures had a hexagonal crystal structure. Moreover, the higher hardness of the V-shaped structures could be associated with the nucleation and globalization of Ti-Al intermetallic phases forming within the crystal. H.Galarraga et al [109] also confirmed a hexagonal structure for a grain boundary in an as printed samples's grain boundary.

5.3 Application of the Current Results in Tailoring and Designing Microstructures that are Better for Implant Industry

The microstructure of Ti6Al4V is dependent on the manufacturing techniques, the microstructure prior to post-processing, and the aging temperature. There were three major structures noticed in this study which were basketweave, lath, and V-shaped structures. V-shaped structures were mostly seen in 3D printed samples which got to their highest volume fraction when they were aged at 500℃. Even though, globulazation mostly happened in the conventional samples. The current study showed that the presence of the V-shaped structures resulted in high hardness. Thus, for applications that a high hardness is required, the presence of these V-shaped microstructures can be beneficial. Additionally, it can be concluded from this study's result that the aging process for the 3D printed implant is not necessary. The properties of the as printed sample were close to the aged sample. Therefore, the complication and the cost of the post-processing (aging) can be eliminated.

The knowledge and understanding from this study can be used to tailor the microstructure and properties of 3D printed Ti6Al4V in different applications. Moreover, the results from this work

can be used to validate computer modelings used to estimate the effect of heat treating on the microstructure and properties of this alloy.

Chapter 6 Conclusion and Future Work

6.1 Conclusion Remarks

The current study was on the effect of post-processing heat treatment on microstructure and mechanical properties of medical-grade Ti6Al4V alloy. This investigation was done to characterize the integrity and performance of the as printed alloy and possibly optimizing the microstructure and improving properties of 3D printed Ti6Al4V alloy by post-processing heat treatment. A summary of the findings is provided below:

1. The microstructure observed in the as printed Ti6Al4V ELI mainly consisted of α lath structures with a high degree of orientation and basketweave structures. Some linear micropores were also observed in the additive manufactured sample prior to heat treatment.
2. It was inferred that heat treatment parameters such as cooling rate and temperature had a significant effect on the size, geometry, spatial distribution and properties of the three main structures; V-shaped, lath, and basket weave.
3. Microstructural evolution of medical-grade Ti6Al4V alloy during heat treatment was influenced by the starting microstructure of the sample, the cooling rate, aging temperature, and duration regardless of the manufacturing process.
4. Solution treatment in both manufacturing techniques improved the microhardness. Although, water quenched samples, in general, had higher hardness compared to the air-cooled ones. Aging at 500℃ for both air-cooled and water quenched 3D printed samples resulted in the highest microhardness due to the presence of V-shaped structures. Regardless of the heat-treating condition, among all observed structures, V-shaped had the highest hardness, while basket weave had the lowest hardness followed by the α lath structures which is due to the different crystal structures and morphologies.
5. Wear rate was influenced by material hardness, properties, surface roughness, and microstructure and each of them individually may result in different wear mechanisms.
6. 3D printed Ti6Al4V ELI alloy had higher wear resistance compared to conventional Ti6Al4V ELI alloy. Also, it was observed that the conventional samples exhibited a lower coefficient of friction than the 3D printed specimens. In addition, better wear rate was obtained by air-cooled samples than water quenched prior to the aging process.

7. Based on the EPMA and XRD results, V-shaped structures and grains boundaries have a hexagonal closed pack (HCP) crystal structure.

6.2 Future Direction

This research was mainly focused on the effect of heat treatment on the microstructural evolution of 3D printed and conventional medical-grade Ti6Al4V alloy and the possible effect of microstructure and manufacturing techniques on properties of this alloy. In the future, observing microstructural evolution during the heat treatment procedure can lead to a better understanding of the phase transformation. Also, other post-processing techniques need to be investigated and possibly compared to the heat treatment results from this study. In addition, a detailed study can be done on the morphology of the V-shaped structure in different heat treatment conditions by TEM.

References

[1] R. Singh, S. Singh, and M. S. J. Hashmi, “Implant Materials and Their Processing Technologies,” in *Reference Module in Materials Science and Materials Engineering*, 2016.

[2] M. J. Donachie, *Titanium: A Technical Guide, 2nd Edition*. 2000.

[3] D. F. Williams, “Titanium for Medical Applications,” 2001.

[4] S. L. Semiatin, V. Seetharaman, and I. Weiss, “The thermomechanical processing of alpha/beta titanium alloys,” *JOM*. 1997.

[5] R. Huang *et al.*, “Energy and emissions saving potential of additive manufacturing: the case of lightweight aircraft components,” *J. Clean. Prod.*, 2016.

[6] G. Lutjering and J. C. Williams, “Titanium - 2nd Edition,” *Engineering*, 2007.

[7] A. Molinari, G. Straffelini, B. Tesi, and T. Bacci, “Dry sliding wear mechanisms of the Ti6A14V alloy,” *Wear*, 1997.

[8] I. Y. Kim, B. J. Choi, Y. J. Kim, and Y. Z. Lee, “Friction and wear behavior of titanium matrix (TiB+TiC) composites,” *Wear*, 2011.

[9] H. Attar *et al.*, “Nanoindentation and wear properties of Ti and Ti-TiB composite materials produced by selective laser melting,” *Mater. Sci. Eng. A*, 2017.

[10] S. Yerramareddy and S. Bahadur, “Effect of operational variables, microstructure and mechanical properties on the erosion of Ti-6Al-4V,” *Wear*, 1991.

[11] J. Donachie and J. M, “Titanium – A Technical Guide,” *ASM Int. 2nd Ed.*, 2000.

[12] Y. M. Ahmed, K. Sahari, and M. Ishak, “Welding of Titanium (Ti-6Al-4V) Alloys: A Review,” 2012.

[13] M. Donachie, *Titanium: A Technical Guide, 2nd Edition*. 1988.

[14] D. H. and A. W. Pense, *Structure and properties of engineering materials*, Fifth. Mc Graw Hill publication, 2002.

[15] M. Niinomi and M. Nakai, “Ti-Based Biomedical Alloys,” 2019, pp. 61–76.

[16] I. Inagaki, T. Takechi, S. Yoshihisa, and A. Nozomu, “Application and Features of Titanium for the Aerospace Industry[J],” *Nippon Steel & Sumitomo Metal Technical Report*. 2014.

[17] R. R. Boyer, “An overview on the use of titanium in the aerospace industry,” *Mater. Sci. Eng. A*, 1996.

[18] P. Singh, H. Pungotra, and N. S. Kalsi, “On the characteristics of titanium alloys for the aircraft applications,” in *Materials Today: Proceedings*, 2017.

[19] E. Uhlmann, R. Kersting, T. B. Klein, M. F. Cruz, and A. V. Borille, “Additive Manufacturing of Titanium Alloy for Aircraft Components,” in *Procedia CIRP*, 2015.

[20] L. Ciocca, M. Fantini, F. De Crescenzio, G. Corinaldesi, and R. Scotti, “Direct metal laser sintering (DMLS) of a customized titanium mesh for prosthetically guided bone regeneration of atrophic maxillary arches,” *Med. Biol. Eng. Comput.*, 2011.

[21] W. E. Garrett *et al.*, “American Board of Orthopaedic Surgery practice of the orthopaedic surgeon: Part-II, certification examination case mix,” *J. Bone Jt. Surg. - Ser. A*, 2006.

[22] C. L. Thomas, T. M. Gaffney, S. Kaza, and C. H. Lee, “Rapid prototyping of large scale aerospace structures,” in *IEEE Aerospace Applications Conference Proceedings*, 1996.

[23] “Rapid prototyping & manufacturing— Fundamentals of stereolithography,” *J. Manuf.*

Syst., 1993.

[24] N. A. Waterman and P. Dickens, “Rapid product development in the USA, Europe and Japan,” *World Cl. Des. to Manuf.*, 1994.

[25] Y. Song, Y. Yan, R. Zhang, D. Xu, and F. Wang, “Manufacture of the die of an automobile deck part based on rapid prototyping and rapid tooling technology,” *J. Mater. Process. Technol.*, 2002.

[26] E. Sachlos, J. T. Czernuszka, S. Gogolewski, and M. Dalby, “Making tissue engineering scaffolds work. Review on the application ofsolid freeform fabrication technology to the production of tissue engineeringscaffolds,” *European Cells and Materials*. 2003.

[27] J. Giannatsis and V. Dedoussis, “Additive fabrication technologies applied to medicine and health care: A review,” *Int. J. Adv. Manuf. Technol.*, 2009.

[28] N. Guo and M. C. Leu, “Additive manufacturing: Technology, applications and research needs,” *Frontiers of Mechanical Engineering*. 2013.

[29] S. Kumar, “Selective Laser Sintering: A Qualitative and Objective Approach,” *JOM*. 2003.

[30] G. N. Levy, R. Schindel, and J. P. Kruth, “Rapid manufacturing and rapid tooling with layer manufacturing (LM) technologies, state of the art and future perspectives,” *CIRP Ann. - Manuf. Technol.*, 2003.

[31] J. P. Kruth, L. Froyen, J. Van Vaerenbergh, P. Mercelis, M. Rombouts, and B. Lauwers, “Selective laser melting of iron-based powder,” in *Journal of Materials Processing Technology*, 2004.

[32] F. Abe, K. Osakada, M. Shiomi, K. Uematsu, and M. Matsumoto, “The manufacturing of hard tools from metallic powders by selective laser melting,” *J. Mater. Process. Technol.*, 2001.

[33] L. Lu, J. Y. H. Fuh, Z. D. Chen, C. C. Leong, and Y. S. Wong, “In situ formation of TiC

composite using selective laser melting," *Mater. Res. Bull.*, 2000.

[34] K. Osakada and M. Shiomi, "Flexible manufacturing of metallic products by selective laser melting of powder," *Int. J. Mach. Tools Manuf.*, 2006.

[35] J. P. Kruth, P. Mercelis, J. Van Vaerenbergh, L. Froyen, and M. Rombouts, "Binding mechanisms in selective laser sintering and selective laser melting," *Rapid Prototyping Journal*. 2005.

[36] "eoc." [Online]. Available: https://www.eos.info/en.

[37] D. Cormier, O. Harrysson, and H. West, "Characterization of H13 steel produced via electron beam melting," in *Rapid Prototyping Journal*, 2004.

[38] P. Heinl, A. Rottmair, C. Körner, and R. F. Singer, "Cellular titanium by selective electron beam melting," *Adv. Eng. Mater.*, 2007.

[39] L. E. Rannar, A. Glad, and C. G. Gustafson, "Efficient cooling with tool inserts manufactured by electron beam melting," *Rapid Prototyp. J.*, 2007.

[40] O. L. A. Harrysson, O. Cansizoglu, D. J. Marcellin-Little, D. R. Cormier, and H. A. West, "Direct metal fabrication of titanium implants with tailored materials and mechanical properties using electron beam melting technology," *Mater. Sci. Eng. C*, 2008.

[41] D. Cormier, H. West, O. Harrysson, and K. Knowlson, "Characterization of thin walled Ti-6Al-4V components produced via electron beam melting," *Solid Free. Fabr. Symp.*, 2004.

[42] P. Heinl, L. Müller, C. Körner, R. F. Singer, and F. A. Müller, "Cellular Ti-6Al-4V structures with interconnected macro porosity for bone implants fabricated by selective electron beam melting," *Acta Biomater.*, 2008.

[43] A. Gasser, G. Backes, I. Kelbassa, A. Weisheit, and K. Wissenbach, "Laser Additive Manufacturing: Laser Metal Deposition (LMD) and Selective Laser Melting (SLM) in Turbo-Engine Applications," *Laser Tech. J.*, 2010.

[44] V. K. Balla, P. D. DeVasConCellos, W. Xue, S. Bose, and A. Bandyopadhyay, "Fabrication of compositionally and structurally graded Ti-TiO2 structures using laser engineered net shaping (LENS)," *Acta Biomater.*, 2009.

[45] G. K. Lewis and E. Schlienger, "Practical considerations and capabilities for laser assisted direct metal deposition," *Mater. Des.*, 2000.

[46] K. Zhang, W. Liu, and X. Shang, "Research on the processing experiments of laser metal deposition shaping," *Opt. Laser Technol.*, 2007.

[47] G. K. Lewis and P. Lyons, "Direct laser metal deposition process fabricates near-net-shape components rapidly," *Mater. Technol.*, 1995.

[48] W. Hofmeister, M. Griffith, M. Ensz, and J. Smugeresky, "Solidification in direct metal deposition by LENS processing," *JOM*, 2001.

[49] J. Sedlak, D. Rican, M. Piska, and L. Rozkosny, "Study of materials produced by powder metallurgy using classical and modern additive laser technology," in *Procedia Engineering*, 2015.

[50] M. Agarwala, D. Bourell, J. Beaman, H. Marcus, and J. Barlow, "Direct selective laser sintering of metals," *Rapid Prototyp. J.*, 1995.

[51] M. Agarwala, D. Bourell, J. Beaman, H. Marcus, and J. Barlow, "Post-processing of selective laser sintered metal parts," *Rapid Prototyp. J.*, 1995.

[52] J. P. Kruth, G. Levy, F. Klocke, and T. H. C. Childs, "Consolidation phenomena in laser and powder-bed based layered manufacturing," *CIRP Ann. - Manuf. Technol.*, 2007.

[53] J. Kruth, B. Vandenbroucke, J. Vaerenbergh, and P. Mercelis, "Benchmarking of different SLS/SLM processes as rapid manufacturing techniques," in *Int. Conf. Polymers & Moulds Innovations (PMI), Gent, Belgium, April 20-23, 2005*, 2005.

[54] R. Chang, K. Emami, H. Wu, and W. Sun, "Biofabrication of a three-dimensional liver micro-organ as an in vitro drug metabolism model," *Biofabrication*, 2010.

[55] “Adler Ortho Group.” [Online]. Available: http://www.alaortho.com/indBigEng.htm. Accessed in 2010.

[56] “Arcam A B.” [Online]. Available: http://www.arcam.com.

[57] B. Vandenbroucke and J. P. Kruth, “Selective laser melting of biocompatible metals for rapid manufacturing of medical parts,” in *17th Solid Freeform Fabrication Symposium, SFF 2006*, 2006.

[58] J. D. Avila, S. Bose, and A. Bandyopadhyay, “Additive manufacturing of titanium and titanium alloys for biomedical applications,” in *Titanium in Medical and Dental Applications*, 2018.

[59] Y. L. Hao, S. J. Li, and R. Yang, “Biomedical titanium alloys and their additive manufacturing,” *Rare Metals*. 2016.

[60] D. A. Hollander *et al.*, “Structural, mechanical and in vitro characterization of individually structured Ti-6Al-4V produced by direct laser forming,” *Biomaterials*, 2006.

[61] E. Sallica-Leva, A. L. Jardini, and J. B. Fogagnolo, “Microstructure and mechanical behavior of porous Ti-6Al-4V parts obtained by selective laser melting,” *J. Mech. Behav. Biomed. Mater.*, 2013.

[62] V. K. Balla *et al.*, “Quasi-static torsional deformation behavior of porous Ti6Al4V alloy,” *Mater. Sci. Eng. C*, 2011.

[63] T. Vilaro, C. Colin, and J. D. Bartout, “As-fabricated and heat-treated microstructures of the Ti-6Al-4V alloy processed by selective laser melting,” *Metall. Mater. Trans. A Phys. Metall. Mater. Sci.*, 2011.

[64] P. H. Li, W. G. Guo, W. D. Huang, Y. Su, X. Lin, and K. B. Yuan, “Thermomechanical response of 3D laser-deposited Ti-6Al-4V alloy over a wide range of strain rates and temperatures,” *Mater. Sci. Eng. A*, 2015.

[65] N. Biswas, J. L. Ding, V. K. Balla, D. P. Field, and A. Bandyopadhyay, “Deformation and

fracture behavior of laser processed dense and porous Ti6Al4V alloy under static and dynamic loading," *Mater. Sci. Eng. A*, 2012.

[66] S. Leuders *et al.*, "On the mechanical behaviour of titanium alloy TiAl6V4 manufactured by selective laser melting: Fatigue resistance and crack growth performance," *Int. J. Fatigue*, 2013.

[67] H. Galarraga, D. A. Lados, R. R. Dehoff, M. M. Kirka, and P. Nandwana, "Effects of the microstructure and porosity on properties of Ti-6Al-4V ELI alloy fabricated by electron beam melting (EBM)," *Addit. Manuf.*, 2016.

[68] P. A. Kobryn, E. H. Moore, and S. L. Semiatin, "Effect of laser power and traverse speed on microstructure, porosity, and build height in laser-deposited Ti-6Al-4V," *Scr. Mater.*, 2000.

[69] Y. Yang and H. C. Man, "Microstructure evolution of laser clad layers of W-C-Co alloy powders," *Surf. Coatings Technol.*, 2000.

[70] A. Bauereiß, T. Scharowsky, and C. Körner, "Defect generation and propagation mechanism during additive manufacturing by selective beam melting," *J. Mater. Process. Technol.*, 2014.

[71] G. K. L. Ng, A. E. W. Jarfors, G. Bi, and H. Y. Zheng, "Porosity formation and gas bubble retention in laser metal deposition," *Appl. Phys. A Mater. Sci. Process.*, 2009.

[72] J. Choi and Y. Chang, "Characteristics of laser aided direct metal/material deposition process for tool steel," *Int. J. Mach. Tools Manuf.*, 2005.

[73] C. de Formanoir, S. Michotte, O. Rigo, L. Germain, and S. Godet, "Electron beam melted Ti-6Al-4V: Microstructure, texture and mechanical behavior of the as-built and heat-treated material," *Mater. Sci. Eng. A*, 2016.

[74] E. Wycisk, A. Solbach, S. Siddique, D. Herzog, F. Walther, and C. Emmelmann, "Effects of defects in laser additive manufactured Ti-6Al-4V on fatigue properties," in *Physics Procedia*, 2014.

[75] P. Li, D. H. Warner, A. Fatemi, and N. Phan, “Critical assessment of the fatigue performance of additively manufactured Ti-6Al-4V and perspective for future research,” *Int. J. Fatigue*, 2016.

[76] C. Casavola, L. S.Campanelli, and C. Pappalettere, “Experimental analysis of residual stresses in the selective laser melting process,” in *Society for Experimental Mechanics - 11th International Congress and Exhibition on Experimental and Applied Mechanics 2008*, 2008.

[77] G. Vastola, G. Zhang, Q. X. Pei, and Y. W. Zhang, “Controlling of residual stress in additive manufacturing of Ti6Al4V by finite element modeling,” *Addit. Manuf.*, 2016.

[78] Y. Liu, Y. Yang, and D. Wang, “A study on the residual stress during selective laser melting (SLM) of metallic powder,” *Int. J. Adv. Manuf. Technol.*, 2016.

[79] N. Hrabe, T. Gnäupel-Herold, and T. Quinn, “Fatigue properties of a titanium alloy (Ti–6Al–4V) fabricated via electron beam melting (EBM): Effects of internal defects and residual stress,” *Int. J. Fatigue*, 2017.

[80] L. Parry, I. A. Ashcroft, and R. D. Wildman, “Understanding the effect of laser scan strategy on residual stress in selective laser melting through thermo-mechanical simulation,” *Addit. Manuf.*, 2016.

[81] Q. Zhang, J. Xie, Z. Gao, T. London, D. Griffiths, and V. Oancea, “A metallurgical phase transformation framework applied to SLM additive manufacturing processes,” *Mater. Des.*, 2019.

[82] C. Körner, E. Attar, and P. Heinl, “Mesoscopic simulation of selective beam melting processes,” *J. Mater. Process. Technol.*, 2011.

[83] J. A. Cherry, H. M. Davies, S. Mehmood, N. P. Lavery, S. G. R. Brown, and J. Sienz, “Investigation into the effect of process parameters on microstructural and physical properties of 316L stainless steel parts by selective laser melting,” *Int. J. Adv. Manuf. Technol.*, 2014.

[84] M. Shellabear and O. Nyrhilä, “DMLS – Development History and State of the Art,” *Lane*

2004, 2004.

[85] M. Yan and P. Yu, “An Overview of Densification, Microstructure and Mechanical Property of Additively Manufactured Ti-6Al-4V — Comparison among Selective Laser Melting, Electron Beam Melting, Laser Metal Deposition and Selective Laser Sintering, and with Conventional Powder,” in *Sintering Techniques of Materials*, 2015.

[86] T. Seshacharyulu, S. C. Medeiros, J. T. Morgan, J. C. Malas, W. G. Frazier, and Y. V. R. K. Prasad, “Hot deformation and microstructural damage mechanisms in extra-low interstitial (ELI) grade Ti-6Al-4V,” *Mater. Sci. Eng. A*, 2000.

[87] G. Lütjering, “Influence of processing on microstructure and mechanical properties of (α + β) titanium alloys,” *Mater. Sci. Eng. A*, 1998.

[88] T. Ahmed and H. J. Rack, “Phase transformations during cooling in α+β titanium alloys,” *Mater. Sci. Eng. A*, 1998.

[89] A. Ducato, L. Fratini, M. La Cascia, and G. Mazzola, “An automated visual inspection system for the classification of the phases of Ti-6Al-4V titanium alloy,” in *Lecture Notes in Computer Science (including subseries Lecture Notes in Artificial Intelligence and Lecture Notes in Bioinformatics)*, 2013.

[90] L. H. Mair, T. A. Stolarski, R. W. Vowles, and C. H. Lloyd, “Wear: Mechanisms, manifestations and measurement. Report of a workshop,” in *Journal of Dentistry*, 1996.

[91] M. Abebe and F. C. Appl, “Theoretical analysis of the basic mechanics of abrasive processes. Part I: General model,” *Wear*, 1988.

[92] K. H. Zum Gahr, “Microstructure and Wear of Materials (Chapter 6 SLIDING WEAR),” *Tribol. Ser.*, 1987.

[93] M. Salmi *et al.*, “Patient-specific reconstruction with 3D modeling and DMLS additive manufacturing,” *Rapid Prototyp. J.*, 2012.

[94] American Society for Testing and Materials, “ASTM F136-13: Standard Specification for

Wrought Titanium-6Aluminum-4Vanadium ELI (Extra Low Interstitial) Alloy for Surgical Implant Applications (UNS R56401),” *Annu. B. ASTM Stand.*, 2015.

[95] ISO/ASTM, “INTERNATIONAL STANDARD ISO / ASTM 52900 Additive manufacturing — General principles — Terminology,” *International Organization for Standardization*, 2015. .

[96] W. Q. Toh, P. Wang, X. Tan, M. L. S. Nai, E. Liu, and S. B. Tor, “Microstructure and wear properties of electron beam melted Ti-6Al-4V parts: A comparison study against as-cast form,” *Metals (Basel).*, 2016.

[97] J. K. Ervin, “Post Heat Treatment Effects of Ti-6Al-4V Produced via Solid Freeform Electron Beam Melting,” *Mater. Sci. Eng.*, 2008.

[98] M. T. Jovanović, S. Tadić, S. Zec, Z. Mišković, and I. Bobić, “The effect of annealing temperatures and cooling rates on microstructure and mechanical properties of investment cast Ti-6Al-4V alloy,” *Mater. Des.*, 2006.

[99] W. Sha and Z. Guo, “Phase evolution of Ti-6A1-4V during continuous heating,” *J. Alloys Compd.*, 1999.

[100] B. Vrancken, L. Thijs, J. P. Kruth, and J. Van Humbeeck, “Heat treatment of Ti6Al4V produced by Selective Laser Melting: Microstructure and mechanical properties,” *J. Alloys Compd.*, 2012.

[101] Y. Fan, W. Tian, Y. Guo, Z. Sun, and J. Xu, “Relationships among the Microstructure, Mechanical Properties, and Fatigue Behavior in Thin Ti6Al4V,” *Adv. Mater. Sci. Eng.*, 2016.

[102] R. Sahoo, S. Mantry, T. K. Sahoo, S. Mishra, and B. B. Jha, “Effect of microstructural variation on erosion wear behavior of Ti-6Al-4V alloy,” *Tribol. Trans.*, vol. 56, no. 4, pp. 555–560, 2013.

[103] M. Emiliani and R. Brown, “The effect of microstructure on the erosion of Ti-6Al-4V by spherical particles at 90° impact angles,” *Wear*, 1984.

[104] M. Naim and S. Bahadur, “Effect of microstructure and mechanical properties on the erosion of 18 Ni (250) maraging steel,” *Wear*, 1986.

[105] M. Naim and S. Bahadur, “Erosion behavior of prestrained and aged 2024 aluminum,” *Wear*, 1988.

[106] M. Naim and S. Bahadur, “Effect of precipitated and dispersed hard particles on erosion,” *Lubr. Eng.*, 1990.

[107] L. Ambrosini and S. Bahadur, “Erosion of AISI 4140 steel,” *Wear*, 1987.

[108] I. Cvijović-Alagić, S. Mitrović, Z. Cvijović, D. Veljović, M. Babić, and M. Rakin, “Influence of the heat treatment on the tribological characteristics of the tibased alloy for biomedical applications,” *Tribol. Ind.*, vol. 31, no. 3–4, pp. 17–22, 2009.

[109] H. Galarraga, R. J. Warren, D. A. Lados, R. R. Dehoff, M. M. Kirka, and P. Nandwana, “Effects of heat treatments on microstructure and properties of Ti-6Al-4V ELI alloy fabricated by electron beam melting (EBM),” *Mater. Sci. Eng. A*, vol. 685, no. December 2016, pp. 417–428, 2017.

APPENDIX

SEM Wear result

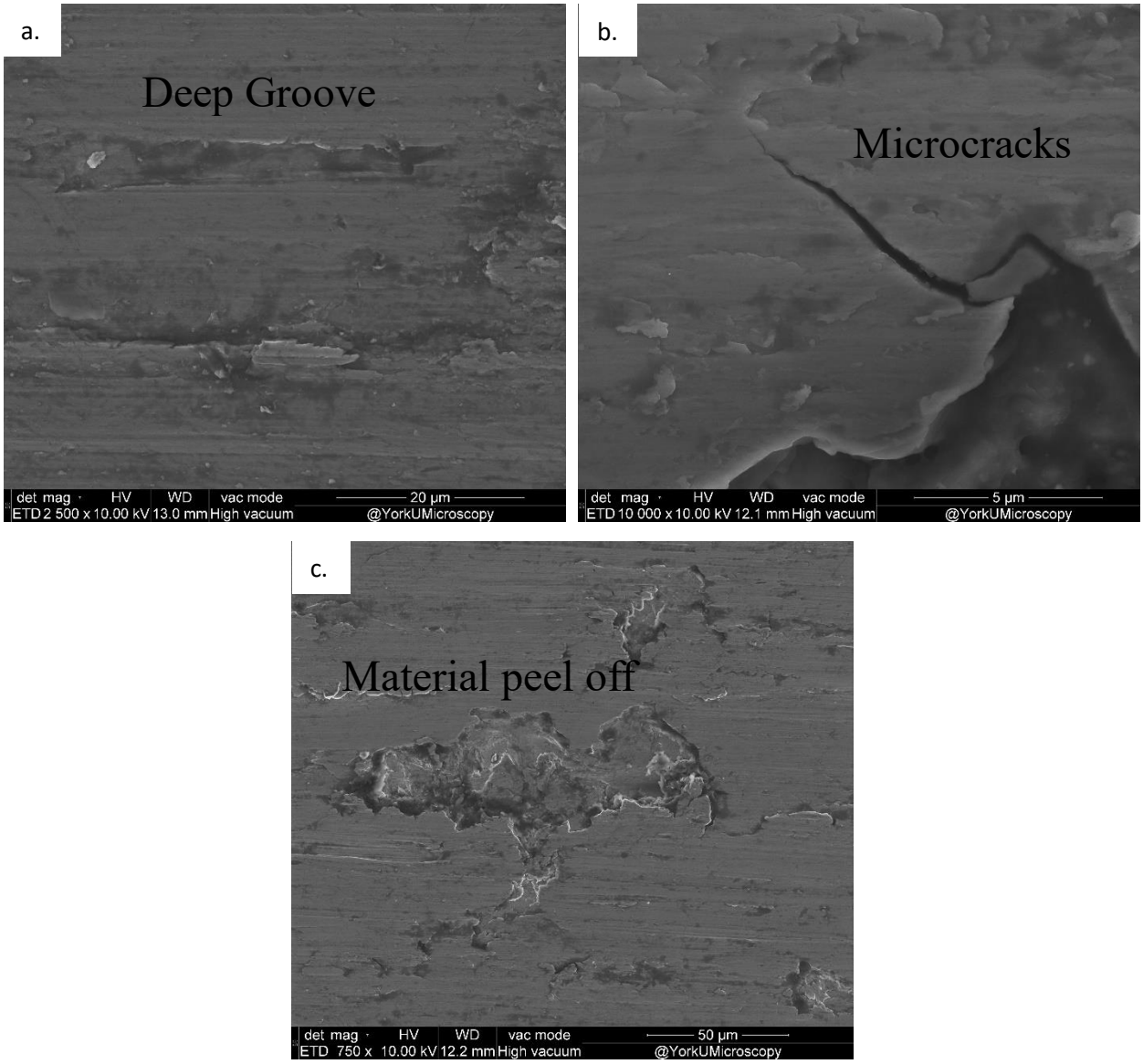

Three different wear mechanisms seen on the wear track a. Abrasive wear b. Fatigue wear c. Adhesive wear.

EPMA result

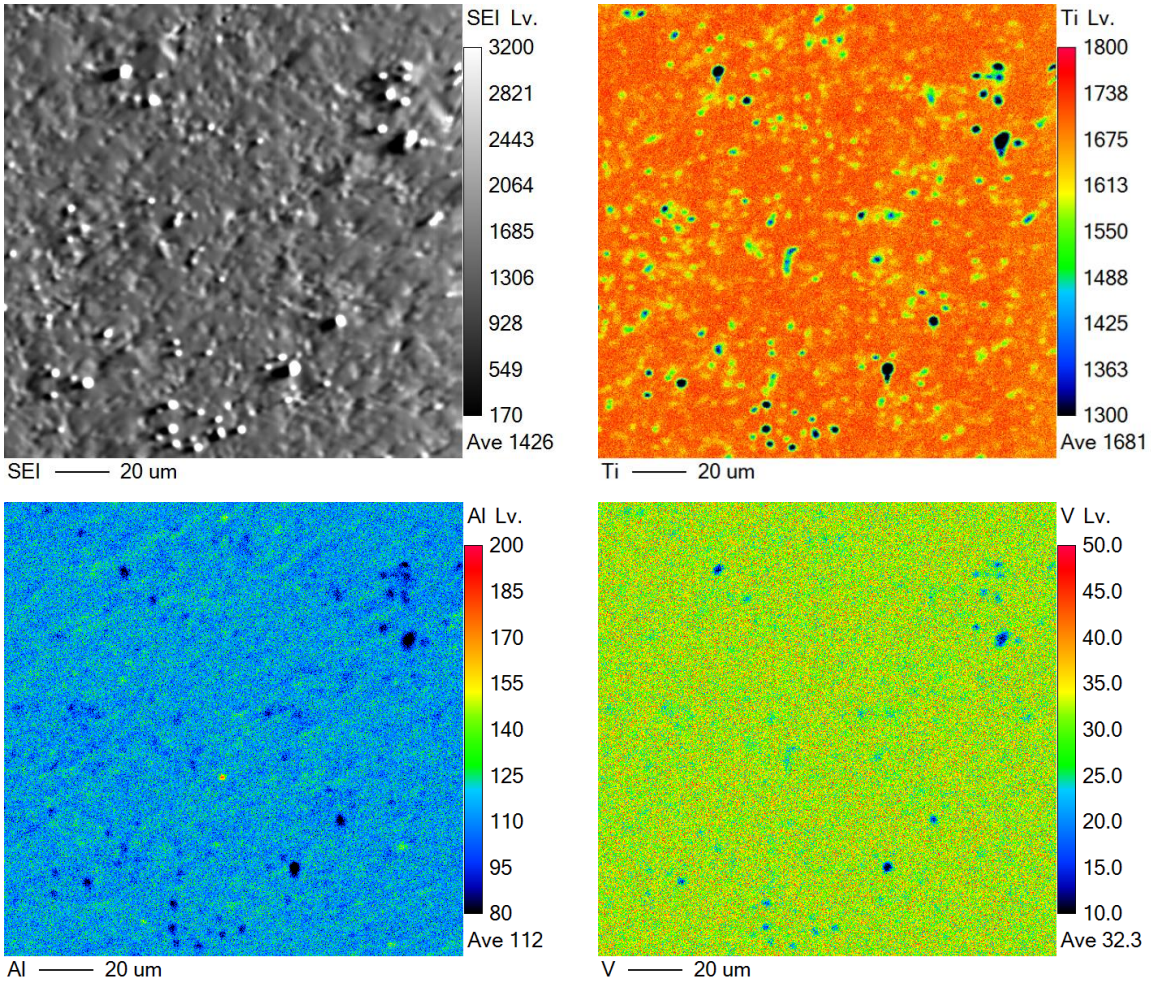

EPMA micrographs describe the Titanium, Aluminum, and Vanadium distribution in the As-Printed 3D Sample

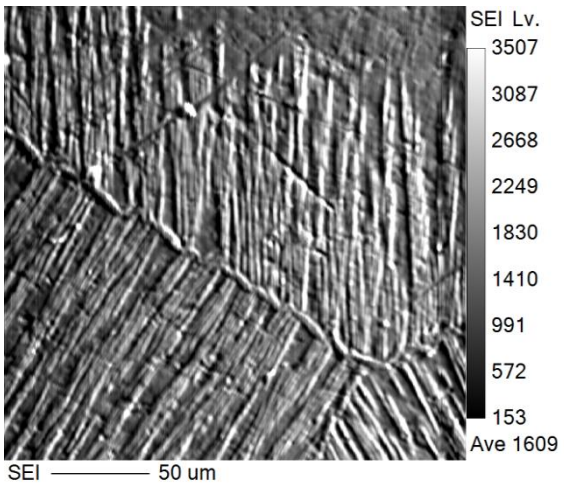

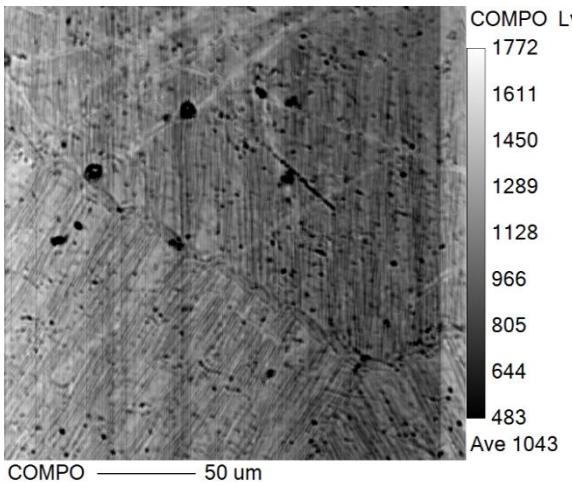

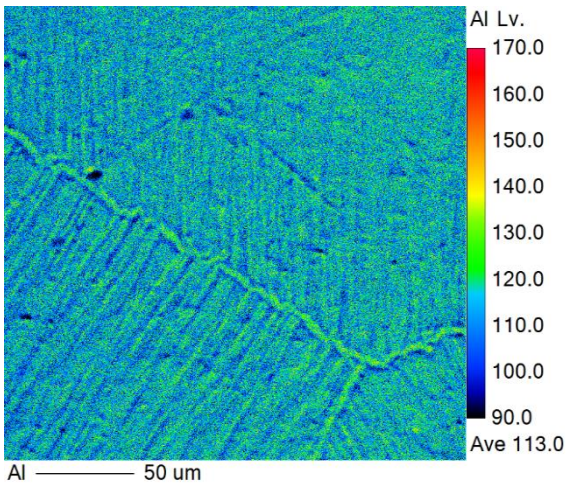

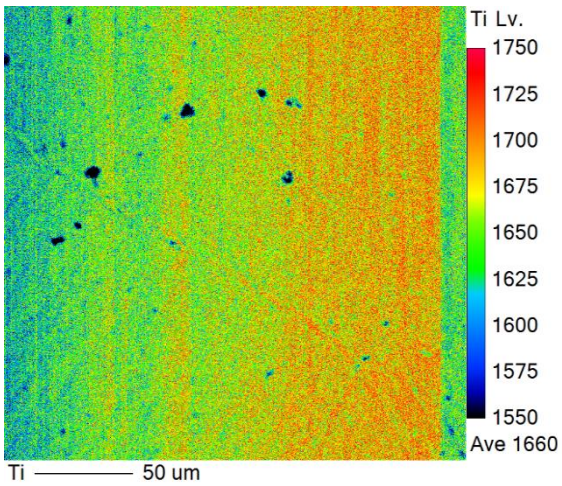

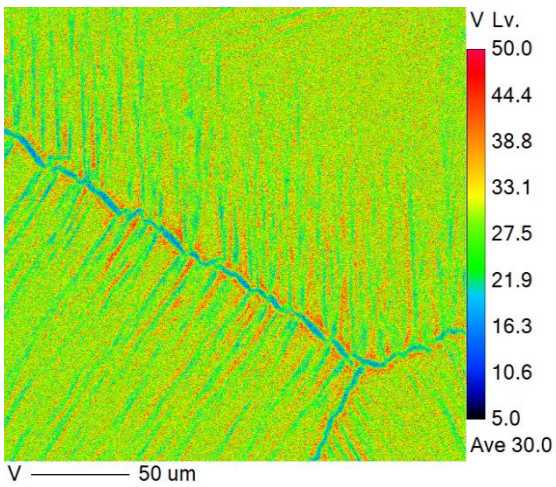

EPMA micrographs describe the Titanium, Aluminum, and Vanadium distribution in the WQ1080 CV Sample

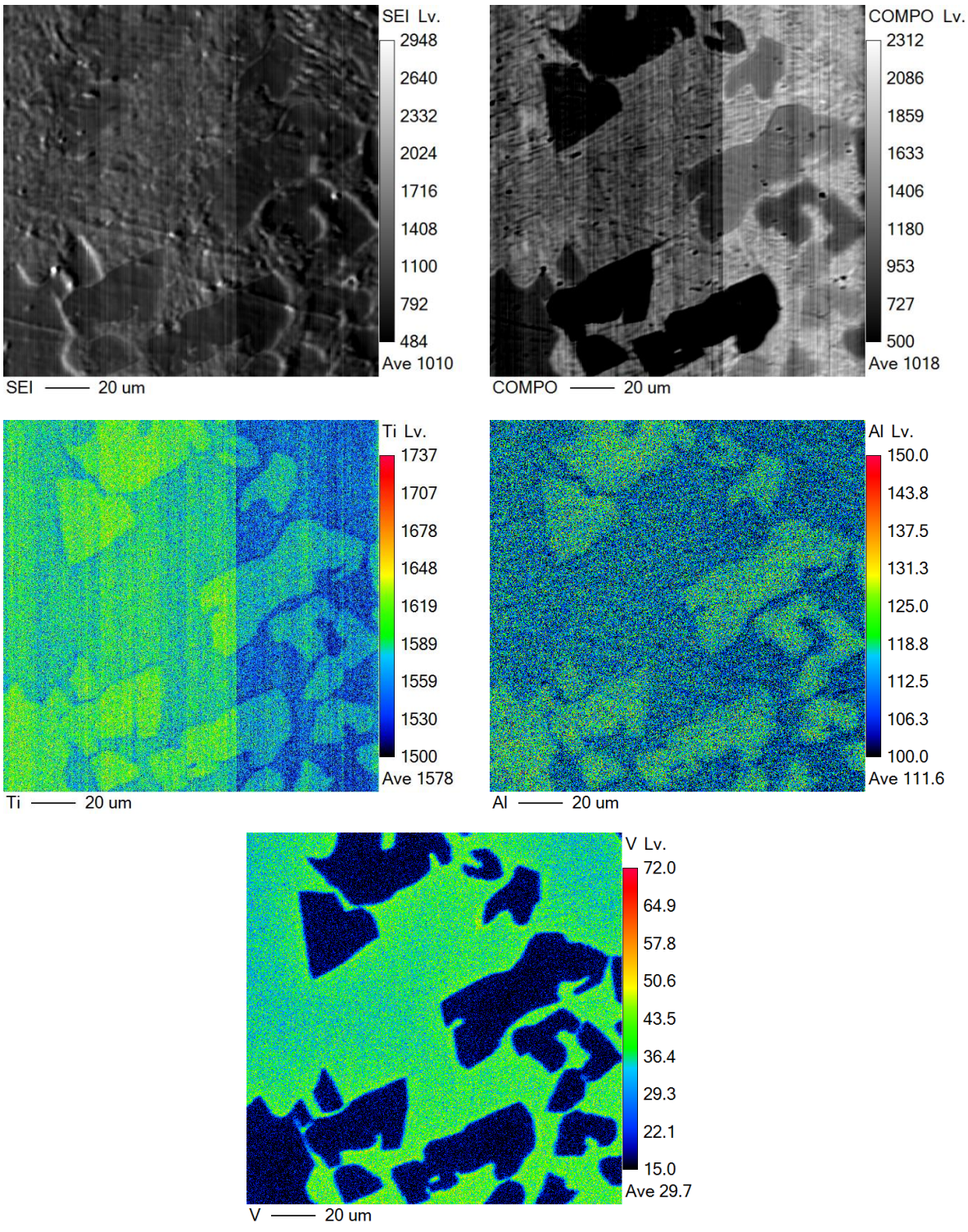

EPMA micrographs describe the Titanium, Aluminum, and Vanadium distribution in WQ1080 3D sample

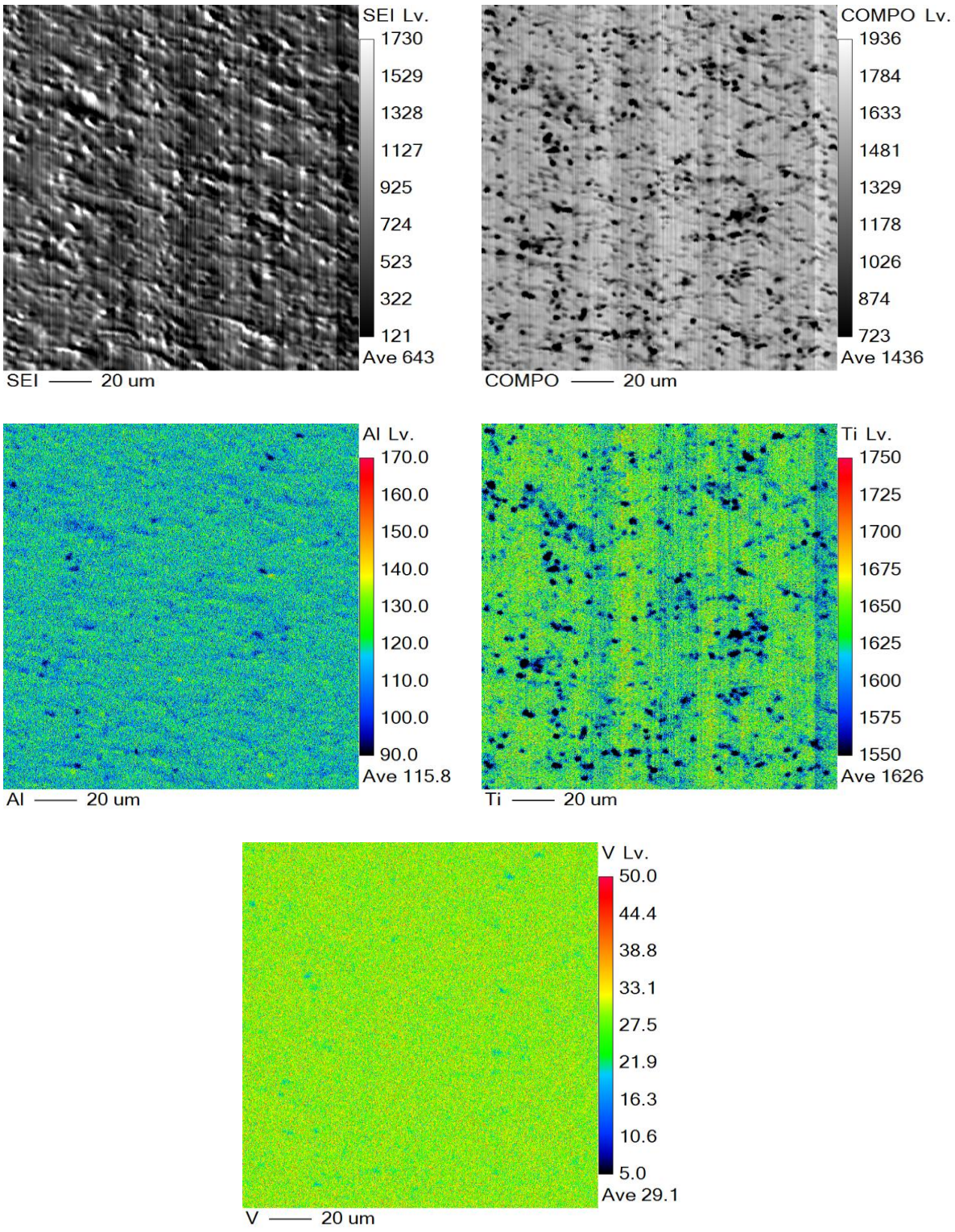

EPMA micrographs describe the Titanium, Aluminum, and Vanadium distribution in WQ500 CV Sample

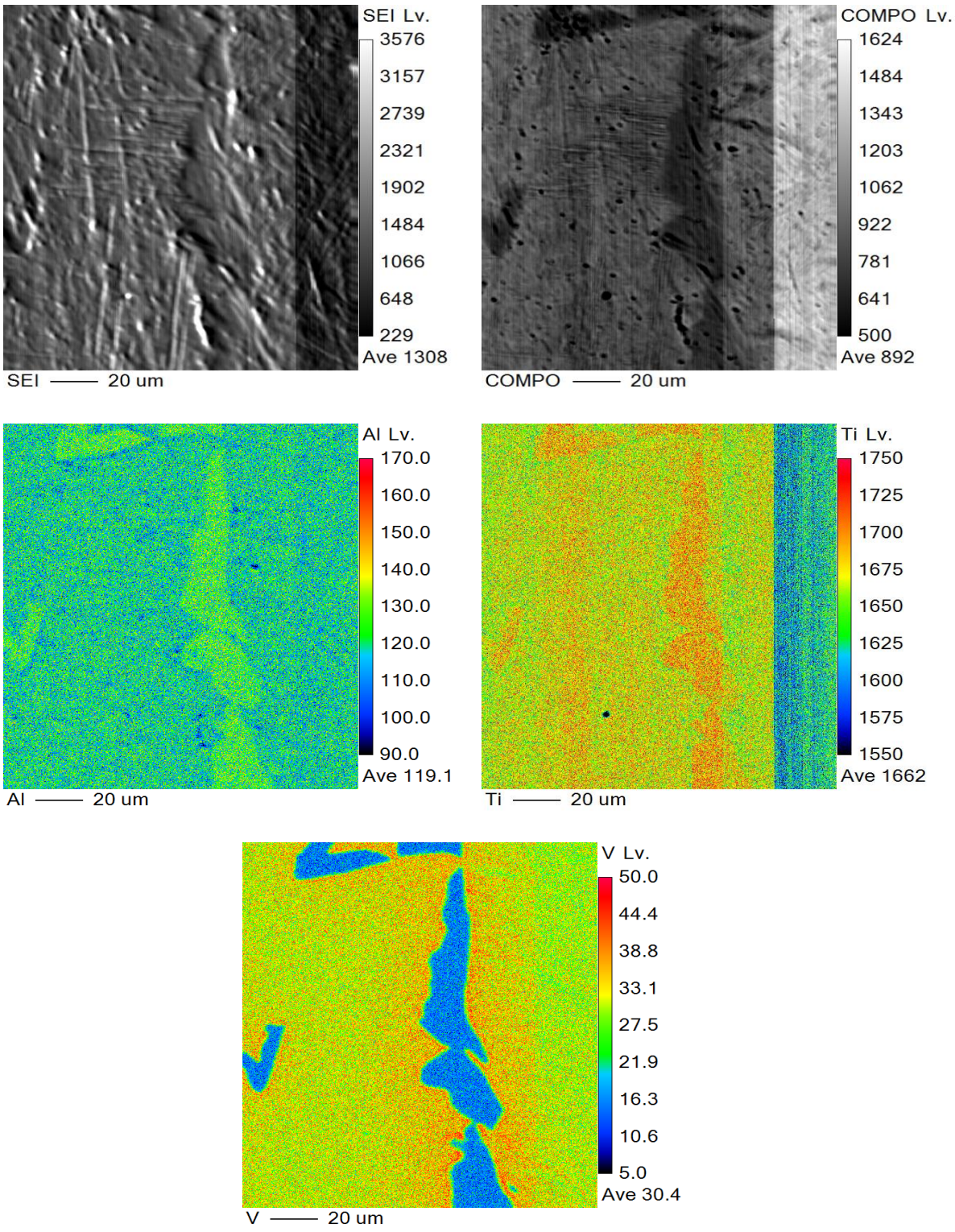

EPMA micrographs describe the Titanium, Aluminum, and Vanadium distribution in WQ500 3D Sample

XRD result

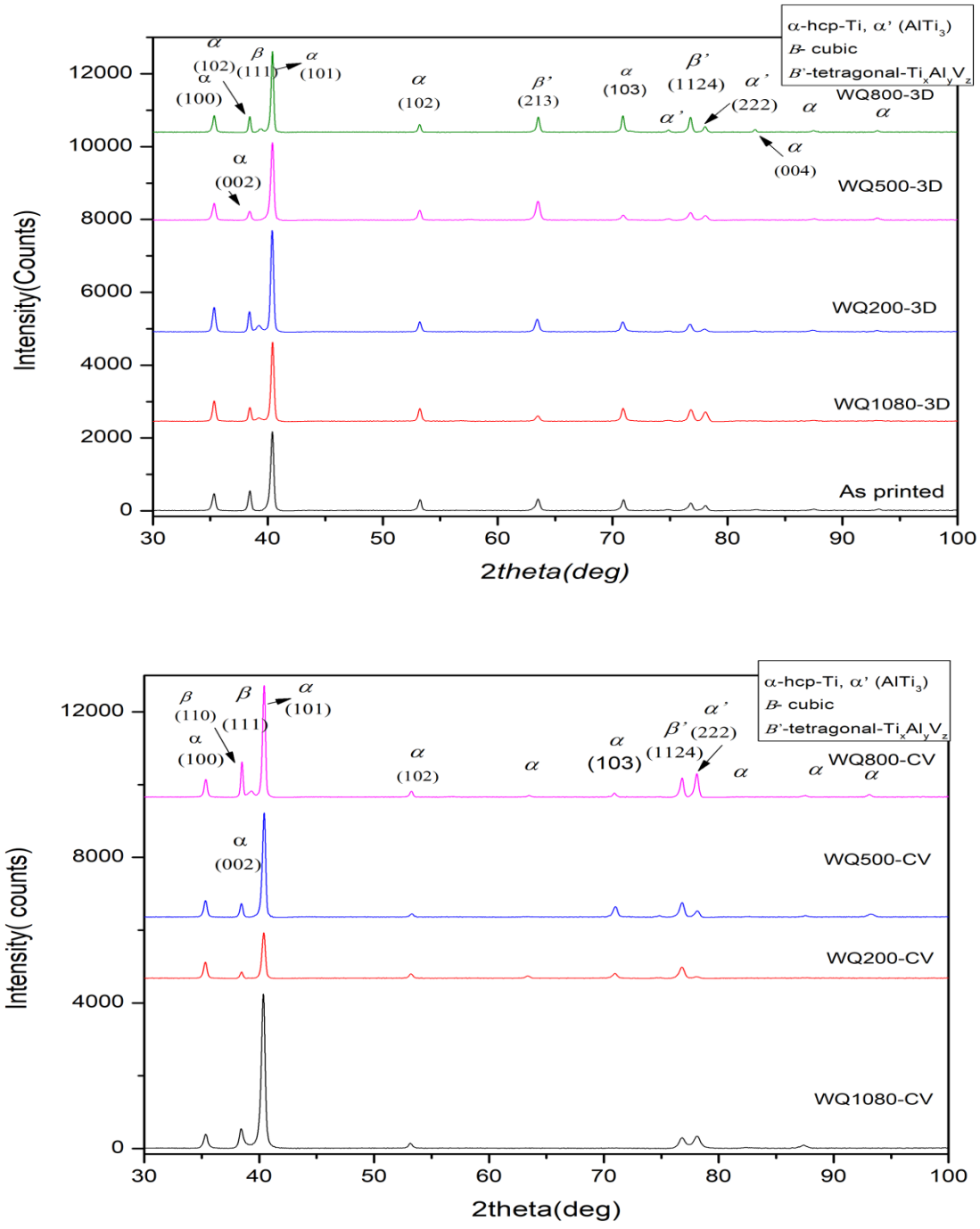

X-ray diffraction (XRD) analysis for water Quenched 3D printed and Conventional medical-grade Ti6Al4V

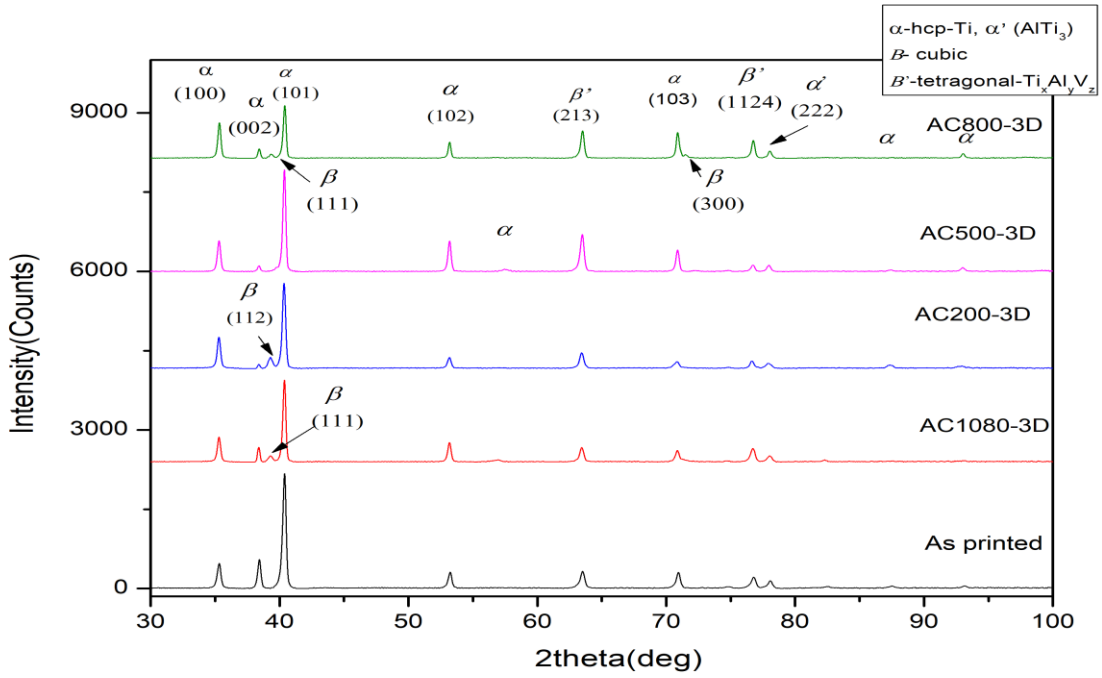

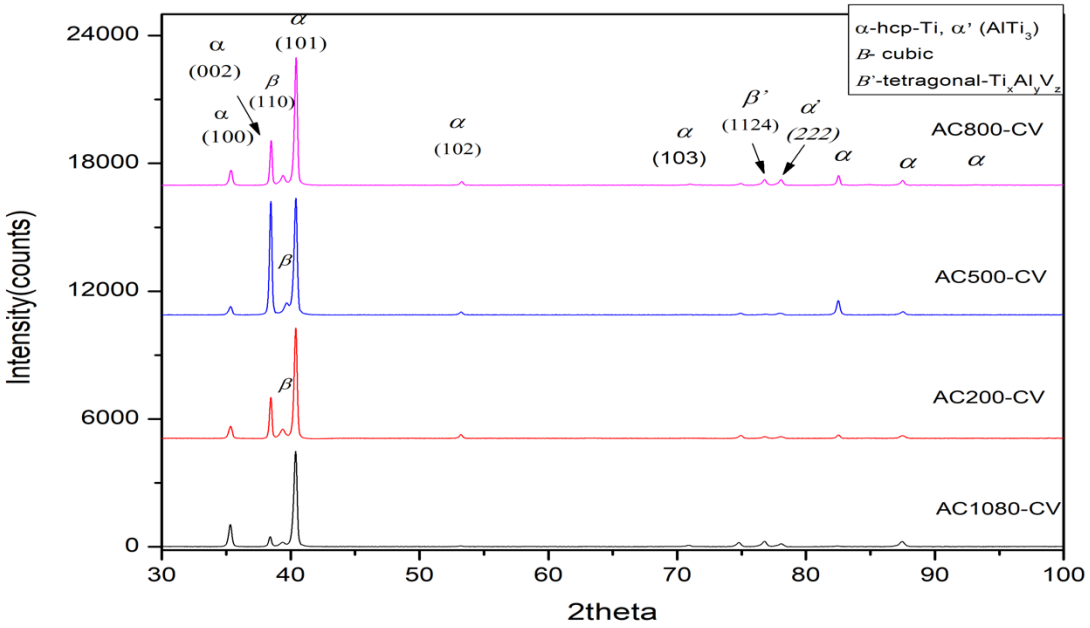

X-ray diffraction (XRD) analysis for Air-Cooled 3D printed and Conventional medical-grade Ti6Al4V